Politecnico di Bari

Repository Istituzionale dei Prodotti della Ricerca del Politecnico di Bari

Control and optimization strategies for noise transmission reduction in sonic crystal acoustic barriers

This is a PhD Thesis

Original Citation:
Control and optimization strategies for noise transmission reduction in sonic crystal acoustic barriers / Ramirez Solana, David. - ELETTRONICO. - (2025). [10.60576/poliba/iris/ramirez-solana-david_phd2025]

Availability:
This version is available at http://hdl.handle.net/11589/281821 since: 2025-01-10

Published version
DOI:10.60576/poliba/iris/ramirez-solana-david_phd2025

Publisher: Politecnico di Bari

Terms of use:

(Article begins on next page)

21 July 2026

DOUBLE PHD DEGREE COTUTELLE

PH.D. PROGRAMS IN
ELECTRICAL AND INFORMATION ENGINEERING AND
IN DESIGN, MANUFACTURING AND MANAGEMENT OF
INDUSTRIAL PROJECTS

Final Dissertation

CONTROL AND OPTIMIZATION STRATEGIES FOR NOISE TRANSMISSION REDUCTION IN SONIC CRYSTAL ACOUSTIC BARRIERS

by
David Ramírez Solana

External Reviewers:
Prof. Andrés Prieto Aneiros
Prof. Jaime Ramis Soriano

Supervisors:
Prof.ssa Maria Pia Fanti
Prof. Javier Redondo

Co-supervisor:
Prof. Agostino M. Mangini

Cycle XXXVII - November, 1st 2021 - October 31st 2024

Politecnico di Bari

LIBERATORIA PER L'ARCHIVIAZIONE DELLA TESI DI DOTTORATO

Al Magnifico Rettore
del Politecnico di Bari

Il/la sottoscritto/a_ ***David Ramírez Solana*** nato/a a **Valencia (Spagna)_** il_**19/03/1994**

residente a **Godella(Spagna)** in via **Ramon y Cajal, 38, 6** e-mail ***david.ramirezsolana@poliba.it***

iscritto al 3° anno di Corso di Dottorato di Ricerca in _ ***Ingegnera Elettrica e Dell'informazione*** ciclo_**XXXVII**

ed essendo stato ammesso a sostenere l'esame finale con la prevista discussione della tesi dal titolo:

Control and Optimization Strategies for Noise Transmission Reduction in Sonic Crystal Acoustic Barriers

DICHIARA

1) di essere consapevole che, ai sensi del D.P.R. n. 445 del 28.12.2000, le dichiarazioni mendaci, la falsità negli atti e l'uso di atti falsi sono puniti ai sensi del codice penale e delle Leggi speciali in materia, e che nel caso ricorressero dette ipotesi, decade fin dall'inizio e senza necessità di nessuna formalità dai benefici conseguenti al provvedimento emanato sulla base di tali dichiarazioni;
2) di essere iscritto al Corso di Dottorato di ricerca ***Ingegnera Elettrica e Dell'informazione,*** ciclo_**XXXVII,** corso attivato ai sensi del "*Regolamento dei Corsi di Dottorato di ricerca del Politecnico di Bari"*, emanato con D.R. n.286 del 01.07.2013;
3) di essere pienamente a conoscenza delle disposizioni contenute nel predetto Regolamento in merito alla procedura di deposito, pubblicazione e autoarchiviazione della tesi di dottorato nell'Archivio Istituzionale ad accesso aperto alla letteratura scientifica;
4) di essere consapevole che attraverso l'autoarchiviazione delle tesi nell'Archivio Istituzionale ad accesso aperto alla letteratura scientifica del Politecnico di Bari (IRIS-POLIBA), l'Ateneo archivierà e renderà consultabile in rete (nel rispetto della Policy di Ateneo di cui al D.R. 642 del 13.11.2015) il testo completo della tesi di dottorato, fatta salva la possibilità di sottoscrizione di apposite licenze per le relative condizioni di utilizzo (di cui al sito http://www.creativecommons.it/Licenze), e fatte salve, altresì, le eventuali esigenze di "embargo", legate a strette considerazioni sulla tutelabilità e sfruttamento industriale/commerciale dei contenuti della tesi, da rappresentarsi mediante compilazione e sottoscrizione del modulo in calce (Richiesta di embargo);
5) che la tesi da depositare in IRIS-POLIBA, in formato digitale (PDF/A) sarà del tutto identica a quelle **consegnate**/inviate/da inviarsi ai componenti della commissione per l'esame finale e a qualsiasi altra copia depositata presso gli Uffici del Politecnico di Bari in forma cartacea o digitale, ovvero a quella da discutere in sede di esame finale, a quella da depositare, a cura dell'Ateneo, presso le Biblioteche Nazionali Centrali di Roma e Firenze e presso tutti gli Uffici competenti per legge al momento del deposito stesso, e che di conseguenza va esclusa qualsiasi responsabilità del Politecnico di Bari per quanto riguarda eventuali errori, imprecisioni o omissioni nei contenuti della tesi;
6) che il contenuto e l'organizzazione della tesi è opera originale realizzata dal sottoscritto e non compromette in alcun modo i diritti di terzi, ivi compresi quelli relativi alla sicurezza dei dati personali; che pertanto il Politecnico di Bari ed i suoi funzionari sono in ogni caso esenti da responsabilità di qualsivoglia natura: civile, amministrativa e penale e saranno dal sottoscritto tenuti indenni da qualsiasi richiesta o rivendicazione da parte di terzi;
7) che il contenuto della tesi non infrange in alcun modo il diritto d'Autore né gli obblighi connessi alla salvaguardia di diritti morali od economici di altri autori o di altri aventi diritto, sia per testi, immagini, foto, tabelle, o altre parti di cui la tesi è composta.

Luogo e data **Bari, 09/01/2025** Firma _____

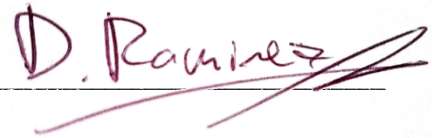

Il/La sottoscritto, con l'autoarchiviazione della propria tesi di dottorato nell'Archivio Istituzionale ad accesso aperto del Politecnico di Bari (POLIBA-IRIS), pur mantenendo su di essa tutti i diritti d'autore, morali ed economici, ai sensi della normativa vigente (Legge 633/1941 e ss.mm.ii.),

CONCEDE

- al Politecnico di Bari il permesso di trasferire l'opera su qualsiasi supporto e di convertirla in qualsiasi formato al fine di una corretta conservazione nel tempo. Il Politecnico di Bari garantisce che non verrà effettuata alcuna modifica al contenuto e alla struttura dell'opera.
- al Politecnico di Bari la possibilità di riprodurre l'opera in più di una copia per fini di sicurezza, back-up e conservazione.

Luogo e data **Bari, 09/01/2025_** Firma _____

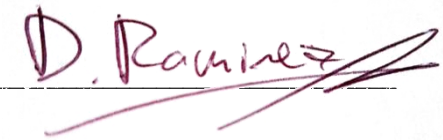

"What we know is a drop, what we don't know is an ocean."- Isaac Newton.

Acknowledgements

Ante todo, mi mayor agradecimiento va a mi madre y a mi hermano, a mi familia, que siempre ha estado ahí apoyándome y animándome. También a mi padre, que me sirve de inspiración desde arriba como camino a seguir en la vida, no solo en el ámbito académico.

Un ringraziamento speciale va alla mia supervisora, la Professoressa Maria Pia Fanti, direttrice del *Laboratory of Control and Automation*. Mi sento molto onorato di aver potuto lavorare sotto la supervisione di una persona così importante nel campo dell'Automatica, di cui ammiro la grande dedizione alla ricerca e l'enorme capacità gestionale, riuscendo a coordinare sia progetti internazionali che questa stessa tesi. Ringrazio inoltre particolarmente l'equilibrio tra la libertà che mi ha offerto per proporre idee e la guida per riorientare quelle che non erano corrette. Ringrazio anche la sua attenzione e la formazione ricevuta da parte sua. Insieme a lei, desidero esprimere la mia gratitudine al mio co-supervisore, Agostino Marcello Mangini, dal quale, oltre a ricevere un grande supporto durante la tesi, ho potuto apprendere dalla sua didattica e metterla in pratica in uno dei suoi corsi.

Por la parte italiana, no quisiera olvidarme de mis compañeros del LCA, mis amigos Puglieses, de Bari y alrededores que han hecho durante largos periodos de este trienio que sienta ahora una segunda casa allí.

En Valencia, mi director Javier Redondo ha sido un guía desde el inicio del máster cuando el doctorado aún quedaba muy lejano y el cual no ha dejado de creer en mí por muy complicado que fuese encontrar el rumbo adecuado al principio.Agradezco su incalculable ayuda y atención diaria. Gracias también a Rubén, Jaime G., Valentino, Andrés, Jaime R. y demás personas que han contribuido a este documento.

Gracias a mi psicologa Virgina, que me ha ayudado a gestionar el síndrome del impostor y frustraciones varias durante periodos difíciles. Me siento muy afortunado de la personas con las he compartido este camino, de más cerca o más lejos y que me han aguantado en Italia y España. Para acabar me siento muy agradecido de la gente que tengo cerca, la cual además de elegirla, ha elegido quedarse junto a mi día tras día.

Abstract

Acoustic metamaterials, such as Sonic Crystals (SC), are periodic artificial structures designed to manipulate sound waves in ways that natural materials cannot. These materials consist of arranged lattices of rigid scatterers embedded in air and exhibit unique properties, such as negative refraction and Band Gaps (BG), which can be leveraged to create highly effective noise control solutions. These Band Gaps prevent transmission of certain frequency ranges depending on the angle of incidence the sound waves relative to the crystal, making them ideal for applications in noise barriers and other acoustic devices.

This research investigates the potential of these advanced materials to enhance the performance of noise reduction devices through innovative design and optimization strategies aimed at minimizing unwanted sound, thereby improving the acoustic environment in various settings. Specifically, among noise reduction devices such as barriers, absorbers, and diffusers, this thesis focuses on Sonic Crystal Noise Barriers (SCNB).

The design and optimization of these devices require a deep understanding of acoustic principles and the ability to predict how sound interacts with different materials and structures. This is achieved through the use of simulations that forecast the behavior and performance of these devices, thus saving time and resources by avoiding the need to manufacture and experimentally test multiple prototypes before arriving at the optimal solution for each specific case.

In line with this, the thesis explores the potential of Active Noise Control (ANC) systems enhanced with Reinforcement Learning (RL) techniques as a complement to improve SCNBs. By integrating reinforcement learning, the study aims to develop ANC systems that continuously learn and adapt to changing environmental conditions, providing a dynamic and adaptive approach to noise control, particularly at low frequencies, where active control is most effective, and where SCNBs tend to be less efficient.

In addition to ANC, Helmholtz Resonators (HR) are incorporated to improve these barriers. By combining numerical methods and optimization

algorithms, not only is the performance of SCNBs found in the literature improved, but a deeper understanding of the physical principles governing them and their interaction with HR is also achieved. 3D printing technology, used in architectural engineering, combined with parametric modeling, greatly increases the versatility in the creation of prototypes resulting from optimizations with HRs.

This thesis also addresses the insulation capabilities of SCNBs made from cylindrical scatterers with multiple Helmholtz resonators, proposing a design that incorporates two Helmholtz resonators per scatterer. This design shows a significant increase in Insertion Loss (IL) compared to conventional barriers. Additionally,examining the interaction between the BGs of HRs and Bragg-BGs, this thesis proposes new transmission applications for multiresonant SCs beyond noise barriers. The ability to control transmission through an active metamaterial by rotating the scatterers provides an advantage over conventional passive metamaterials.

Furthermore, the thesis explores, both numerically and experimentally, wave incidence measurements to further refine noise control strategies. Prototypes designed to mitigate tonal noise, such as that produced by train braking, are experimentally tested under both normal incidence and diffuse incidence of sound waves on the SCNB.

In summary, this doctoral thesis provides a comprehensive exploration of SCNBs, from design and optimization to practical applications. It delves into the phenomenology of the interactions between these periodic materials, ANC, HRs, and 3D printing. By integrating advanced optimization techniques and reinforcement learning, the study aims to improve current noise control solutions.

Resum

Els metamaterials acústics, com els Sonic Crystals (SC), són estructures artificials periòdiques dissenyades per a controlar les ones sonores de maneres que els materials naturals no poden. Aquests materials exhibeixen propietats úniques, com la refracció negativa i les Band Gaps (BG), que es poden aprofitar per a crear solucions de control de soroll altament efectives. Aquests Band Gaps (o bandes prohibides en espanyol) permeten prohibir la transmissió de certs rangs freqüencials en determinades direccions d'incidència de la font sonora amb respecte al cristall, cosa que els fa ideals per a aplicacions en barreres de soroll i altres dispositius acústics. Aquesta investigació investiga el potencial d'aquests materials avançats per a millorar el rendiment dels dispositius de reducció de soroll mitjançant estratègies innovadores de disseny i optimització, dissenyades per a minimitzar el so no desitjat, millorant així l'entorn acústic en diversos entorns. Més concretament, dins dels dispositius de reducció de soroll, que abasten barreres, absorbents i difusors, aquesta tesi se centra en les barreres basades en cristalls de so (SCNB). El disseny i l'optimització d'aquests dispositius requereixen una comprensió profunda dels principis acústics i la capacitat de predir com interactua el so amb diferents materials i estructures. Per a això, és necessària la utilització de simulacions que prediuen el comportament i rendiment d'aquests dispositius, podent així estalviar temps i diners d'haver de fabricar els diferents dissenys i haver de provar els prototips experimentalment per a finalment donar amb la millor solució per a cada cas específic. En aquesta línia, la tesi investiga el potencial dels sistemes de control actiu del soroll (ANC), millorats amb tècniques d'aprenentatge per reforç (RL), com un complement que permeti millorar les SCNB. En integrar l'aprenentatge per reforç, l'estudi té com a objectiu desenvolupar sistemes ANC que aprenguin i s'adaptin contínuament a les condicions ambientals canviants, proporcionant un enfocament dinàmic i adaptatiu per al control del soroll, amb un especial focus en freqüències baixes on el control actiu és més eficient i on les SCNB ho són menys.

A més de l'ANC, s'incorporen Resonadors de Helmholtz (HR) per a

millorar aquestes barreres. Gràcies a la combinació de mètodes numèrics i algorismes d'optimització, no només es millora el rendiment de les barreres d'aquesta tipologia trobades en la literatura sinó que millora la comprensió dels principis físics que les governen i la seua interacció amb els HR. Aprofitant els avanços en la tecnologia d'impressió tridimensional (3D) en l'enginyeria arquitectònica i mitjançant l'ús de modelatge paramètric, la versatilitat augmenta enormement en el procés de creació dels prototips que han estat resultats de les optimitzacions amb els HR. Aquesta tesi també aborda la capacitat d'aïllament de les SCNB fetes de dispersors cilíndrics amb diversos ressonadors de Helmholtz, proposant un disseny amb dispersors que inclouen dos ressonadors de Helmholtz. Aquest disseny demostra un augment significatiu en la Insertion Loss (IL) en comparació amb les barreres convencionals.

La tesi també explora tant numèricament com experimentalment, resultats de mesuraments d'incidència d'ones per a refinar encara més les estratègies de control de soroll. Es testegen experimentalment prototips dissenyats per a mitigar un soroll tonal molest com el de la frenada dels trens, tant en incidència normal com en incidència difusa de les ones sobre la barrera de SC. En resum, aquesta tesi doctoral proporciona una exploració exhaustiva de les SCNB, des del disseny i l'optimització fins a les aplicacions pràctiques. Entenc tota la fenomenologia de les interaccions d'aquests materials periòdics amb ANC, HRs i 3D printing. En integrar tècniques avançades d'optimització i aprenentatge per reforç, l'estudi té com a objectiu millorar les solucions actuals de control de soroll.

Resumen

Los metamateriales acústicos, como los Cristales de sonido (SC), son estructuras artificiales periódicas diseñadas para controlar las ondas sonoras de maneras que los materiales naturales no pueden. Estos materiales exhiben propiedades únicas, como la refracción negativa y las Band Gaps (BG), que se pueden aprovechar para crear soluciones de control de ruido altamente efectivas. Estos Band Gaps (o bandas prohibidas en español) permiten prohibir la transmisión de ciertos rangos frecuenciales en determinadas direcciones de incidencia de la fuente sonora con respecto al crisal, lo que los hace ideales para aplicaciones en barreras de ruido y otros dispositivos acústicos. Esta investigación investiga el potencial de estos materiales avanzados para mejorar el rendimiento de los dispositivos de reducción de ruido mediante estrategias innovadoras de diseño y optimización, diseñados para minimizar el sonido no deseado, mejorando así el entorno acústico en diversos entornos. Más concretamente, dentro de los dispositivos de reducción de ruido, que abarcan barreras, absorbentes y difusores, esta tesis se centra en las barreras basadas en cristales de sonido (SCNB). El diseño y la optimización de estos dispositivos requieren una comprensión profunda de los principios acústicos y la capacidad de predecir cómo interactúa el sonido con diferentes materiales y estructuras. Para ello, es necesario la utilización de simulaciones que predigan el comportamiento y rendimiento de estos dispositivos, pudiendo asi ahorrar tiempo y dinero de tener que fabricar los diferentes diseños y tener que probar los prototipos experimentalmente para finalmente dar con la mejor solución para cada caso especifico. En esta linea,la tesis investiga el potencial de los sistemas de control activo del ruido (ANC), mejorados con técnicas de aprendizaje por refuerzo (RL), como un complemento que permita mejorar las SCNB. Al integrar el aprendizaje por refuerzo, el estudio tiene como objetivo desarrollar sistemas ANC que aprendan y se adapten continuamente a las condiciones ambientales cambiantes, proporcionando un enfoque dinámico y adaptativo para el control del ruido, con un especial foco en frecuencias bajas donde el control activo es más eficiente y donde las SCNB lo son menos.

Además del ANC, se incorporan Resonadores de Helmholtz (HR) para mejorar estas barreras. Gracias a la combinación de métodos númericos y algoritmos de optimización, no solo se mejora el rendimiento de las barreras de esta tipologia encontradas en la literatura sino que mejora la comprensión de los principios físicos que las gobiernan y su interacción con los HRs. Aprovechando los avances en la tecnología de impresión tridimensional (3D) en la ingeniería arquitectónica y mediante el uso de modelado paramétrico, la versatilidad aumenta enormemente en el proceso de creación de los prototipos que han sido resultados de las optimizaciones con los HRs. Esta tesis también aborda la capacidad de aislamiento de las SCNB hechas de dispersores cilíndricos con varios resonadores de Helmholtz, proponiendo un diseño con dispersores que incluyen dos resonadores de Helmholtz. Este diseño demuestra un aumento significativo en la Insertion Loss (IL) en comparación con las barreras convencionales.

La tesis también explora tanto numerica como experimentalmente, resultados de mediciones de incidencia de ondas para refinar aún más las estrategias de control de ruido. Se testea experimentalmente prototipos diseñados a mitigar un ruido tonal molesto como el de la frenada de los trenes, tanto en incidencia normal como incidencia difusa de las ondas sobre la barrera de SC. En resumen, esta tesis doctoral proporciona una exploración exhaustiva de las SCNB, desde el diseño y la optimización hasta las aplicaciones prácticas. Entiendo toda la fenomenologia de las interacciones de estos materiales periodicos con ANC, HRs y 3D printing.Al integrar técnicas avanzadas de optimización y aprendizaje por refuerzo, el estudio tiene como objetivo mejorar las soluciones actuales de control de ruido.

Sommario

I metamateriali acustici, come i *Sonic Crystals* (SC), sono strutture artificiali periodiche progettate per manipolare le onde sonore in modi che i materiali naturali non possono. Questi materiali consistono in reticoli di scatterers rigidi disposti nell'aria e mostrano proprietà uniche, come la riflessione negativa e le *Band Gaps* (BG), che possono essere sfruttate per creare soluzioni altamente efficaci per il controllo del rumore. Queste *Band Gaps* (o bande vietate) impediscono la trasmissione di determinate gamme di frequenze a seconda dell'angolo di incidenza delle onde sonore rispetto al cristallo, rendendole ideali per applicazioni in barriere antirumore e altri dispositivi acustici.

Questa ricerca indaga il potenziale di questi materiali avanzati per migliorare le prestazioni dei dispositivi di riduzione del rumore attraverso strategie di design e ottimizzazione innovative volte a minimizzare i suoni indesiderati, migliorando così l'ambiente acustico in vari contesti. In particolare, tra i dispositivi di riduzione del rumore, come barriere, assorbitori e diffusori, questa tesi si concentra sulle *Sonic Crystal Noise Barriers* (SCNB).

La progettazione e l'ottimizzazione di questi dispositivi richiedono una profonda comprensione dei principi acustici e la capacità di prevedere come il suono interagisce con diversi materiali e strutture. Questo è realizzato attraverso l'uso di simulazioni che prevedono il comportamento e le prestazioni di questi dispositivi, risparmiando tempo e risorse evitando la necessità di fabbricare e testare sperimentalmente più prototipi prima di arrivare alla soluzione ottimale per ogni caso specifico.

In linea con quanto sopra, la tesi esplora il potenziale dei sistemi di *Active Noise Control* (ANC) migliorati con tecniche di *Reinforcement Learning* (RL) come complemento per migliorare le SCNB. Integrando il *reinforcement learning*, lo studio mira a sviluppare sistemi ANC che apprendono e si adattano continuamente alle condizioni ambientali in cambiamento, fornendo un approccio dinamico e adattivo al controllo del rumore, particolarmente a basse frequenze, dove il controllo attivo è più efficace e dove le SCNB tendono a essere meno efficienti.

In aggiunta all'ANC, sono incorporati i *Helmholtz Resonators* (HR) per migliorare queste barriere. Combinando metodi numerici e algoritmi di ottimizzazione, non solo viene migliorata la prestazione delle SCNB già presenti in letteratura, ma si ottiene anche una comprensione più profonda dei principi fisici che le governano e della loro interazione con gli HR. La tecnologia di stampa 3D, utilizzata nell'ingegneria architettonica, combinata con la modellazione parametrica, aumenta notevolmente la versatilità nella creazione di prototipi risultanti da ottimizzazioni con gli HR.

Questa tesi affronta anche le capacità di isolamento delle SCNB realizzate con scatterers cilindrici dotati di più *Helmholtz Resonators*, proponendo un design che incorpora due HR per scatterer. Questo design mostra un significativo aumento dell' *Insertion Loss* (IL) rispetto alle barriere convenzionali. Inoltre, esaminando l'interazione tra le BG degli HR e le Bragg-BGs, questa tesi propone nuove applicazioni di trasmissione per gli SC multiresonanti oltre le barriere antirumore. La capacità di controllare la trasmissione attraverso un metamateriale attivo ruotando gli scatterers fornisce un vantaggio rispetto ai metamateriali passivi convenzionali.

Inoltre, la tesi esplora, sia numericamente che sperimentalmente, le misurazioni di incidenza delle onde per affinare ulteriormente le strategie di controllo del rumore. I prototipi progettati per mitigare il rumore tonale, come quello prodotto dal freno dei treni, sono stati testati sperimentalmente sia in incidenza normale che in incidenza diffusa delle onde sonore sulle SCNB.

In sintesi, questa tesi di dottorato fornisce un'esplorazione completa delle SCNB, dalla progettazione e ottimizzazione alle applicazioni pratiche. Si approfondisce la fenomenologia delle interazioni tra questi materiali periodici, ANC, HR e stampa 3D. Integrando tecniche avanzate di ottimizzazione e *Reinforcement Learning*, lo studio mira a migliorare le soluzioni attuali per il controllo del rumore.

Contents

Contents i

List of Figures iv

List of Tables viii

Abbreviations ix

List of Publications x

1 Introduction 1
- 1.1 Objectives 1
- 1.2 Thesis structure 3
- 1.3 Contributions 5

I Theoretical Concepts 7

2 Fundamentals of Acoustics 8
- 2.1 Wave Transmission in Uniform Linear Fluids 9
- 2.2 Periodic lattices and wave propagation 11
- 2.3 Local Resonators 16
- 2.4 State of Art of Sonic Crystal Noise Barriers 18

3 Strategies of Control; Metaheuristics Optimization, Modelling, and Methods 23
- 3.1 Heuristic Evolutionary Algorithms 24
- 3.2 Deep Reinforcement Learning 26
- 3.3 Numerical Methods 27
- 3.4 Parametric Design Process 35
- 3.5 Thesis Outline Methodology scheme 40

II Active Noise Control in Sonic Crystal Noise Barriers 41

4 Improving the Insertion Loss of Sonic Crystal Active Noise Barrier by Reinforcement Learning and Finite Difference Time Domain Simulations 42
4.1 Introduction . . . 42
4.2 Methodology . . . 46
4.3 Case Study: SCNB with ANC System . . . 50
4.4 Results . . . 53
4.5 Conclusion . . . 59

III Resonant Sonic Crystal Noise Barriers 60

5 Particle Swarm Optimization of Resonant Sonic Crystals Noise Barriers 61
5.1 Introduction . . . 61
5.2 Methodology . . . 63
5.3 Case Study: The SCNB Optimization module applying PSO Algorithm . . . 68
5.4 Results . . . 72
5.5 Discussion and Comparison . . . 79
5.6 Conclusion . . . 81

6 Parametric modelling of Resonant Sonic Crystal Noise Barriers. Case of Train Brake Noise 82
6.1 Introduction . . . 82
6.2 Materials and Methods . . . 86
6.3 Results . . . 99
6.4 Conclusions . . . 104

IV Multiresonant Scatterers in Sonic Crystal Transmission Applications 106

7 Increasing the Insertion Loss of Sonic Crystal Noise Barriers with Multiple Helmholtz Resonators 107
7.1 Introduction . . . 107
7.2 Methodology . . . 109
7.3 Bragg and Helmholtz resonances interaction . . . 112
7.4 SCNB scatterer with two HRs . . . 116

7.5 Conclusions 119
7.6 Appendix: Viscothermal Losses 120

8 Acoustic Switch based on Rotatable Sonic Crystal with Multiresonant Scatterers 122
8.1 Introduction 122
8.2 Methodology 124
8.3 Results 134
8.4 Conclusions 140

V Conclusions 141

Conclusions 143

References 143

List of Figures

2.1 2D Bravais lattices. 12
2.2 Constructive interference (left) and destructive interference (right) according to the angle of deviation. 13

3.1 FDTD scheme of pressure and particle velocity fields in 2D . . . 29
3.2 Adaptative FEM mesh of a 2D multiresonant scatterer unit cell. 32
3.3 Workflow of the parametric modelling methodology with numerical simulations. 36
3.4 Parametrized 3D model of the SCNB. 37
3.5 Parametrized 3D model of the SCNB. 37
3.6 Parametrized 3D model of the SCNB. 39

4.1 Main block diagram of the process of a generic RL system. . . . 46
4.2 The FDTD Environment of the SCNB with the ANC system. . 50
4.3 Training results of the DDPG agent. random frequencies of each episode a). Episode rewards (blue) and the cumulative average reward of all episodes(red) b). 54
4.4 Comparison between DDPG agent deployment performance along 21 episodes (100-500 Hz range) with different car velocities before training the agent a) and after training it b). 55
4.5 Insertion Loss of a SCNB of 3 rows with a moving source of 100, 110 and 120 Km/h incidence, with and without the ANC system working. 57
4.6 FDTD SPL maps at t = 30 ms with the car emitting noise at a frequency of 200 Hz. a) the ANC system switched off; b) the ANC system switched on. 58

5.1 2D Finite elements model of periodic sonic crystal noise barrier. 3 rows of scatters to be optimized and the distance between them too with the PSO algorithm. 64
5.2 Block diagram of the PSO process. 71

5.3 Particle Swarm optimization with 100 iterations and different populations and coefficients. 73
5.4 Convergence detail for the best configuration of coefficients and population. 74
5.5 Detail of the 2D model with the optimized SCNB. 75
5.6 Sound Insulation (SI) of the SCNB FEM simulation that maximizes the Fitness function. 76
5.7 Maps of Sound Pressure Level (dB) of the FEM model at maximum attenuation frequency (a) and Bragg's frequency (b). . . . 77
5.8 Genetic algorithm with 100 generation and different population sizes to optimize the SCNB model. 79
5.9 Box and whiskers plot of 4500 random simulations of the SCNB model and the best values of PSO and Genetic algorithm optimizations. 80

6.1 Chapter outline: the experimental part is in orange, and the numerical part is in green. 85
6.2 Periodic FEM generic parametrized 2D model. 87
6.3 2D design of a cylindrical scatter with a HR. 88
6.4 3D-printed prototypes with: (a) five rows; and (b) four rows of scatterers. 90
6.5 Emission and reception chambers. 91
6.6 Wood frame with the 3D-printed prototype inserted. 92
6.7 Measurement equipment. 93
6.8 Remote control acquisition software interface. 93
6.9 Numerical FEM model of the resonant scatter at 0° and 90°(upper part), simulation domain with the 4x12 SCNB at 0^{o}(middle part) and the three different barriers, CB, SCNB 0° and SCNB 90° (lower part). 94
6.10 3D Printed 1:2 scaled SCNB PLA prototypes a) Front view of the scaled SCNBs with the resonant cavity at 0^{o}; b) Top view of the scaled SCNBs at 0^{o} and 90^{o} configurations. 95
6.11 Experimental set up measurement system. up) SCNB measurement; down) CB measurement. 98
6.12 Transmission coefficient (τ) of four-row and five-row SCNBs with the FEM results and its experimental validation tests. 100
6.13 Insertion Loss of Numerical FEM Models with 0° SCNB (blue), 90° SCNB (red) and CB (black). 101

6.14 Band structure diagrams for 0° SCNB (left), 90° SCNB (right) both including the unit cell of the two-dimensional scatterer with LR, which forms the periodic system defining the SCNB and irreducible Brillouin zone of the square lattice SC based on the Bloch-Floquet theory for the calculation of the band structure. . 102
6.15 Insertion Loss of the experimental measurements, with 0° SCNB Experimental (blue dashed-dotted), 90° SCNB Experimental (red dash-dotted) and experimental CB (black dot-dashed). 103

7.1 a) Unit cell of the two-dimensional scatterer with HR, which forms the periodic system defining the SC and irreducible Brillouin zone of the square lattice SC based on the Bloch-Floquet theory for the calculation of the band structure. Numerical models for the SCNBs with 3-row scatterers for the evaluation of the IL with b) 0^{o} aligned and c) 90^{o} aligned HRs. 111
7.2 Transmission coefficient of the SCNB and band structure of the corresponding SC with **(left)** $f_{\text{HR}} < f_c$ and **(right)** $f_{\text{HR}} < f_c$ of the configurations with 0° alignment(blue) and 90° alignment (red). The SCNB-CC case is plotted in black for reference . . . 113
7.3 Insertion Loss of SCNB with varying HR resonant frequency for the configuration with **left**) 0° alignment and **right**) 90° alignment. The dashed vertical lines represent the lower and upper Bragg-BG limits of the SCNB-CC. The value of the theoretical resonant frequency of the HR is rep-resented by the white dotted line. 114
7.4 Insertion loss as a function of frequency of SCNBs with $f_{\text{HR}} < f_c$ (red) and $f_{\text{HR}} > f_c$ (blue) with l**eft**) 0° alignment and **right**) 90° alignment. The coloured area graphically represents the variance of the IL of the SCNB with HRs with respect to the SCNB-CC (dashed black). 115
7.5 Cylindrical scatterer consisting of two HRs with identical mouth and variable coupled surfaces through a rotating inner wall. . . 116
7.6 Insertion loss in colour scale as a function of frequency for SCNB with scatterers with coupled-surface HRs as a function of the inner wall rotation angle. (Right) Cases $\theta = 0°$ and $\theta = 180°$ and SCNB-CC.. 117
7.7 **Left**: Scatterer with HR with wider mouth ($w = 1$ cm) and. **Right**: Scatterer with HR with narrower mouth ($w = 1$ cm). HR1 and HR2 have the same resonance frequency $f_{\text{HR}} = 400$ Hz 120

7.8 Insertion Loss of a SCNB with HR1, used in the paper (blue) and with HR2, with a thin mouth (red) with (continuous) and without (circles) losses 121

8.1 a)Three Pareto points within a group, b) Pareto front. The red arrow indicates the direction that the optimization process should pursue, guiding the algorithm to generate new individuals and, as a result, achieve improved outcomes in subsequent generations of groups. 125
8.2 Flowchart of the process to optimize the behaviour of the multiresonant SC. 128
8.3 Brim that provides support and adhesion for the prototype on the print bed and initial layers(left). Almost completed prototype, with only a few layers remaining(right). 131
8.4 Continuous extruder path(left); Digital image of multiple overlapping layers (center); Zoom on the toolpath during the transition, with continuous flow, from one layer to another(right). . 131
8.5 Experimental set up. 133
8.6 Pareto Front variation with colours depending on the generation. 135
8.7 Band diagram comparison before (left) and after optimization process (right). 136
8.8 Transmittance, Numerical and Experimental (up); Optimization objectives, Numerical and experimental (down). 138
8.9 Insertion Loss of the Multiresonant SC with scatterers at 0^{o} and 90^{o}. 139

List of Tables

2.1 Summary of some crystal nose barriers, their noise control mechanisms, and materials 20

3.1 Transmission cases in Sonic Crystals 40

4.1 DDPG Hyperparameters 53

5.1 Normalized Traffic Noise Spectrum 69
5.2 Optimal Parameters X_{optim} that maximize the DL_{SI} 75
5.3 Categories of noise barrier according to their airborne Sound Insulation. 78

Abbreviations

ANC	Active Noise Control
BG	Band Gap
DDPG	Deep Deterministic Policy Gradient
DRL	Deep Reinforcement Learning
evMOGA	Evolutionary Multi-Objective Genetic Algorithms
FDTD	Finite-Difference Time Domain
FEM	Finite Element Method
FOH	Front of House
GA	Genetic Algorithm
HR	Helmholtz Resonator
IL	Insertion Loss
IPW	Incident Plane Wave
LR	Local Resonator
MS	Multiple Scattering
NB	Noise Barrier
NRD	Noise Reduction Devices
PA	Public Address
PML	Perfectly Matched Layer
PSO	Particle Swarm Optimization
RC	Resonant Cavity
SC	Sonic Crystal
SCNB	Sonic Crystal Noise Barrier
TL	Tranmission Loss

List of Publications

International Journals

1. **D. Ramírez-Solana**, J. Redondo, A. M. Mangini, and M. P. Fanti, "Particle Swarm Optimization of Resonant Sonic Crystals Noise Barriers," IEEE Access, vol. 11, pp. 38426–38435, 2023, doi: 10.1109/ACCESS.2023.3267972.

2. J. Redondo, **D. Ramírez-Solana**, and R. Picó, "Increasing the Insertion Loss of Sonic Crystal Noise Barriers with Helmholtz Resonators," Applied Sciences, vol. 13, no. 6, p. 3662:1-3662:13, Mar. 2023, doi: 10.3390/app13063662.

3. **D. Ramírez-Solana**, V. Sangiorgio, N. Parisi, J. Redondo, A. M. Mangini, and M. P. Fanti, "Parametric Design and Assessment of 3D Printable Open Noise Barrier: Device Customization to Protect Buildings from Train Brake Noise," Journal of Architectural Engineering, vol. 30, no. 2, 2024, doi: 10.1061/JAEIED.AEENG-1605.

4. **D. Ramírez-Solana** et al., "Sonic Crystal Noise Barrier with Resonant Cavities for Train Brake Noise Mitigation," Applied Sciences, vol. 14, no. 7, p. 2753, Mar. 2024, doi: 10.3390/app14072753.

5. **D. Ramírez-Solana**, J. Galiana-Nieves, J. Redondo, A. M. Mangini and M. P. Fanti, "Improving Insertion Loss of Sonic Crystal Active Noise Barrier by Reinforcement Learning and Finite Difference Time Domain Simulations," IEEE Access, vol. 12, pp. 77988-77998, 2024, doi: 10.1109/ACCESS.2024.3406857.

6. J. La Roda Mauro, **D. Ramírez-Solana**, and J. Redondo, "Low Frequency Sound Wave Propagation at Open Air Concerts: Acoustic Metamaterial's audience phenomenon," Journal of Acoustical Engineering Society, vol. 72, no. 11, pp. 767-775, 2024, doi: 10.17743/jaes.2022.0173.

7. **D. Ramírez-Solana**, V. Sangiorgio, R.Picó and J. Redondo, "Acoustic Switch based on Rotatable Sonic Crystal with Multiresonant Scatterers," Applied Acoustics, 2025, *Submitted*.

International Conferences

1. **D. Ramírez-Solana**, S. Castiñeira-Ibáñez, J. M. Bravo-Plana-Sala, J. V. Sánchez-Pérez, J. Redondo, and R. Picó, "Analysis of the interaction of helmholtz resonators in periodic acoustic metamaterials depending on its orientation with the acoustic source.," Internoise, vol. 263, no. 6, pp. 215–226, Aug. 2021, doi: 10.3397/IN-2021-1369.

2. J. Galiana Nieves, J. Redondo, D. Benítez Aragón, **D. Ramírez-Solana**, and J. M. Herrero, "Evolutionary optimization processes for acoustic applications where size matters," Internoise, vol. 265, no. 3, pp. 4125–4135, 2022, doi: 10.3397/IN_2022_0589.

3. **D. Ramírez-Solana**, J. Galiana Nieves, J. Redondo, R. Picó, A. M. Mangini, and M. P. Fanti, "Análisis numérico del aislamiento producido por barreras basadas en cristales de sonido en incidencia oblicua," in Proceedings of Tecniacustica 2022, Elche (Spain), 2022.

4. J. Galiana-Nieves, R. Del Rey, J. Alba, **D. Ramírez-Solana**, and J. Redondo, "Evaluación de la Reducción Sonora Proporcionada por Materiales con Alta Permeabilidad Acústica," in Proceedings of Tecniacustica 2022, Elche (Spain), 2022.

5. **D. Ramírez-Solana**, J. Galiana-Nieves, J. Redondo, A. M. Mangini, and M. P. Fanti, "On the Optimization of Sonic Crystal Acoustic Noise Barriers," Internoise, vol. 265, no. 4, pp. 3821–3832, 2022, doi: 10.3397/IN_2022_0540.

6. **D. Ramírez-Solana**, V. Sangiorgio, J. Redondo, M. P. Fanti, A. M. Mangini, and T. D. Noia, "The 3D Printed Sonic Crystal Noise Barrier," in Atti AIA (Associazione Italiana Acustica), Matera (Italy), 2022.

7. J. Galiana-Nieves, **D. Ramírez-Solana**, R. Picó, and J. Redondo, "Periodic Boundary Conditions implementation for the study of sonic crystals," in Proceedings of the 10th Convention of the European Acoustics Association Forum Acusticum 2023, Turin, Italy: European Acoustics Association, 2023, pp. 3835–3840. doi: 10.61782/fa.2023.0810.

8. **D. Ramírez-Solana**, J. Galiana-Nieves, J. Redondo, R. Picó, A. M. Mangini, and M. P. Fanti, "Dispositivo de Filtrado Sintonizable Basado en Cristal De Sonido Multiresonante," in Proceedings of Tecniacustica 2023, Cuenca (Spain), 2023.

9. **D. Ramírez-Solana**, J. Galiana-Nieves, J. Redondo, A. M. Mangini, and M. P. Fanti, "Reinforcement learning applied to an Active Noise Control system in Sonic Crystal Noise Barriers" in Proceedings of the 10th Convention of the European Acoustics Association Forum Acusticum 2023, Turin, Italy: European Acoustics Association, 2023, pp. 925–931. doi: 10.61782/fa.2023.0714.

10. J. Redondo, J. Galiana-Nieves, **D. Ramírez-Solana**, R. Picó, "Estándares De Medida De Aislamiento De Pantallas Acústicas: "El Bueno, El Feo Y El Malo", in Proceedings of Tecniacustica 2024, Faro (Portugal), 2024.

1 Introduction

1.1 Objectives

The primary objective of this thesis is to carry out a thorough review of the existing literature to define the current state of the art regarding sonic crystals, focusing on the analysis of their challenges and applications. This review will provide a comprehensive background, contextualizing the problem within the broader field of noise control technologies. Specifically, it will explore the relationship between sonic crystals and their usage in noise barriers, active noise control systems, and transmission phenomena. The research will delve into the existing solutions, with particular attention to the utilization of resonant cavities and Helmholtz Resonators (HRs), which have proven to enhance the performance of sonic crystals in addressing transmission-related issues. By identifying key challenges and gaps in current approaches, this objective will set the foundation for further developments in the field.

The second objective is to develop simplified two-dimensional acoustic simulation models that are computationally efficient. These models will play a crucial role in the subsequent stages of the research, as they are intended to be used in multiple calls from optimization processes. Computational efficiency is essential to improve the transmission performance of sonic crystals in real-life applications. Therefore, the models must be both practical and effective, balancing accuracy with computational cost.

Another essential aspect of this research involves conducting a detailed analysis of each case study to make informed decisions regarding the most suitable simulation technique. This step requires evaluating the Finite Element Method (FEM) or the Finite-Difference Time-Domain (FDTD) method, based on the specific requirements of each case. Moreover, this objective will focus on selecting the most appropriate optimization procedure, determining whether artificial intelligence techniques like Deep Reinforcement Learning (DRL) should be utilized or whether heuristic and evolutionary algorithms, such as Genetic Algorithms (GA) or Particle Swarm

Optimization (PSO), offer more practical solutions. The selection of these methods will be case-specific, ensuring that the approach is tailored to the unique characteristics of each study.

An equally important objective of this thesis is to modify and adapt each optimization process according to the specific requirements of the case studies. This will involve the interconnection of various software tools to facilitate different parts of the optimization process, such as acoustic numerical simulation and parametric modeling. The development of customized workflows will streamline the entire process, thereby improving overall efficiency and reducing computational cost. The optimization procedures will be adapted not only to enhance numerical accuracy but also to improve the performance of the metamaterials under investigation. In addition to using conventional tools, this objective will emphasize the need for seamless integration between the diverse software employed, ensuring that each tool effectively complements the others in producing optimal solutions for the case studies. The goal is to create an interconnected framework that is highly adaptable and capable of producing results with greater accuracy and efficiency, which will serve as a stepping stone for future research in this area.

Lastly, the final objective is to conduct experimental tests under various acoustic wave incidences in order to validate the numerical results obtained from the simulations. These experiments will be critical in verifying the accuracy of the developed models and optimization procedures. While the research will adhere to existing International Standards, it also recognizes that traditional testing standards may not always be appropriate for evaluating the performance of advanced metamaterials such as sonic crystals. As a result, this objective aims to propose new strategies for experimental testing, ensuring that the tests are well-suited to the unique characteristics of metamaterials. By doing so, the research will bridge the gap between numerical simulations and real-world applications, providing a more comprehensive understanding of the performance of sonic crystals in practical settings.

1.2 Thesis structure

The primary focus of this thesis is to examine the use of optimization algorithms across a range of Sonic Crystal wave transmission's applications, with a special focus in their use as Noise Barriers.

The **first part** of this thesis provides the theoretical background and the overview of the methodology applied.

The **second part** of this thesis delves into the automatic control of loudspeakers with Artificial Intelligence in the low-frequency regime of Sonic Crystal Noise Barriers without HRs.

In Chapter 4 the case study involves the use of loudspeakers to implement an Active Noise Control (ANC) system, controlled by Deep Reinforcement Learning, that complements a Sonic Crystal Noise Barrier. In the low-frequency range of the car traffic noise spectrum (100 - 500 Hz), adaptive scenarios of moving noise sources (motor vehicles) with different frequencies and diverse vechicles velocities are addressed. With this moving sources and varying velocities approach more realistic situations are studied. The time-varying models are simulated by employing finite-difference time-domain (FDTD) method.

The **third part** of this thesis delves into contributing to the improvement of the feasibility of Noise Barriers made from Sonic Crystals with Resonant Cavities in two different noise mitigation scenarios; Traffic Noise and Train Brake Noise.

In Chapter 5, the application of Swarm algorithms in a Resonant Sonic Crystal Noise Barrier is explored. A detailed framework, based on Finite Element Method (FEM) simulations to construct Noise Barriers utilizing Sonic Crystals is presented. Within this framework, the issue of the scatterer's topology parameters, including a Helmholtz Resonator embedded is addressed by the deployment of a Particle Swarm Optimization (PSO) algorithm. The novelty of this work lies in the synergistic use of FEM models for acoustic simulation, and PSO to determine the scatterer's topology parameters that define the integrated resonant cavity, with the aim to optimize the insulation offered by the barrier according to a single objective parameter based on an International Standard, while ensuring the barrier remains competitive with conventional ones in terms of width. The proposed PSO algorithm can be executed in a script that invokes the simplified numerical model multiple times, to enhance efficiency and expedite convergence

time. Lastly, a comparison with a MonoObjective Genetic Algorithm (GA) is carried out, demonstrating the superiority of PSO in circumventing local solutions and delivering a better global solution.

Chapter 6 discusses the complete process of designing and prototyping noise barriers based on Sonic Crystals with resonant cavities. This includes parametric modeling, Finite Element Method (FEM) simulations, and subsequent experimental validation. It analyzes different types of acoustic wave incidences and different orientations of the resonant cavity with respect to the incident wave. This methodology is applied to the case of train braking noise, a tonal rough noise.

Chapter 7 delves into the enhancement of noise insulation properties of Sonic Crystal Noise Barriers (SCNBs) through the integration of multiresonant Scatterers with two Helmholtz Resonators (HRs). The chapter focuses on the interaction between Bragg scattering and local resonance phenomena, which can either amplify or diminish the barrier's effectiveness based on its design. It identifies key factors influencing this interaction, specifically the orientation of the resonator mouth relative to the incident wave and the resonance frequency of the HR in relation to the Bragg-bandgap (Bragg-BG). The main findings reveal that optimizing these parameters can significantly boost the Insertion Loss of SCNBs. Also it propose a novel design featuring scatterers equipped with two HRs, demonstrating a substantial 20 dB increase in noise reduction within the Bragg-BG compared to traditional barriers. This chapter provides a comprehensive analysis of the conditions necessary to maximize the acoustic performance of SCNBs, offering valuable insights for future noise mitigation solutions.

Lastly, in chapter 8, both numerical and experimental analysis explore an additional application beyond the previous chapter 7, which was solely numerical but helped to understand the physical phenomena behind the interaction between HRs and Bragg BGs. After examining this interaction, the study proposes new transmission applications for multiresonant SCs beyond noise barriers. The ability to control transmission in particular ranges through an active metamaterial by rotating the scatterers provides an advantage over conventional passive metamaterials.

1.3 Contributions

The main contributions of this thesis include the following:

In-depth exploration of Sonic Crystal Noise Barriers (SCNBs): The study delves into the design and optimization of SCNBs, which are advanced materials with unique properties that can significantly reduce noise transmission. By focusing on these metamaterials, the research aims to enhance the performance of existing noise reduction solutions.

Integration of Active Noise Control (ANC) and Reinforcement Learning (RL): The thesis proposes the use of ANC systems augmented with RL techniques to improve the efficiency of SCNBs, particularly at low frequencies. This approach allows for dynamic and adaptive noise control strategies that respond effectively to changing environmental conditions. An advancement over what has been published so far is the use of artificial intelligence with finite dimensions acoustic numerical models in the time-domain that are not a unit cell, employing reinforcement learning instead of solely machine learning.

Combination with Helmholtz Resonators (HRs): The research combines numerical methods and optimization algorithms to analyze the interaction between SCNBs and HRs, leading to improved barrier performance. This integration expands the understanding of the underlying physical principles governing these systems and their potential synergies.

Advanced prototyping through 3D printing and parametric modeling: The study leverages the versatility of 3D printing technology and parametric design to create innovative prototypes based on optimized structures. This enables the production of complex shapes and configurations that were previously difficult or impossible to achieve with conventional manufacturing methods.

Evaluation of insulation capabilities with multi-resonator cylindrical scatterers: By proposing a design with two Helmholtz resonators per scatterer, the thesis demonstrates a substantial increase in Insertion Loss (IL) compared to conventional barriers. This opens up new possibilities for the application of multiresonant sonic crystals in various transmission scenarios.

Experimental analysis of wave incidence: The thesis includes both numerical simulations and experimental work to investigate the impact of different wave incidences on the effectiveness of SCNBs. This is particularly relevant for designing barriers capable of handling tonal noise, such as that produced by train braking, under various real-world conditions.

Contributions to the theoretical and practical knowledge of

acoustic metamaterials: Through the analysis of the interactions between SCNBs, ANC, and HRs, this research advances the state-of-the-art in acoustic metamaterials and provides valuable insights for the design and implementation of future noise reduction technologies.

Limitations acknowledged in the thesis include the complexity of simulating real-world environments and the potential for discrepancies between theoretical predictions and experimental results due to fabrication imperfections and environmental factors. However, these limitations are addressed by employing robust numerical methods and validating findings through experimental testing, ensuring that the contributions remain relevant and applicable to practical scenarios.

After understanding the interaction between the band gaps of Helmholtz resonators and those of Bragg scattering, and thanks to the appropriate combination, additional transmission applications beyond noise barriers are also proposed, using multiresonant sonic crystals. The transmission control through an active metamaterial, which can be altered by rotating the scatterers, offers an advantage over traditional passive metamaterials.

In summary, the thesis provides significant advancements in the field of acoustic metamaterials and noise control by integrating sonic crystal technology with active control systems and exploring the influence of wave incidence. The work is expected to have a substantial impact on the design and optimization of noise reduction devices, leading to quieter and more comfortable environments in various industrial and urban settings.

Part I

Theoretical Concepts

2 Fundamentals of Acoustics

Acoustics is the science that deals with the study of sound, its production, transmission, and effects. It encompasses a wide range of phenomena, including the behaviour of sound waves in different media, the principles of wave propagation, and the interaction of sound with materials. The fundamental principles of acoustics are rooted in physics, particularly in the areas of wave mechanics and vibrations. Understanding these principles is essential for developing effective strategies for controlling sound transmission, which is the one of the focus of this thesis.

Sound transmission refers to the passage of sound waves through a medium, which can be solid, liquid, or gas. This phenomenon contrasts with sound absorption, where energy is dissipated within a material, and reflection, where sound waves bounce back from surfaces. In the context of this research, transmission control in periodic acoustic structures is crucial for optimizing the efficiency of noise reduction devices. By manipulating the transmission properties of these structures, it is possible to enhance their performance in practical applications.

2.1 Wave Transmission in Uniform Linear Fluids

Acoustic waves are a form of mechanical energy transmission through a medium, such as through adiabatic compression and decompression in fluids. This transmission occurs due to particle vibrations around their equilibrium positions, assuming the medium's elasticity. Therefore, in an elastic medium, sound waves cause pressure variations, leading to dynamic pressure deviations from the local ambient or static pressure [1]. For this discussion, we will focus on wave propagation in air. The following properties of air are relevant:

- Air is a homogeneous and isotropic fluid, meaning its properties are spatially uniform and directionally independent.
- Air behaves as an ideal fluid: inviscid, lossless, and without dissipative effects due to viscosity ($\mu_0 = 0$).
- Pressure and density perturbations are small compared to the average atmospheric values [1].
- Changes of state are adiabatic, meaning no heat exchange occurs between regions of low and high pressure due to the rapid motion of particles[2].

The sound pressure at a given point and time, t, can be expressed as:

$$p(x,t) = p'(x,t) - p_0 \tag{2.1}$$

where x is the position, p_0 is the atmospheric pressure.

The Wave propagation equation

The comprehensive equation that describes wave propagation can be derived by combining the continuity equation, also known as the conservation of mass law, with Euler's equation of fluid dynamics. The continuity equation expresses the relationship between the particle velocity ν due to the compression and expansion of the fluid. It states that the rate of change of mass within a given volume equals the mass flow through the volume:

$$\frac{\partial \rho}{\partial t} = -\rho_0 \nabla \cdot \nu \tag{2.2}$$

where $\rho = \rho_0$ is the instantaneous air density. The linear form of Euler's equation, also known as the conservation of momentum [1], is the second fundamental law and is given by:

$$\rho_0 \frac{\partial \nu}{\partial t} = -\nabla p \tag{2.3}$$

Here, ρ_0 is the static air density, $\nu(x,t)$ is the particle velocity vector field, and $p(x,t)$ is the sound pressure. Assuming the fluid is inviscid, meaning rotational effects can be neglected, and the particle velocity $\nu(x,t)$ is irrotational ($\nu = -\nabla u$, where u is the velocity potential), equation 2.3 can be rewritten as:

$$p = -\rho_0 \frac{\partial u}{\partial t} \tag{2.4}$$

Combining equations 2.2 and 2.3, we obtain the wave equation for a continuum medium, which describes wave propagation in a homogeneous fluid. This second-order, linear, partial differential equation for mechanical waves can be written in its general three-dimensional form as:

$$\frac{\partial^2 p}{\partial t^2} = c^2 \nabla^2 p \tag{2.5}$$

where p represents the instantaneous pressure deviation from equilibrium, t is time, c is the speed of sound in the fluid, and ∇^2 is the Laplacian operator (denoting the spatial Laplacian, or the divergence of the gradient). Equation 2.5 is the time-dependent form of the wave equation. Typically, sound pressure is assumed to be a time-harmonic signal of the form:

$$p(x,t) = P(x)e^{-i\omega t} \tag{2.6}$$

where P is the pressure amplitude and ω is the angular frequency of oscillation. Equation 2.6 can be expressed in its time-independent form as:

$$p(x,t) = P(x)e^{-ikx} \tag{2.7}$$

where kx is the scalar product of the position vector x and the wave number k. This plane wave solution describes a harmonic sound wave that remains unchanged across each plane normal to the propagation vector k. By combining equations 2.5 and 2.6, we obtain the Helmholtz equation, defined as:

$$\nabla^2 p = -k^2 p \tag{2.8}$$

2.2 Periodic lattices and wave propagation

The study of periodic lattices, whether they are naturally occurring like crystals or artificially arranged networks, has a diffuse origin deep in the past. However, one of the seminal studies on the arrangement of elements in such structures was conducted by Auguste Bravais, who introduced the concept of a Bravais lattice in 1850[3].

Bravais lattices

A Bravais lattice is an infinite array of discrete points generated by a set of discrete translation operations in three-dimensional space. This concept is fundamental in the study of crystalline structures, as it provides a mathematical framework to describe the periodic arrangement of atoms or molecules in a crystal. Bravais discovered that there are 14 different ways to arrange atoms in three-dimensional space, known as the 14 Bravais lattices. This thesis focuses on two-dimensional crystals, so the 5 types of Bravais lattices in two dimensions are shown below, according to the angles (α) and the distance between nodes, known as lattice constant (a):

a) **Square lattice**, $a_1 = a_2$ $\alpha = 90$

b) **Rectangular lattice**, $a_1 \neq a_2$ $\alpha = 90$

c) **Hexagonal lattice**, $a_1 = a_2$ $\alpha > 90$

d) **Centered rectangular lattice**, $a_1 \neq a_2$
$\alpha = 90$

e) **Oblique lattice**, $a_1 = a_2$ $\alpha < 90$

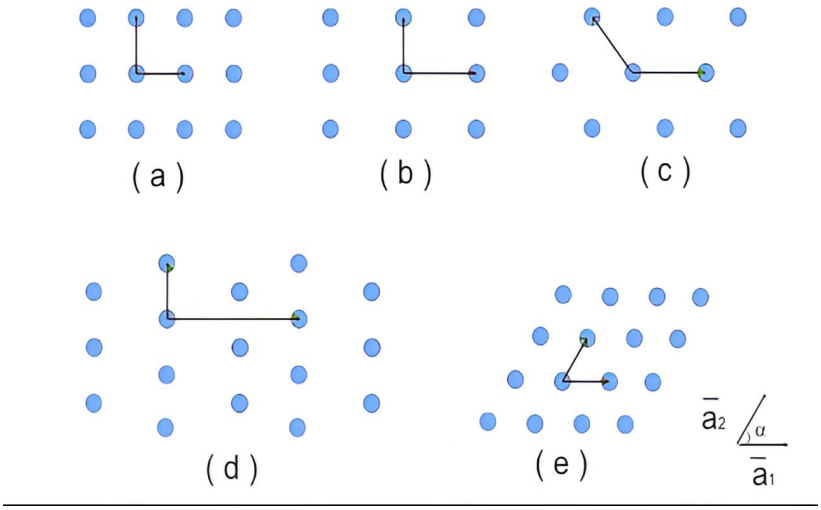

Figure 2.1: 2D Bravais lattices.

The concept of a Bravais lattice is closely related to the field of acoustics. (CAMBIAR)

Phononic crystals possess a unique structure that is characteristic of a periodic lattice, featuring elements distributed in a regular and repetitive manner in space, known as acoustic scatterers. In nature, we find a large number of solids with this atomic structure, the crystalline solids. Depending on the number of directions in which the repetition of scatterers occurs, Phononic crystals can be one-dimensional (1D), two-dimensional (2D), or three-dimensional (3D).

Multiple scattering

Multiple scattering (MS) is a phenomenon that occurs when waves interact with a medium composed of discrete scatterers, such as the atoms in a crystal lattice. In phononic crystals with perfect lattices, quantum-mechanical methods, which were developed to analyze scattering of elementary particles in crystals, can be used to describe the scattering of photons [4]. The periodicity of the lattice plays a crucial role in the scattering process, as it can lead to constructive and destructive interference patterns. If the incident wavelength is comparable to the lattice constant (a) in the direction of wave propagation, multiple scattering generates a new wave, due to the destructive and constructive interferences that occur within the crystal, which travels in the opposite direction to the incident wave.

The interaction of sound waves with these scatterers significantly affects the material's acoustic properties. Researchers employ sophisticated meth-

ods, such as Bloch-Floquet theory, to analyze this phenomenon [5]. Based on the Bloch-Floquet theory the calculation of the band structure can be perform, according to the unit cell of the scatterer, which forms the periodic system defining the crystal and its irreducible Brillouin zone [6] and depends on the lattice constant (a). The band-structure results reveal allowed and forbidden frequency ranges. The forbidden ones are called Band Gaps (BGs) for acoustic waves in the periodic composite.

These BGs arise due to constructive or destructive interference of scattered waves, leading to reduced transmission at specific frequencies, and their central frequency can be deduce by the Bragg's law.

Bragg's law

Assuming crystalline structures like phononic crystals in which waves impinge and are reflected in other directions from the parallel planes of the scatterers that form the crystal, Bragg's Law [7] allows us to study the directions in which constructive interferences occur. For an interference to be constructive, the path difference between the reflected wavefront must be an integer multiple, n, of wavelengths λ.

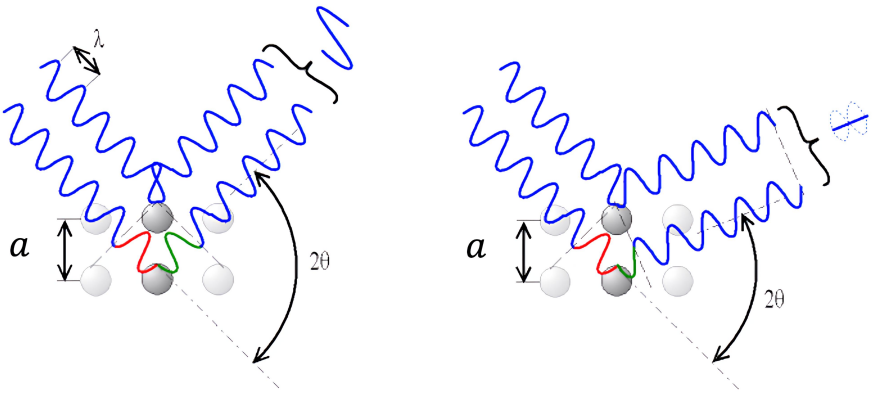

Figure 2.2: Constructive interference (left) and destructive interference (right) according to the angle of deviation.

The mathematical expression where crystals have square lattice is as follows:

$$2a \sin\theta = n\lambda \tag{2.9}$$

where a represents the lattice constant, θ is the angle formed by the incident wave and the reflected wave, and λ is the sound wavelength [8].

It is observed, therefore, that Bragg reflection only occurs if the wavelength λ is at least twice the distance between parallel planes of the crystal and for certain values of the angle θ.

For the present thesis in most of the cases normal wave incidence will be considered, the case $n = 1$ is studied, where the previous equation becomes:

$$2a = \lambda = \frac{c}{f_c} \rightarrow f_c = \frac{c}{2a} \tag{2.10}$$

where c is the speed of sound propagation and f_c is the central frequency of the first Bragg-BG . Therefore, for certain frequencies, given by equation 2.10, and due to the periodicity of the crystal, when the Bragg condition is satisfied, a standing wave will be formed by successive reflections and the aforementioned destructive interferences. These frequency intervals are the previously explained Bragg-Band Gaps (Bragg-BGs). Equation 2.10 refers to the 1^{st} Bragg-BG, while the second would be found for $n = 2$, clearing from equation 2.9, and so on.

The periodic distribution of the scatterers of a crystal is immersed in a host medium with distinct physical properties. This structural relationship between the scattering medium and the scatterers determines the topology of the network, which can be:

- **Cermet topology**, where the scatterers are isolated inclusions, embedded in the host material of less density.
- **Network topology**, where the scatterers with higher density are connected, forming a continuous network throughout the structure with the periodic inclusions of less density.

The Cermet topology is more conducive to the formation of elastic/acoustic stop-bands, while the Network topology is more advantageous for generating optical band gaps in photonic crystals and for electromagnetic waves [9, 10].

This thesis focuses in a specific case of phononic crystals called **Sonic Crystals** (SC) and its acoustic wave manupulations, with a special foucs in transmission situations. In particular, on two-dimensional SCs with Cermet topology, as the rigid scatterers are embedded in air, which is the host material through which sound is transmitted.

Sonic Crystals

As mentioned before, an specific case inside of phononic crystals, are Sonic Crystals (SCs), where the acoustic scatterers of higher density are embedded

in air as a host medium [11, 12]. SCs can play a pivotal role in manipulating the propagation of acoustic waves. Through their intricate design, SCs can effectively modulate various properties of sound, including its frequency, directionality, and attenuation. Since 1949 when SC acoustic lens where studied by Kock and Harvey [13], their versatility has led to their widespread adoption in a varied scope of applications, spanning from noise control to the creation of acoustic filters [14], diffusers [15], noise barriers [16] and waveguides [17].

Throughout this thesis, only two-dimensional SCs are considered. Although the periodicity is in two dimensions (x,y), the scatterers are extruded along the z-axis. This results in cylindrical scatterers, which in some cases, have resonant cavities.

2.3 Local Resonators

Resonance-based metamaterials are specially engineered structures designed to selectively absorb certain sound wave frequencies. By modifying the geometrical dimensions and characteristics of the resonators, these materials can be customized to absorb undesired frequencies while permitting others to pass through [1]. Their function is based on localized resonances, where particular structural elements interact with sound waves at specific frequencies. These resonances lead to increased absorption or reflection, depending on their intended use. In this thesis, two types of local resonators, the Continuous Cavity Resonator(CCR) and the Helmholtz Resonator (HR) [18], are examined for complementing the SCs. The main difference between this two types is that Helmholtz resonators have well-differentiated parts and can be tuned using an equation 2.12 , while so-called CCRs arise from parametric optimizations and modeling in which the final shape does not allow differentiation between the neck of the resonator and the internal resonant cavity.

Helmholtz Resonators

Helmholtz resonators (HRs) have the remarkable capability to vibrate at frequencies where the wavelengths are much larger than the resonator's own physical size. This unique feature has led to their extensive use in the design of acoustic metamaterials, which are, by definition, smaller than the wavelength in both size and dimensions.

The basic structure of a Helmholtz resonator consists of two main parts: a cavity with stiff walls and a protruding neck. This particular configuration enables HRs to vibrate at specific frequencies, similar to a mass-spring system. The air in the resonator's neck acts as the oscillating mass, while the adiabatic compression of air within the cavity serves as the spring constant.

When an acoustic wave hits the resonator, the Helmholtz resonator reacts like a force, causing the air mass in the neck to move. As the mass descends, it reduces the volume of the cavity, thereby increasing the pressure. This cycle continues until the pressure is high enough to push the mass back into the cavity.

The resonance frequency of a Helmholtz resonator can be calculated based on its geometric parameters [1]:

$$f_{\text{res3D}} = \frac{c}{2\pi}\sqrt{\frac{S_H}{L_H \cdot V}} \tag{2.11}$$

In this context, S represents the cross-sectional area of the neck, L_H denotes the effective length of the neck (that needs a correction factor), and V_H signifies the volume of the cavity. This particular interpretation does not take into account any Viscothermal losses (see 3.3) that may occur within the neck and the cavity.

In this thesis, two-dimensional scatterers with HRs are employed, so in 2D the HR is characterized by the length of the neck L, the width of the mouth w, the inner surface area ($S = \pi r^2$), where r is the inner radius of the surface of the HR. The first resonance frequency of the resonator is given by [2]:

$$f_{\mathrm{HR}} = \frac{c}{2\pi}\sqrt{\frac{w}{L + \frac{\Delta w}{2}S}}, \tag{2.12}$$

where Δ is the correction factor for neck length added account for the effects of the neck-cavity junction caused by a sudden change in the circular cross-sections (usually between 1.6 and 1.8) [19].

2.4 State of Art of Sonic Crystal Noise Barriers

Noise is defined as an undesired outdoor sound produced by human activities that can affect quality of life due to its unpleasant effects on human health [20]. When it is not possible to mitigate the noise at the source, the most common and useful option used to be acting during its transmission phase, placing noise barriers (NB) [21]. The principle of operation is based on locating the barrier between the noise source and the receiver, such that a significant amount of the noise energy is reflected, while other amounts are diffracted from the edge of the barrier, transmitted through it, or dissipated by the rigid material which the barrier is made. However, due to the fact that classical NBs are always formed by continuous flat walls of dense materials [22], some aesthetic inconveniences occur. Furthermore, fluids or light cannot flow through classical NBs, and they not discriminate between different noise types in different frequency ranges [23]. To solve these problems, noise barriers based on Sonic Crystals (SC) have been proposed. SC as previously explained, can exhibit peculiar transmission properties, and the main noise control mechanism is based on Bragg interferences, due to multiple scattering (MS) [8, 24]. MS phenomena produce destructive interferences such that waves at those specific frequency ranges cannot propagate through the structure. These ranges are called Bragg band gaps (Braag-BG) and depend on the distance between scatterers, which is called the "lattice" constant (a) [9, 25].

The first Sonic Crystal Noise Barrier (SCNB), proposed in 1997 by Kushwaha [26], was a theoretical study and the first prototype designed and experimentally tested was by Sánchez-Pérez in 2002[16]. The scatterers of the SCNB were cylindrical rigid scatterers, and the position and size of the BG in the frequency spectrum were determined by the wave angle or incidence, radius of cylinders, and distance between the scatterers. A cylindrical shape enables a wide scope of materials that don't require significant modification to set up the periodic structure of the SCNB, e.g., using rods of PVC [27], wood [28], aluminium [29], recycled materials [30], or natural materials like bamboo rods [31], or maritime timber logs [32]. In all these cases, the barriers were manufactured without 3D-printing technology. However, the MS noise control mechanism is not sufficient for achieving a performing noise barrier. Consequently, two new mechanisms were added to SCNB by Romero-Garcia et al. [14]: Helmholtz resonances and absorbent materials modifying the scatterers' design. The new multi-phenomena scatterers were more complex, changing from cylindrical to C-Shape and having iron

cylinders with an aperture, usually with a resonant cavity in the centre of the cylinder. They were covered by rock wool, produced for a specific case and modified by hand [33]. It was the beginning of what can be called the second generation of SCNB. However, they are produced with rigid materials similar to the first generation and modified, e.g., bamboo resonant rods [31], Elastic Beams Of Low-Density Polyethylene Foam (LDPF) with handmade resonant cavities [34], or steel cylinders with a C-shape aperture [35]. In most of the mentioned literature, the simulations were usually performed by the Finite Element Method (FEM), one of the most used numerical techniques in acoustics. This method is used to solve partial differential equations numerically, in which small, discretized areas of the domain provide an approximate solution of the differential equations. This meshing technique enables the description of complex geometries and is a reliable method to determine the sound pressure fields using sonic crystals [36].

To summarize all the previously mentioned works related to SCNB, Table 1 exposes the noise control mechanisms and the materials used. In all the cases showed in Table 1, the geometrical topology of the scatter was defined for a specific Helmholtz resonance frequency, as well as other parameters like the distance between the scatterers (lattice constant) for BG frequencies, number of rows, or height of the barrier. In doing this, every prototype was applicable for a single case study only and it is necessary to redesign the system for every different application.

Table 2.1: Summary of some crystal nose barriers, their noise control mechanisms, and materials

Author (year)	**Multiple scattering**	**Resonators**	**Absorbent**	**Materials**
Sanchez-Perez et al. (2002)	Yes	No	No	PVC
Umnova et al. (2006)	Yes	No	Yes	Fibrous woolen felt
Chalmers et al. (2009)	Yes	Yes	No	Iron cylinders
Sanchez-Dehesa et al. (2011)	Yes	No	No	Metal shells filled with rubber crumb
Romero-García et al. (2011)	Yes	Yes	Yes	PVC and woollen felt cover
Castiñeira-Ibáñez et al. (2012)	Yes	Yes	Yes	Iron cylinders rockwool cover
Romero-García et al. (2013)	Yes	Yes	Yes	Elastic beams of LDPF with cavities
Lagarrigue et al. (2013)	Yes	Yes	No	Bamboo rods
Morandi et al.(2016)	Yes	No	No	PVC
Bravo et al.(2019)	Yes	No	No	Aluminium
Iannace et al.(2021)	Yes	No	No	Wood
D'Orazio et at.(2023)	Yes	No	No	Maritime pine timber logs

Noise Barrier International Standards

The design and implementation of noise barriers are governed by international standards that ensure their effectiveness and safety. These standards specify the criteria for materials, construction, and performance, providing guidelines for achieving optimal noise reduction. Understanding and adhering to these standards is crucial for developing noise barriers that meet the required specifications and deliver the desired acoustic performance. However, not conventional barriers like the ones made by Sonic Crystals sometimes require other evaluation methods.

This thesis reviews the relevant international standards and explores how advanced optimization techniques can be employed to design noise barriers that not only comply with these standards but also require other evaluation techniques to test their performance.

In the realm of acoustic barrier design and implementation, international standards play a pivotal role in ensuring consistency and efficacy across various applications. Furthermore, the European Test Standards for Noise Barriers have undergone revisions to address the need for acoustically effective, durable, and low-maintenance systems. These revisions include defining higher categories for acoustic performance, mandating outdoor noise testing under direct sound field conditions, and the potential use of in situ acoustic testing for barrier maintenance and asset management. In contrast to conventional noise barriers, metamaterials, particularly those constructed from sonic crystals, present a novel approach to sound attenuation. Metamaterials are engineered to possess properties not found in naturally occurring materials, and in the context of acoustics, they can exhibit extraordinary sound insulation characteristics due to their unique structural design.

The evaluation of these SCNB requires new methodologies that account for their anisotropic and frequency-dependent behavior. Traditional standards may not fully capture the complex interactions within metamaterials, such as different incident performance and the anisotropic inertia that contribute to their insulation properties. Therefore, while international standards provide a foundation for assessing acoustic barriers, the advent of metamaterials made from sonic crystals calls for the development of new evaluative frameworks that can accurately characterize their performance [37].

1. **EN 1793-2 [38]:** This standard specifies the laboratory method for measuring the airborne sound insulation performance of road traffic noise reducing devices in reverberant conditions. It covers the assessment of the intrinsic performance of barriers that can reasonably be assembled inside the testing facility described in EN ISO 10140-2 and EN ISO 10140-4. The method requires two adjacent reverberation rooms, the "source room" and the "receiving room".

2. **EN 1793-3 [39]:** The European Standard EN 1793-3 provides a normalized traffic noise spectrum for evaluating and assessing the acoustic performance of devices designed to reduce traffic noise near roads.

3. **EN 1793-6[40]:** This part of the standard is about the test method for determining the acoustic performance. It focuses on the intrinsic characteristics and in situ values of airborne sound insulation under direct sound field conditions. The latest versions, published in 2023, provide guidelines for measuring the sound transmission properties of noise barriers. Unlike the subtraction technique used in reflection

measurements, transmission measurements do not require isolating parts of the signal. Instead, they directly compare the signal recorded with a noise barrier to the signal recorded without a barrier.

In summary, while both standards deal with the acoustic performance of road traffic noise reducing devices, EN 1793-2 focuses on airborne sound insulation in reverberant conditions, and EN 1793-6 deals with airborne sound insulation under direct sound field conditions. They use different testing methods and environments to measure the performance of these devices.

3 Strategies of Control; Metaheuristics Optimization, Modelling, and Methods

Metaheuristics are high-level strategies that coordinate local heuristics to find quality solutions to complex optimization problems. Both evolutionary algorithms and Deep Reinforcement Learning algorithms can be considered metaheuristics.

3.1 Heuristic Evolutionary Algorithms

The common family of evMOGA (Evolutionary Multi-Objective Genetic Algorithms), GA (Genetic Algorithms), and PSO (Particle Swarm Optimization) algorithms is called Evolutionary Computation. These algorithms are indeed considered heuristic optimization methods.

Here's a brief explanation of each that will be extended further in different chapters of this thesis:

- **Genetic Algorithms (GA)**: These are inspired by the process of natural selection and genetics. They use techniques such as mutation, crossover (recombination), and selection to find solutions to optimization problems [41].

- **Particle Swarm Optimization (PSO)**: This is a computational method that optimizes a problem by iteratively trying to improve a candidate solution with regard to a given measure of quality. It's inspired by the social behavior of bird flocking or fish schooling [42]. In chapter 5 a more extended explanation is made and the case study where it is applied.

- **Evolutionary Multi-Objective Genetic Algorithms (evMOGA [43, 44])**: The Epsilon Variable Multi-Objective Genetic Algorithm (ev-MOGA) is an advanced evolutionary optimization technique specifically developed to address multi-objective problems, which often require simultaneous optimization of conflicting objectives. One of the main challenges in solving such problems is finding a set of optimal solutions, known as the Pareto front, which represents trade-offs between competing objectives. Unlike single-objective optimization, where there is a clear best solution, multi-objective optimization typically results in a range of solutions where improving one objective might degrade another.

  To manage this complexity, ev-MOGA incorporates the concept of ϵ-dominance, which is a refinement of traditional dominance relations in evolutionary algorithms. ϵ-dominance allows the algorithm to maintain a smaller, more manageable set of Pareto-optimal solutions by introducing a threshold (ϵ) that determines how much better one solution must be in order to be considered dominant over another. This reduces the number of solutions to be stored and processed, while still maintaining a well-distributed spread of solutions across the objective space, ensuring diversity.

By adjusting ϵ dynamically during the optimization process, ev-MOGA strikes a balance between convergence, which is the ability of the algorithm to get closer to the true Pareto front, and diversity, which ensures that the algorithm explores different regions of the objective space. This balance is crucial for multi-objective problems, as it prevents premature convergence to suboptimal regions and promotes the exploration of potentially better solutions.

The result is a highly efficient algorithm that not only converges toward optimal solutions but also provides a diverse set of solutions, giving decision-makers or designers more flexibility in choosing the most appropriate trade-off according to their preferences. This makes ev-MOGA particularly suitable for complex real-world problems where multiple criteria need to be optimized simultaneously, such as engineering design, resource allocation, and logistics optimization.

Chapter 8 provides an in-depth explanation of this algorithm and its application to the optimization of a Multiresonant SC with acoustic switch transmission behaviour.

3.2 Deep Reinforcement Learning

Deep Reinforcement Learning (DRL) is a specialized branch of machine learning that is primarily concerned with sequential decision-making. This process is akin to a game, where an artificial agent, or 'player', interacts with its environment, or 'game board', over a series of steps. The agent's actions are driven by the goal of maximizing a cumulative reward, which is a measure of its success in the game [45].

The DRL framework can be described using the following components: an agent, a set of states S, a set of actions A, and a reward function R. At each time step t, the agent observes the current state s_t, chooses an action a_t from the set of available actions $A(s_t)$, receives a reward r_t, and transitions to a new state s_{t+1}. The agent's objective is to learn a policy π, which is a mapping from states to actions, that maximizes the expected cumulative reward [46].

One of the key aspects of DRL is the concept of exploration and exploitation. The agent needs to balance its time between exploring the environment to find rewarding states and exploiting its current knowledge to maximize the reward. This is often referred to as the exploration-exploitation trade-off.

Another important aspect of DRL is the concept of value functions, which are predictions of future rewards. They are used to quantify how good it is for the agent to be in a certain state, or how good it is to perform a certain action in a state. The agent uses these value functions to make decisions about what actions to take.

The agent learns from its interactions with the environment through a process of trial-and-error. It updates its policy based on the rewards it receives and the changes in the values of states and actions. Over time, the agent improves its policy, and hence its performance in the task [47].

3.3 Numerical Methods

Numerical methods are indispensable tools in the field of acoustics, allowing for the simulation and analysis of complex acoustic phenomena. These methods enable researchers to predict how sound waves interact with different structures and materials, facilitating the design and optimization of acoustic devices. The scientific community has recognized the significance of accurately predicting the acoustic performance of novel Noise Reduction Devices (NRDs) even before physical prototypes are created. To address this, researchers have developed and validated various numerical methods for evaluating the acoustic behavior of these devices. These simulation techniques have not only advanced acoustic technology but have also facilitated the creation of new NRDs, such as sonic crystals. In the realm of design, optimization methodologies combined with numerical simulations serve as powerful tools. By leveraging these methods, engineers can enhance the acoustic performance of sonic crystal noise barriers and introduce novel functionalities. Achieving this optimization requires an efficient simulation approach with minimal memory usage, especially when dealing with complex iterative processes and accurate predictions for different design proposals.

Finite-Difference Time-Domain (FDTD)

The Finite-Difference Time-Domain (FDTD) method is a powerful computational technique used to solve wave equations in acoustics. It involves discretizing the time and space domains to simulate the propagation of sound waves through different media. FDTD is particularly useful for modeling the interaction of sound with complex structures, making it an essential tool for this research. This thesis employs FDTD simulations to analyze and optimize the transmission properties of periodic acoustic structures.

In this section, the steps followed for the implementation of the FDTD simulation method [48]. are described.

Basics

The equations for momentum conservation and continuity provide the basis for an acoustic FDTD model without any sound sources. These models may be expressed as follows in a homogeneous medium with no losses:

$$\frac{\partial p}{\partial t} + k\vec{\nabla} \cdot \vec{u} = 0, \tag{3.1}$$

$$\vec{\nabla} p + \rho_0 \frac{\partial \vec{u}}{\partial t} = 0, \tag{3.2}$$

where $\vec{u} = (u_x, u_y, u_z)$ is the vector denoting the particle velocity field, p represents the pressure field, ρ_0 stands for the mass density of the medium and $B = \rho_0 c^2$ is the Bulk modulus. The central finite difference technique is used to approximate the spatial and temporal derivatives of pressure and particle velocity.

For the sake of readability and to avoid repeating very similar equations, the variable $\xi = (x, y, z)$ can be used to represent the three spatial coordinates. In this way, the governing equations of FDTD apply to both 2D and 3D cases in this thesis.

For instance, we can use this method to estimate the derivative of sound pressure with respect to the x-coordinate, which can be expressed by the following equation:

$$\left.\frac{\partial p}{\partial \xi}\right|_{\xi=\xi_0} \approx \frac{p\left(\xi_0 + \frac{\Delta\xi}{2}\right) - p\left(\xi_0 - \frac{\Delta\xi}{2}\right)}{\Delta\xi}. \tag{3.3}$$

In particular, the spatial interval denoted by $\Delta\xi$ represents the distance between closely-spaced points along the ξ-axis. In D dimensions, we must define $D + 1$ grids: one for pressure and D for the different components of particle velocity. To minimize the influence of higher-order terms in equations 3.4 - 3.7, these grids are 'staggered'. For instance, the mesh for the ξ component of particle velocity is shifted by $\Delta\xi/2$ relative to the pressure mesh. The same principle applies to the time intervals; the particle velocity meshes are shifted by $\Delta t/2$ in time compared to the pressure mesh. By adopting this approach, we can derive a set of update equations that allow us to determine the values of pressure and particle velocity after iterating for a specified number of steps. These equations are the following:

$$\begin{aligned} p_{i,j,k}^{n+1/2} = p_{i,j,k}^{n-1/2} - B\Delta t \Bigg(& \frac{ux_{i+1/2,j,k}^{n} - ux_{i-1/2,j,k}^{n}}{\Delta x} \\ & + \frac{uy_{i,j+1/2,k}^{n} - uy_{i,j-1/2,k}^{n}}{\Delta y} + \ldots + \frac{uz_{i,j,k+1/2}^{n} - uz_{i,j,k-1/2}^{n}}{\Delta z} \Bigg) \end{aligned} \tag{3.4}$$

$$ux_{i+1/2,j,k}^{n+1} = ux_{i+1/2,j,k}^{n} - \frac{\Delta t}{\rho}\left(\frac{p_{i+1,j,k}^{n+1/2} - p_{i,j,k}^{n+1/2}}{\Delta x}\right) \tag{3.5}$$

$$uy_{i,j+1/2,k}^{n+1} = uy_{i,j+1/2,k}^{n} - \frac{\Delta t}{\rho}\left(\frac{p_{i,j+1,k}^{n+1/2} - p_{i,j,k}^{n+1/2}}{\Delta y}\right). \tag{3.6}$$

$$uz_{i,j,k+1/2}^{n+1} = uz_{i,j,k+1/2}^{n} - \frac{\Delta t}{\rho}\left(\frac{p_{i,j,k+1}^{n+1/2} - p_{i,j,k}^{n+1/2}}{\Delta z}\right). \tag{3.7}$$

The superscripts denote the time index, and the subscripts denote the spatial indices as follows:

$$p_{i,j,k}^{n+1/2} = p(i\Delta x, j\Delta y, k\Delta z, (n+1/2)\Delta t) \tag{3.8}$$

$$ux_{i+1/2,j,k}^{n} = u_x((i+1/2)\Delta x, j\Delta y, k\Delta z, n\Delta t) \tag{3.9}$$

$$uy_{i,j+1/2,k}^{n} = u_y(i\Delta x, (j+1/2)\Delta y, k\Delta z, n\Delta t). \tag{3.10}$$

$$uz_{i,j,k+1/2}^{n} = u_z(i\Delta x, j\Delta y, (k+1/2)\Delta z, n\Delta t). \tag{3.11}$$

To have a better understanding of the update equations, Fig. 1 represents the FDTD scheme. With the aim of guaranteeing the numerical convergence, it is important that the time step is sufficiently small to accurately simulate wave propagation.

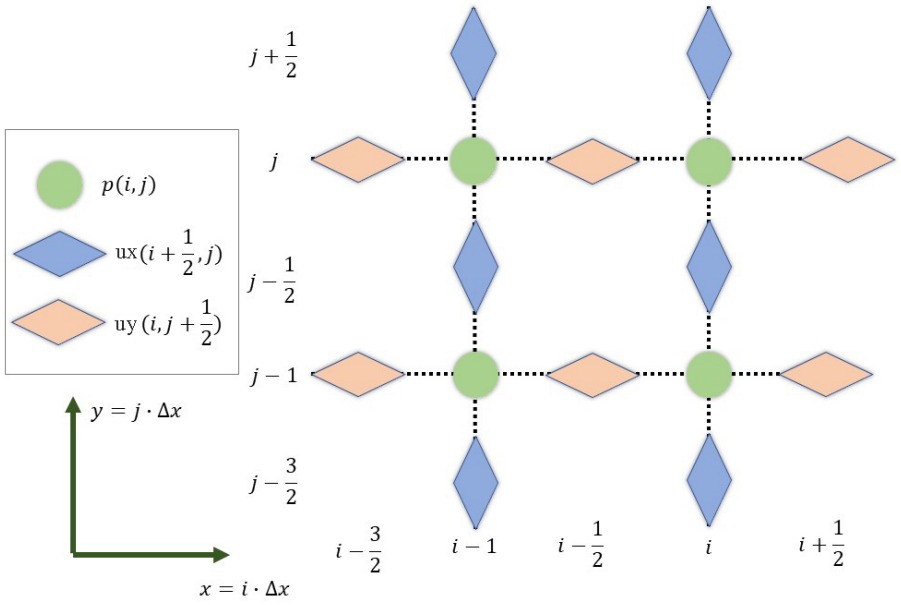

Figure 3.1: FDTD scheme of pressure and particle velocity fields in 2D

This relationship between the spatial steps and the time step is determined by the Courant-Friedrichs-Levy number s, which can be defined as follows in 3 dimensions:

$$s = c\Delta t\sqrt{\left(\frac{1}{\Delta x}\right)^2 + \left(\frac{1}{\Delta y}\right)^2 + \left(\frac{1}{\Delta z}\right)^2} \leq 1 \tag{3.12}$$

Another limitation of the FDTD method, which is shared with other numerical techniques, arises from the dependence of the maximum element size in discretization on the frequency. The standard criterion suggests using at least four elements per wavelength: in the related literature [49] it is shown that for a high level accuracy a minimum of 10 elements per wavelength is needed. Consequently, at high frequencies, solving the numerical problem becomes computationally intensive. In this thesis, we will employ a spatial step small enough to ensure accurate results up to 2 kHz.

Absorbing Boundary Conditions

In order to remove unwanted reflections from the boundaries of the computational domain, an absorbing boundary condition is used. The technique, known as "Perfectly Matched Layers" (PML) [50] is chosen. PML introduces a lossy medium near the boundaries, requiring modifications to equations 3.1 and 3.2 to incorporate attenuation factors for each dimension considered (denoted as γ_ξ in D dimensions). This adjustment is expressed as follows:

$$\frac{\partial p_\xi}{\partial t} + \gamma_\xi p_\xi + B\left(\frac{\partial u_\xi}{\partial \xi}\right) = 0 \tag{3.13}$$

$$\frac{\partial p}{\partial \xi} + \rho\left(\frac{\partial u_\xi}{\partial t} + \gamma_\xi u_\xi\right) = 0 \tag{3.14}$$

In equations 3.13 and 3.14 the sound pressure p is divided into D separate components p_ξ being $\xi = (x, y, z)$. These components do not have any physical significance and are defined merely for the purpose of optimizing the absorption performance. The attenuation factors are set to zero within the integration area but are heightened in regions near the boundaries.

Finite Element Method (FEM)

The Finite Element Method (FEM) is another crucial numerical technique used in acoustics. FEM divides a complex structure into smaller, manageable elements, allowing for the detailed analysis of how sound waves propagate and interact with the structure. This method is highly versatile and can be applied to a wide range of acoustic problems. In this thesis, FEM is utilized to complement FDTD simulations, providing a comprehensive approach to the optimization of Sonic crystal devices.

The Finite Element Method (FEM) is a computational approach used to solve partial differential equations in one, two, and three dimensions. The method involves breaking down the geometry into a finite number of small subdivisions, known as elements. These elements are interconnected at specific points called nodes, forming a mesh where the equation is solved. The global solution is obtained by solving for each individual cell and using interpolation to achieve a continuous solution across the entire domain. In the numerical models used in this study, the governing equation is the Helmholtz equation, which is given by:

$$\nabla \left(-\frac{1}{\rho_c} \nabla p_0 \right) - \frac{k_{eq}^2}{\rho_c} p_0 = 0 \tag{2.70}$$

Here, a harmonic pressure wave excitation is considered, with ($p = p_0 e^{i\omega t}$), the equivalent wavenumber is (k_{eq}) defined considering the effective parameters, and (ρ_c) is the complex dynamic density. All the rigid surfaces of the domain are generally modeled as sound-hard boundaries, considering the Neumann boundary conditions:

$$\vec{n} \left(-\frac{1}{\rho_c} \nabla p_0 \right) = 0 \tag{2.71}$$

where ($\vec{n}$) is the normal vector at the boundaries.

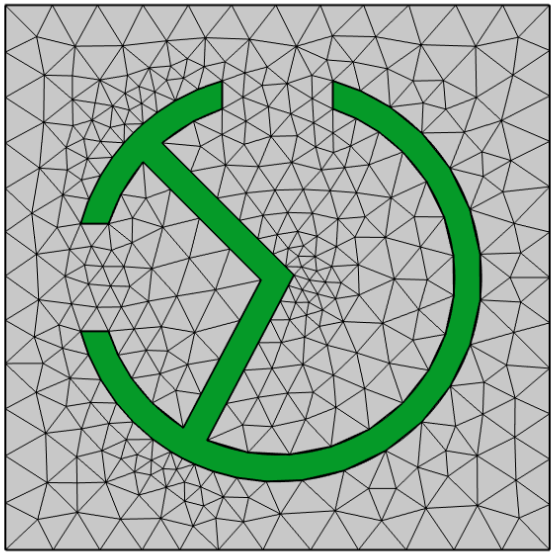

Figure 3.2: Adaptative FEM mesh of a 2D multiresonant scatterer unit cell.

The accuracy of the model depends on the size of the discretization elements, known as the mesh. For the acoustic systems modeled in this thesis, the maximum element size has been set to be at least eight times smaller than the smallest wavelength considered relative to the maximum frequency in the model. This ensures the correctness of results for high frequencies without assuming any overlooked approximations due to excessively large mesh size and without achieving the so-called convergence of the model. However, the smaller the mesh elements of the system, the higher the computational processing cost. Therefore, it is advisable to find a balance where convergence is achieved, and the system does not exhibit overly detailed geometry, which might be unnecessary for this study. Furthermore, the number of mesh elements has been increased near critical geometry features or particularly small elements, such as around holes or at the boundary between two materials. In practice, adaptive mesh refinement and practical adjustments have been set to enhance the mesh quality of a domain.

Viscothermal Losses

The main causes of dissipation of acoustic energy in a SCNB with HR are viscous forces and thermal conduction, which occur mainly at the viscous and thermal boundary layers. Temperature and velocity gradients between the bulk domain and the boundary surface are responsible for the losses. Based on these mechanisms, a distinction can be made between a thermal and a viscous boundary layer. While the heat gradient occurs when this boundary wall is isothermal, the velocity gradient can be explained by the fluid viscosity (μ) and the no slip condition at the wall. While the thermal boundary layer (δ_t) is a function of the fluid thermal conductivity (κ), the viscous boundary layer (δ_v) is dependent on the fluid viscosity. According to the following equations, the boundary layers are both frequency dependent [51]:

$$\delta_t = \sqrt{\frac{\kappa}{\rho_0 C_p \ \pi f}}, \tag{3.15}$$

and

$$\delta_v = \sqrt{\frac{\mu}{\rho_0 \ \pi f}} \ , \tag{3.16}$$

where C_p is the fluid heat capacity at constant temperature and the fluid density is ρ_0. Both characteristic lengths are related according to the not dimensional Prandtl number, $P_r = (\delta_v/\delta_t)^2$.

In the numerical models of this thesis, the fluid is air with $T = 20$°C and $p = 1$ atm, where thermal and viscous losses are almost equally important, having a $P_r = 0.7$, in contrast with water or other fluids where the role of thermal losses is smaller. Modelling viscothermal losses in acoustics can be computationally expensive as a large amount of detail is required to capture all physical effects. However, if the acoustic waves travel through slits with constant cross-section much smaller than the acoustic wavelength and larger than the thickness of the boundary layers, the viscothermal losses can be estimated by including them in the fluid in a homogenized approach for the narrow domain of the slit using the Low Reduced Frequency (LRF) models [52, 53].

According to the analyzed domain of the slits, the cases of this thesis are the necks of the HRs embedded in the scatterers and the governing equations in that zone to estimate viscothermal losses are, the complex wavenumbers by splitting it into the viscous and thermal parts, the following wavenumbers are obtained:

$$k_v{}^2 = -i2\pi f\frac{\rho_0}{\mu} \tag{3.17}$$

and

$$k_t{}^2 = -i2\pi f\frac{\rho_0 C_p}{\kappa}\ . \tag{3.18}$$

3.4 Parametric Design Process

Concept and parametric modeling

The development of a 3D-printed SCNB starts with the identification of function, size and required behaviour. Specific attention should be paid to ensuring modularity and adaptability to guarantee applications in different contexts. In addition, during such an initial phase, the limitation of the current available technologies must be considered for the realization of complex geometrical shapes[54]. Indeed, some of the chosen parameters also depend on the printing process. For example, the layer thickness, the material used, or a complex geometry (specifically in the z axis) can affect the 3D printing result. Consequently, the novel conceptual design needs to consider all these characteristics and achieve effective 3D modelling. Once the generic shape of the 3D printed SCNB is defined, the parametric model can be developed. This process provides the ability to change the shape of the model's geometry when specific dimension values are modified. Consequently, once the conceptual design of the model is ready, it is necessary to identify all the dimension values that need to be parameterized (e.g., thicknesses, lengths, heights, curvatures, and other parameters that can influence the noise barrier performances). The aim of this step is of fundamental importance since it allows an interactive application in synergy with FEM. The parameters of the 3D model can be changed until the target performances are reached.

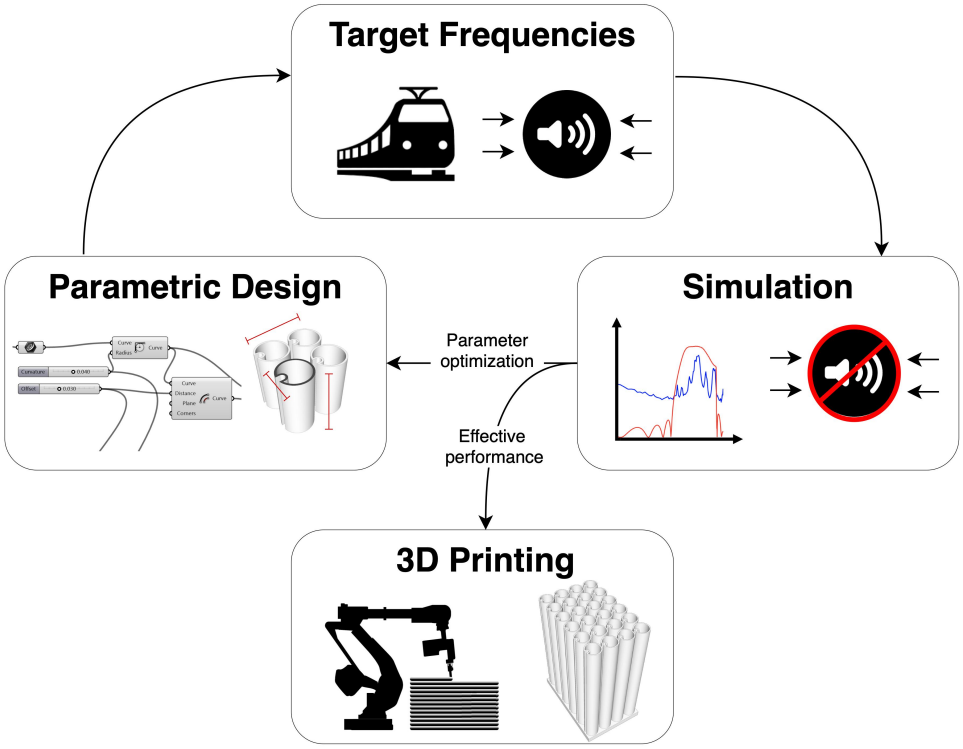

Figure 3.3: Workflow of the parametric modelling methodology with numerical simulations.

Since the proposed application in Chapter 6 concerns the noise barrier designed for railways, all the physical parameters should be modified in the parametric modelling to syntonise the SCNB performance in the annoyance frequency ranges. Moreover, the proposed barrier is characterized by numerous slender elements. Consequently, the 3D-printing process chosen for such type of barrier is the Fused Deposition Modelling (FDM), a technology capable of 3D printing with excellent precision that can exploit low environmental impact materials (as demonstrated by recent companies such as "The New Row"). Once the technology is defined, the noise barrier is modelled by using the visual scripting of Grasshopper to achieve a parametric model. Grasshopper is a visual programming language that runs within the computer-aided design software of Rhinoceros 3D (v.7.19.22165.13002) ([55]).

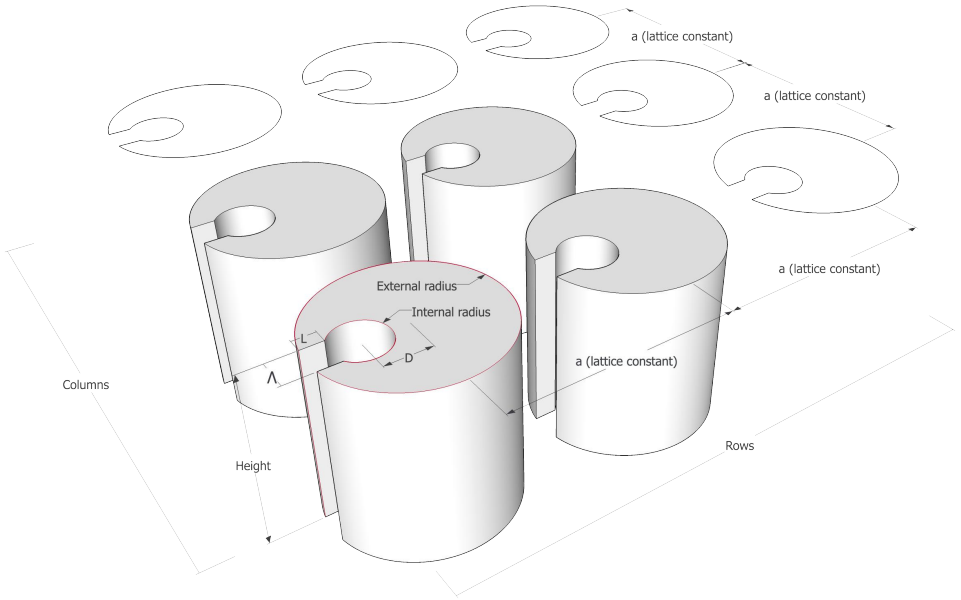

Figure 3.4: Parametrized 3D model of the SCNB.

In addition, Fig.3.4 shows the 3D model achieved with the related parameters and Fig. 3.5 shows the visual scripting of Grasshopper, where the parameterized dimensions are highlighted with green smoothed boxes. The script is able to combine different parameters to create a model of SC by utilizing components such as "rectangular array," "vector xyz," "circle," "extrusion," "region difference," and "cap hole."

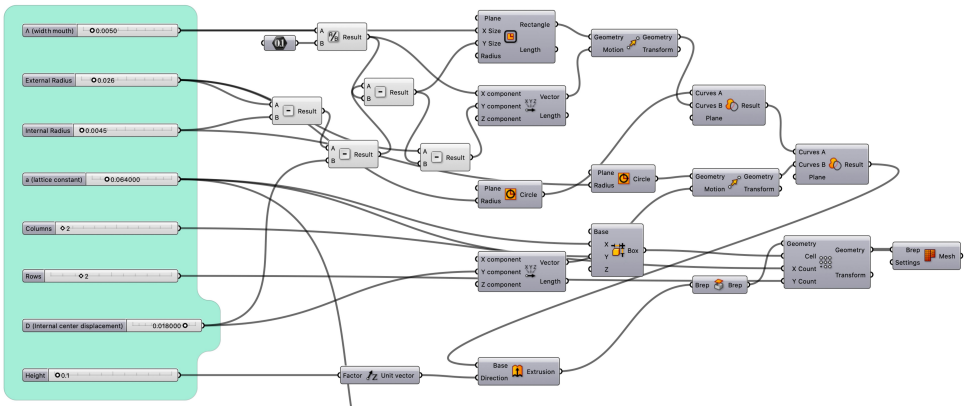

Figure 3.5: Parametrized 3D model of the SCNB.

In particular, in the parametric model, the following dimensions can be easily edited (in both the Helmholtz resonators parameters and their spatial

position, Fig. 3.5):

- Width of the mouth of the resonator (L).
- External radius corresponding with the shell of the resonator (er).
- Internal radius corresponding with the mouth of the resonator (ir).
- Length of the neck of the resonator (L) that is linked with the displacement (D) between the centre of the external and internal radius.
- Number of rows(r).
- Number of columns (c).
- Lattice constant (a) of the Sonic Crystal representing the separation between the periodic arrays of scatterers.
- Height of the resonator extrusion (h)

Fig. 3.6 showcases the diverse geometries achievable by manipulating the specified parameters within the Grasshopper script. More precisely, Fig. 3.6 presents in a graphical table of cells, the obtained modifications in the 3D models alongside their corresponding parameters. Each cell shows the 3D models obtained by modifying specific parameters. In particular, each row enlightens the variation of 3D model geometry obtained by modifying the parameters in bold.

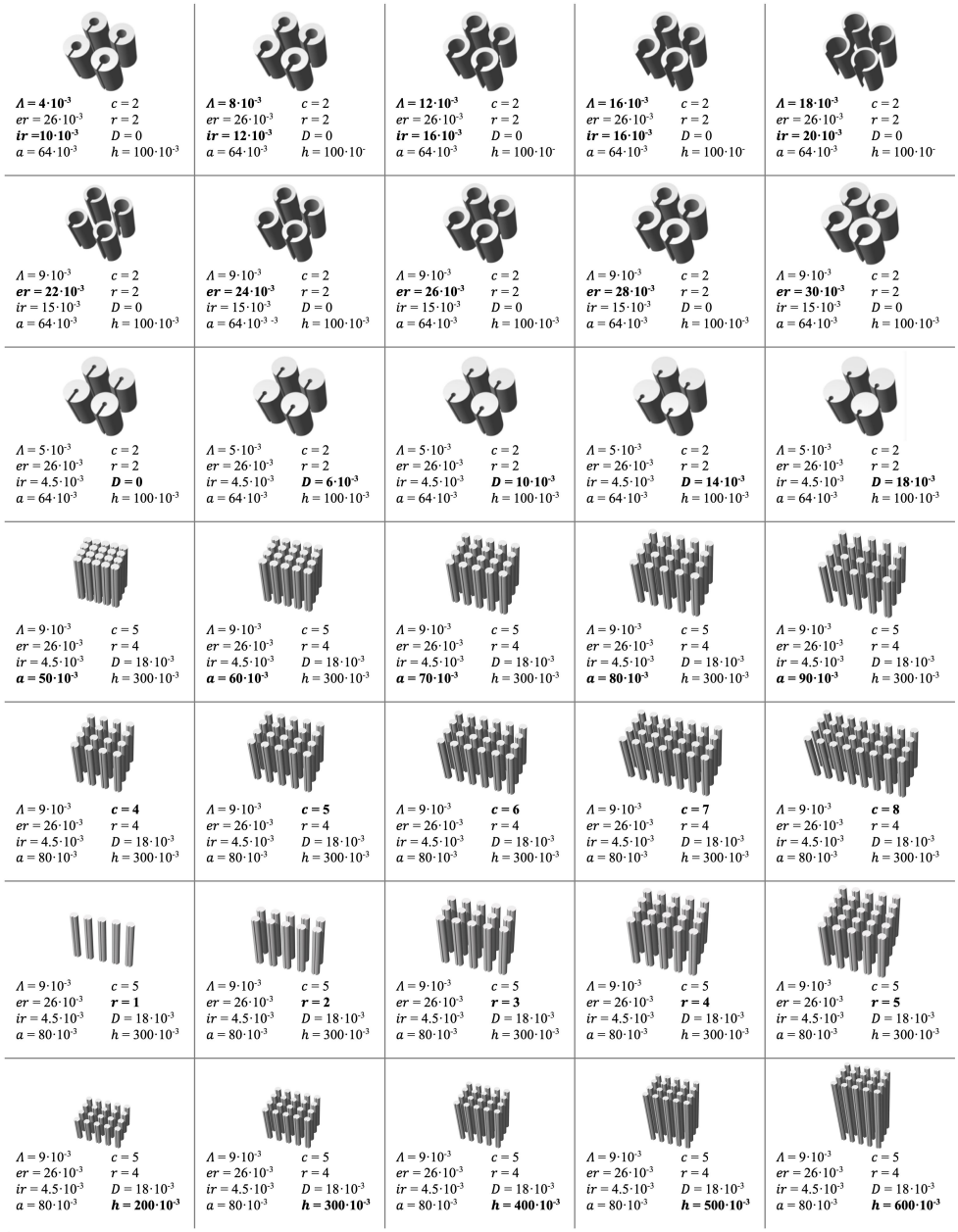

Figure 3.6: Parametrized 3D model of the SCNB.

3.5 Thesis Outline Methodology scheme

In the following table 3.1 all different approaches employed along the document are structured depending of the specific acoustic transmission case under analysis.

Given the absence of variation in the z-axis of the cylindrical scatterers with resonant cavities, and in light of the optimization processes, two-dimensional FDTD and FEM models have been employed consistently in this thesis.

Throughout this document, the resonant cavities in the scatterers may be referred to as Helmholtz Resonators (HR) or Continuous Cavity Resonator (CCR) as explained before. However, the term 'resonant cavity' is more encompassing, as some designs resulting from the optimization process do not strictly conform to the shape of an HR. For instance, in Chapter 5 and chapter 6 , it becomes exceedingly challenging to model the resonant scatterer, differentiating between the neck and the internal cavity, due to the C-shape of the optimized topology.

The abbreviations HR $\downarrow$ and HR $\uparrow$ in Table 3.1 refer to Helmholtz Resonators, which serve as transmission control mechanisms. Here, the upward arrow indicates that the resonance frequency is above the first Bragg-Band Gap (Bragg-BG) of Multiple Scattering (MS), while the downward arrow signifies that the resonance frequency is below the first Bragg-BG.

Table 3.1: Transmission cases in Sonic Crystals

Case Study	**Acoustic Phenomena**	**Optimization/Control Algorithm**	**Simulation technique**
Low frequencies. Traffic noise reduction	MS + ANC	DRL (DQN & DDPG)	FDTD
Low and medium frequencies. Traffic noise reduction	MS + HR $\downarrow$	PSO	FEM
High frequencies. Train brake noise reduction	MS + HR $\uparrow$	Parametric Modelling	FEM
Tunable frequencies. Multiresonant SCNB & Switch	MS + HR $\downarrow$ + HR $\uparrow$	evMOGA	FDTD & FEM

Part II

Active Noise Control in Sonic Crystal Noise Barriers

4 Improving the Insertion Loss of Sonic Crystal Active Noise Barrier by Reinforcement Learning and Finite Difference Time Domain Simulations

4.1 Introduction

The use of metamaterials in industrial applications has been promising during the last decade [56] In the field of noise barriers, Sonic Crystal Noise Barriers (SCNB) represent an innovative approach to mitigate the pervasive issue of traffic noise pollution. These barriers are designed to selectively target and attenuate sound waves at specific frequencies through the use of periodic structures, a concept rooted in the science of sonic crystals (SC) [16]. By carefully designing the topology of scatterers or adjusting the lattice constant between them, engineers can create SCNB suitable to reduce noise pollution effectively. The SCNB have the property of allowing the passage of wind and light [57]. This advantage makes them more aesthetically pleasing and environmentally friendly than traditional noise barriers, usually built using solid structures made with opaque materials such as concrete or wooden planks [21, 58]. However, the substantial costs associated with the installation and maintenance of SCNB have limited their widespread implementation [23].

Contrary to that, Active Noise Control (ANC) systems offer a potentially cost-effective approach to noise reduction. These systems operate by using strategically placed microphones to capture incoming noise and speakers to emit sound waves that are precisely out of phase with the noise, leading to cancellation [59]. ANC has been successfully applied in various domains, such as automotive [60] and industrial settings [61], where reduc-

ing noise is crucial. However, the effectiveness of ANC systems relies heavily on the accuracy of noise prediction models and the sophistication of the control algorithms used to generate the anti-phase sound waves [62]. The idea of improving the insulation of noise barriers employing ANC systems has been applied to traditional barriers since several decades [63]. Some of the studies are applied to real cases [64], other ones have developed their own experimental validations in anechoic chambers [65] and exploiting unidirectional sources [66].

Control algorithms play a pivotal role in ANC systems, and one approach that has gained prominence in recent years is Reinforcement Learning (RL) [46]. RL is a subfield of Machine Learning (ML) that focuses on developing algorithms capable of learning optimal actions through interaction with an environment and feedback in the form of rewards [47]. There is a wide scope of applications that have demonstrated its efficiency optimizing its processes such as Blockchain [67] or additive manufacturing processes [68]. Deep Q-learning and actor-critic methods, two prominent branches of RL, have been applied successfully to ANC systems [69], enabling them to adapt dynamically to changing noise conditions and improve noise reduction performance, especially in enclosed spaces or noise signals without simulations [70].

Before delving into the proposed RL-based solution for integrating ANC with SCNB, it is essential to recognize the important challenges and considerations that arise when combining these two technologies.
The SCNB challenges are the following:

- **Low-Frequency Performance:** SCNB, despite their effectiveness at certain frequencies, often struggle to attenuate low-frequency noise effectively. This limitation is particularly relevant in cases where the width of the barrier should not exceed a certain value [71].

- **Normal Incidence Insulation:** Many SCNB studies focus on noise reduction at normal incidence, neglecting the real-world scenario of random incidence noise sources. This limited normal incidence approach can differ from the noise reduction performance when the noise source is not aligned with the barrier [72].

- **Plane Wave Excitation:** SCNB designs frequently relies on the assumption of an incident plane wave as the primary noise source [73]. That means that the source is located far enough away, but that condition is usually not satisfied.

In addition, the ANC challenges are the following:

- **Fixed Primary Noise Sources:** Traditional ANC systems are primarily designed for scenarios where the primary noise source is fixed and known. In contrast, outdoor environments with varying noise sources pose unique challenges, as identifying and tracking these sources in real-time is complex.
- **Enclosed Spaces:** Most existing ANC applications target enclosed spaces [74], such as closed rooms, or ducts. The extension of ANC to outdoor environments with open boundaries and complex propagation conditions needs a different approach.

To overcome these challenges and bridge the gap between SCNB and ANC, this research proposes the development of an RL-based procedure for constructing SCNB that enhance their insulation performance by integrating an ANC system utilizing microphones and speakers. This approach leverages a Finite Difference Time Domain (FDTD) simulation environment handling low-frequency noise and dynamic outdoor noise propagation. The FDTD method, initially introduced by Yee in 1966 [75] for investigating the scattering of electromagnetic waves, has found applications in various acoustic domains. A parallel approach suitable for acoustic purposes has emerged with success in different applications. These applications encompass but are not limited to sound diffusers [48, 76], absorbing panels [77] and sonic crystal waveguides [17] and SCNB [78]. The FDTD modelling has proven beneficial in scenarios where spatial constraints and low-frequency bandwidth extension are critical considerations, and the FDTD simulation has also demonstrated its effectiveness in generating successful RL optimizations [79].

This approach offers several advantages:

- **Adaptation to Changing Conditions:** By continually learning and adjusting its control strategy, the RL-based ANC system can respond to varying noise sources, frequencies, and incidence angles, overcoming some of the limitations associated with traditional ANC.
- **Improved Low-Frequency Performance:** RL algorithms can learn sophisticated control strategies to tackle low-frequency noise, a known weakness of SCNB, by optimizing the placement and operation of ANC speakers.
- **Outdoor Noise Propagation Modelling:** The integration of a FDTD simulation environment allows for the more realistic modelling of outdoor noise propagation, to evaluate ANC effectiveness in open environments.

The chapter is organized as follows. Section 4.2 presents the employed methodology to create the FDTD simulations and the set-up of the RL problem, Section 4.3 specifies the case study of RL applied to a SCNB with ANC system. Section 4.4 presents the results of the training and deployment of the RL process and the acoustic analysis, and Section 4.5 encapsulates the conclusions and the future works.

4.2 Methodology

The tools and procedures to improve the SCNB with the ANC system are presented in this section. The implementation of the FDTD simulation method was previously explained in 3.3 that is why here there is only explained here the RL chosen agent procedure.

Reinforcement Learning with Deep Deterministic Policy Gradient (DDPG) Agent

The RL technique is an interdisciplinary area of ML dedicated to the domain of sequential decision-making. It revolves around artificial agents that, akin to their biological counterparts, refine their capabilities through interactions with the surrounding environment. Leveraging experiential knowledge (States), the artificial agents strive to accomplish defined objectives, presented in the form of cumulative rewards as it is illustrated in Fig. **2**. The essence of RL lies in the agent's capacity to assimilate suitable actions, progressively adapt, acquire new skills, and engage in trial-and-error experiences. Noteworthy components of RL include the agent's adeptness at interacting with the environment and information gathering, without necessitating an exhaustive understanding or control over the environment [47].

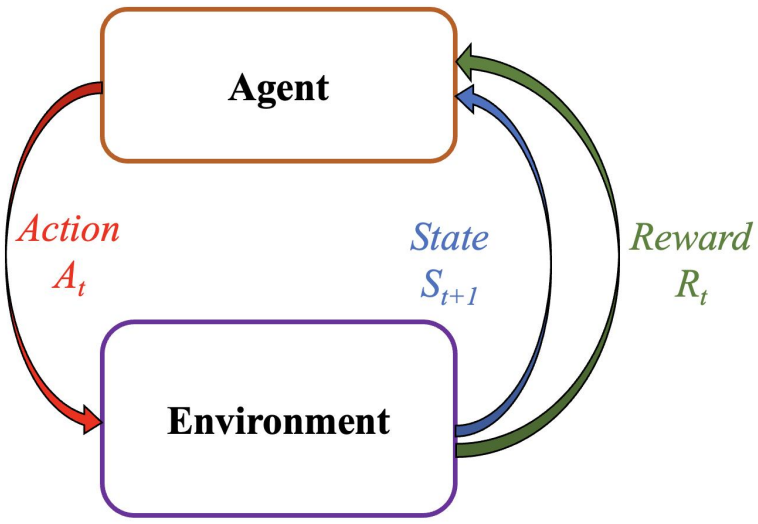

Figure 4.1: Main block diagram of the process of a generic RL system.

DDPG Training Algorithm

The RL structure is framed as a discrete-time stochastic control process. This process involves an agent engaging with its environment within the context of a discrete-time Markov Decision Process (MDP).
Specifically, a discrete-time MDP is described by the tuple (S, A, p, R) where S is the environment state set, A is the system action set, p is the state transition probability and R is the reward function. More precisely, the state transition probability (p) is the probability of transition from the current state $s_t \in S$ at time t to state $s_{t+1} \in S$ at time $t+1$ under action $a \in A$:

$$p : S \times A \times S \to [0, 1] \tag{4.1}$$

Moreover, the reward function R gives the reward after transition from s_t to s_{t+1} with action a:

$$R : S \times A \to [r_{\min}, r_{\max}] \tag{4.2}$$

The objective in RL is that the agent obtains an optimal policy $\pi(s)$ (conditioning the action to be chosen in state s) that maximizes the reward function. RL can directly calculate the optimal strategy without model knowledge and using a Q-function (Q-learning algorithm).
The Q-function, denoted as $Q(s, a)$, is a function that maps a state-action pair (s, a) to a value, representing the expected cumulative reward obtained by taking action a from state s and then following a certain policy. In this work, the selected agent is the Deep Deterministic Policy Gradient (DDPG) algorithm, a Q-learning actor-critic approach that consists of two parts: the actors that refer to a policy and the critic that estimates the Q-function. In the DDPG algorithm, both the actor and the Q-function (the critic) are approximated using neural networks. These kinds of agents are especially suitable for large continuous action spaces [45]. The used procedure is based on the steps described in the following.

1. Initialize the critic $Q(s, a)$ and target critic $Q_t(s, a)$ with the same random values of parameters (ϕ, ϕ_t).

2. Initialize the actor $\pi(s; \theta)$ and the target actor $\pi_t(s; \theta)$ with the same random parameters (θ, θ_t).

3. For each episode:

3.1 For the current state s of the episode, select an action according to the policy $\pi(s;\theta) + N$, where N is configured as exploration stochastic noise.

3.2 Execute action a and observe the reward r and the next state s'.

3.3 Store the experiences (s_i, a_i, r_i, s'_i) in the experience buffer along a mini-batch of size M experiences.

3.4 At each step of the training process, update the parameters of the critic ϕ by minimizing the loss L_{critic} across sampled experiences of the mini-batch:

$$L_{\text{critic}} = \frac{1}{2M} \sum_{i=1}^{M} (y_i - Q(s_i, a_i; \phi))^2 \tag{4.3}$$

where a_i is the bounded action derived from the policy unbounded output from the actor $\pi(s_i;\theta)$. If s_i is a terminal state (final of the episode), the value function target y_i is exactly the experience reward r_i. If it is not a terminal state, the value function target is the sum of r_i and the discounted future reward r' from the target critics, considering the noise added by the agent:

$$y_i = r_i + \gamma Q_(s'_i, \pi_t(s'_i;\theta_t);\phi_t) \tag{4.4}$$

where the discount factor γ represents how important the nearest rewards are compared to future rewards.

3.5 To calculate the cumulative reward, the agent initiates the computation by determining the subsequent action. This is achieved by forwarding the next observation s'_i obtained from the sampled experience to the target actor.

3.6 Depending on the time steps defined by the *"Policy frequency update"* hyperparameter, update the parameters of the actor θ using the policy gradient function to maximize the reward:

$$\nabla_\theta J_{\text{actor}} \approx \frac{1}{M} \sum_{i=1}^{M} (\nabla_A Q(s_i, a_i; \phi) \cdot \nabla_\theta \pi(s_i;\theta)) \tag{4.5}$$

where the first term of the product is the gradient of the critic's output with respect to the action computed by the actor, and the second term is the gradient of the actor's output with respect to the actor parameters.

3.7 Update the target critic Q_t parameters ϕ_t and the target actor parameters θ_t using the hyperparameter called the "smooth factor" τ:

$$\phi_t = \tau\phi + (1-\tau)\phi_t \tag{4.6}$$

$$\theta_t = \tau\theta + (1-\tau)\theta_t \tag{4.7}$$

The training algorithm is expressed in pseudocode in **Algorithm 1**.

Algorithm 1 DDPG Training process

Input: ϕ, θ, and M (Initial parameters)
$\phi_t \leftarrow \phi$ ▷ Initialize target critic parameters with the critic parameters
$M \leftarrow \emptyset$ ▷ Initialize the empty mini-batch M of buffer experiences

for each episode **do**
    for each environment step **do**
        $a_i \sim \pi(s;\theta) + N$ ▷ Sample action from the policy adding exploration noise
        $s'_i \sim p(s'_i|s_i, a_i)$ ▷ Sample state from the environment
        $M \leftarrow M \cup \{(s_i, a'_i, r_i, s'_i)\}$ ▷ Store the state in the mini-batch of buffer experiences
        $\phi \leftarrow \phi - L_{\text{critic}}$ ▷ Update the Q-function (critic) parameters
    end for
    for each policy update step **do**
        $\theta \leftarrow \theta - \nabla_\theta J_{\text{actor}}$ ▷ Update the policy parameters (actor)
        $\phi \leftarrow \tau\phi + (1-\tau)\phi_t$ ▷ Update target critic parameters
        $\theta_t \leftarrow \tau\theta + (1-\tau)\theta_t$ ▷ Update target actor parameters
    end for
end for
Output: ϕ, ϕ_t, θ (Optimized parameters)

4.3 Case Study: SCNB with ANC System

Finite Difference Time Domain Environment

The FDTD environment follows the process outlined in Fig. 4.1. By utilizing time-domain simulation techniques like FDTD, reinforcement learning (RL) can interact in real-time throughout the optimization process, enabling adjustments to be made at each time step. In contrast, standard frequency-domain simulation techniques only allow optimization after the process has finished and the stationary study returns the results.

Fig. 4.2 provides an overview of the simulation environment. The primary noise source is a moving car that emits a sinusoidal pure tone. The car travels from the lower to the upper boundary of the environment at a speed of 100 km/h. Each time the car passes through, it varies the frequency of the emitted tone, selecting a different random frequency ranging from 100 to 500 Hz. These frequencies represent the low range of the traffic noise spectrum, where the Sonic Crystal Noise Barrier (SCNB) is almost transparent. The noise produced by the passing vehicle is measured at a reference point. The recorded signal is then processed and broadcasted from a secondary source to enhance noise mitigation at the evaluation point, combining the properties of the SCNB and the Active Noise Control (ANC) system.

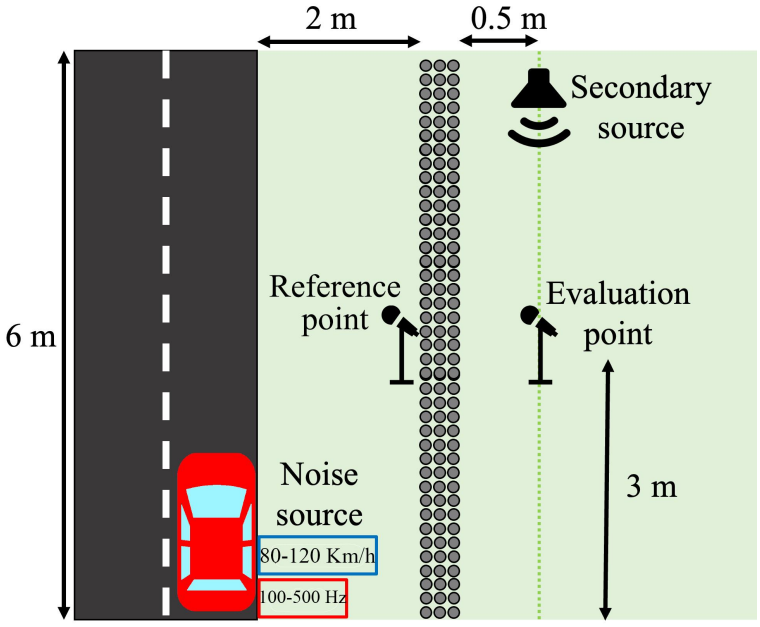

Figure 4.2: The FDTD Environment of the SCNB with the ANC system.

During the assessment phase, the cancellation signal from the loudspeaker and the car noise are evaluated to achieve noise cancellation following the principles of ANC. The FDTD simulation is conducted within a distinct function that the agent activates whenever it intends to interact with the environment. Consequently, this environment accepts inputs such as agent actions to be taken during the duration of time steps and provides outputs in the form of states or observations. Absorbing boundary conditions are implemented at the model's boundaries to mimic an open-field situation, following the form of Perfectly Matched Layers (PMLs) [50].

States

The primary objective of the RL architecture is to enhance the efficiency of the SCNB when coupled with the ANC system. Initially, the acoustic insulation provided solely by the barrier is considered as the baseline for reducing the acoustic pressure level. This serves as the initial observation in the process, i.e., the reset function of each episode. Following the execution of actions, a secondary pressure level is recorded, and subsequently, the Insertion Loss of the ANC system (IL_{ANC}) is computed according to the following formulation:

$$IL_{ANC} = 20 \log_{10} \left(\frac{\sum_{t}^{t_{\text{maxStep}}} p(t)_b}{\sum_{t}^{t_{\text{maxStep}}} p(t)_{ANC}} \right), \tag{4.8}$$

where the numerator comes from the reset function of each frequency when the ANC system is off, being $p(t)_b$ the pressure measured only having the SCNB without the ANC working. The denominator is the result of each step function when the ANC system is working. That implies that at each step of the episode, the state is measured as $p(t)_{ANC}$ at the evaluation point. The whole episode of a car passing is equally divided into 5 steps, with $t_{\text{maxStep}} \approx 30$ ms. IL_{ANC} is calculated at each step of the episode, having the summatory in the first step only one value, and at the end of the episode 5 values.

Actions

The actions space is continuous, and it has two different actions that can be explored in the RL system to modify the signal emitted by the secondary source. Both actions aim to generate an optimal signal capable of canceling the noise emanating from the noise source (car). But when the reference microphone (reference point) registers a pressure with the auditability threshold ($2 \cdot 10^{-5}$ Pa), the secondary source filters the sinusoidal

signal from the car and starts emitting from the secondary source. The first action ($Action_1$) determines the amplitude level of the signal emitted by the source, while the second action ($Action_2$) determines the phase of the signal. The range of $Action_1$ is from 0 to 0.5 Pa, and $Action_2$ has a range of variation between 0 and 2π.

When the phases of the signals are in opposition, the acoustic wave is canceled, creating a 'sweet point' in accordance with the main principle of ANC. The signal of the secondary source (S2) is described by the following equation:

$$S2 = -Action_1 \times \sin(2\pi f t + Action_2), \tag{4.9}$$

with f being the random frequency from the car settled in the reset function and measured at the reference point. As previously explained, an episode is defined when the car is passing through the whole environment, and 5 actions pairs are applied to every episode as there are 5 times steps and two actions in the action set to cancel the noise from the car.

Reward

The agent executes its behavior during each invocation of the step function, defined at intervals of $t_{\text{maxStep}} \approx 30\,\text{ms}$, and receives rewards based on how these actions influence the environment according to the states observed. The reward serves as feedback from the environment, indicating the success or failure of the agent's activities. The agent is tasked with adjusting certain parameters of the signal emitted from the secondary source to optimize noise cancellation at the evaluation point. Building upon the observations previously detailed, the Reward function (R) evaluates the Insertion Loss of the ANC system (IL_{ANC}) and assigns its value proportionally based on the extent to which the insulation is improved:

$$R = \begin{cases} IL_{ANC}, & \text{if } IL_{ANC} > 0 \\ 0, & \text{if } IL_{ANC} < 0 \end{cases} \tag{4.10}$$

4.4 Results

This section presents the results obtained from the ANC system in the SCNB. More specifically, first the training process of the SAC agent is presented, then the validation with the trained agent is proposed and finally the analysis of the acoustic performance of the system is discussed.

Training

During the process up to having a trained agent, the hyperparameters condition the process, and Table 4.1 shows all the values for the different parts of the RL system, the Critical and Actor networks.

Table 4.1: DDPG Hyperparameters

Name	**Value**
Agent Batch size	512
Agent buffer length (number of samples)	$1 \cdot 10^5$
Agent smooth factor (τ)	0.001
Agent Discount factor (γ)	0.99
Target Update frequency	1
Target smooth factor	0.001
Actor Learn rate	0.001
Actor Optimizer type	adam
Critic Optimizer type	adam
Critic Optimizer learn rate	0.01

The hyperparameters were tuned after observing different training processes. In the following Fig. 4.3 the training process is presented.

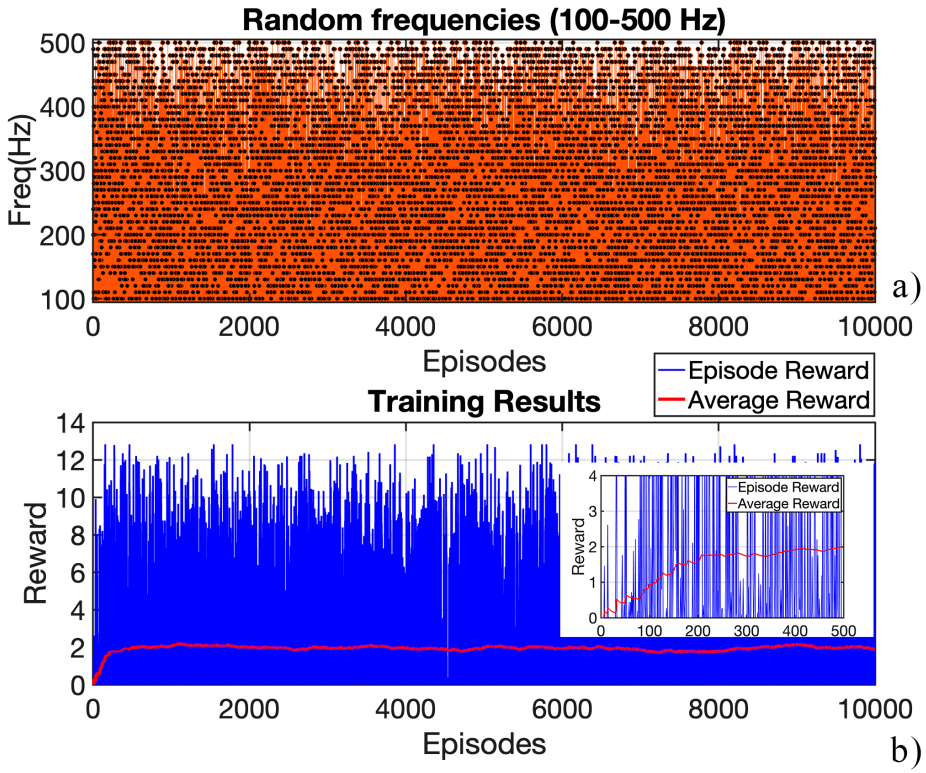

Figure 4.3: Training results of the DDPG agent. random frequencies of each episode a). Episode rewards (blue) and the cumulative average reward of all episodes(red) b).

The black dots shown in Fig. 4.3 a) represents the different random frequencies between 100 and 500 Hz during the training process. The total accumulated rewards throughout the training phase can be observed in Fig. 4.3 b). The cumulative reward for each episode is depicted in blue, while the overall average reward is highlighted in red. Even if the average reward is not very high compared to the single one obtained at some frequencies, it is still an improvement compared with the no ANC system case. Since the reward function was chosen to only be positive if the IL_{ANC} is better than the Insertion Loss produced with the SCNB and without ANC system (IL).

At some frequencies, the system improved the insulation up to 40 dB according to equation 22. That value represents the cumulative reward so it can be deduced that, taking into account that there are 5 steps, about 5 dB in average is obtained with ANC SCNB while the vehicle is passing by.

Deployment

Following the completion of training, the agent was considered for testing in the ANC procedure, aimed at assessing its capacity to respond to various frequencies, to be contrasted with the non-trained configuration. Additionally, the agent underwent testing to evaluate its performance against different car velocities, accounting for adjustments due to the Doppler effect. Differing from its training conditions, when only a velocity of 100 km/h was considered.

Despite being trained with random frequencies ranging from 100 to 500 Hz with the car (acting as a moving source) passing at 100 km/h, the agent demonstrated slightly diminished rewards when modifying the car velocity. Fig. 4.4 illustrates 21 distinct deployment episodes within the low-frequency range of interest (100-500 Hz) with a frequency step size of 20 Hz. Three velocities were examined: 100 km/h, which was utilized during the training phase, and 110 km/h and 120 km/h as additional velocities and new deployment scenarios. In deployment scenarios, the agent faces additional real-world conditions beyond its training environment, such as varying car velocities. This testing phase is crucial for evaluating the agent's adaptability and generalization capabilities.

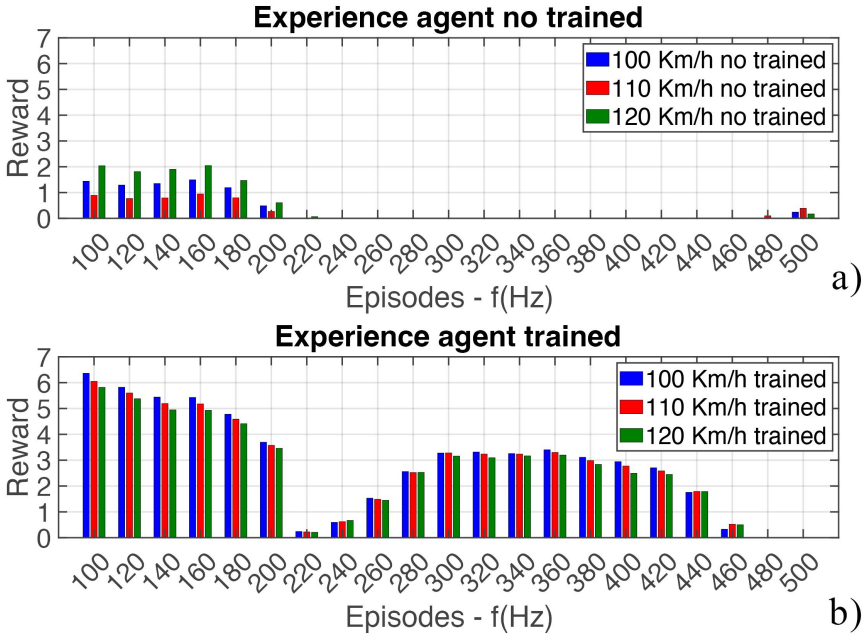

Figure 4.4: Comparison between DDPG agent deployment performance along 21 episodes (100-500 Hz range) with different car velocities before training the agent a) and after training it b).

It is noted that the non-trained agent (see Fig. 4.4 a) achieved approximately 1 or 2 dB of improvement in certain instances, particularly within the lower frequency range (100-220 Hz). This improvement can be attributed to the agent's ability to take four additional actions during each frequency episode as per the initial step, aimed at enhancing performance. However, despite these efforts, the improvement obtained remains modest compared to the SCNB without ANC. In contrast to that, the trained agent (see Fig. 4.4 b) obtains a remarkable improvement in the low frequencies and decreases with the frequency. Moreover, in the high frequency cases, the trained agent does not obtain an improvement compared to the SCNB without ANC. Hence, the lower the frequency is, the better performance of the cancellation principle of ANC works. The limit of the interest range of improvement is about 480 Hz, and even the agent has passed the training process, it was not possible to improve the SCNB with the ANC system.

The levels plotted are the average of the 5 steps of each episode, since each step was making a cumulative reward of all steps, bigger than the overall time calculation (about 40 dB) and the global vision of the insulation in dB is represented (around 4-5 dB in some cases).

The deployment scenarios highlight the challenges of real-world applications, where factors like varying car velocities can significantly impact the performance of the agent. Despite training in a controlled environment, the agent's effectiveness may vary when faced with these real-world complexities. Therefore, comprehensive testing under diverse conditions is essential to assess the agent's robustness and effectiveness in practical settings.

The insulation analysis with a global view depending on frequency spectrum is explained in the next section, together with the FDTD simulations results and the global acoustic performance.

Analysis

Considering that noise at higher frequencies can be mitigated with absorbent materials or other complementary solutions to the SCNB mechanisms, the IL analysis is plotted only showing until 2 kHz. The SCNB has 3 rows and 27 columns, and the main insulation mechanism is designed to mainly mitigate at 1 kHz, considering the peak of traffic noise spectrum [39]. In Fig. 4.5 the Insertion Loss (IL) of the barrier is plotted without the ANC considering that the noise incidence is not normal, neither diffuse. The car is moving at 100, 110 and 120 km/h, which produces different angles of incidence of the sound during the time it travels through the FDTD domain. Usually, SCNB are studied at normal incidence as enlightened in introduction, some studies have also considered the diffuse incidence [80],

but this approach looks for more realistic noise barrier case which is the moving source incidence. In blue, the insulation provided without the ANC is plotted until 2 kHz, to mainly observe where the SCNB produces bigger values due to its noise control phenomena [27].

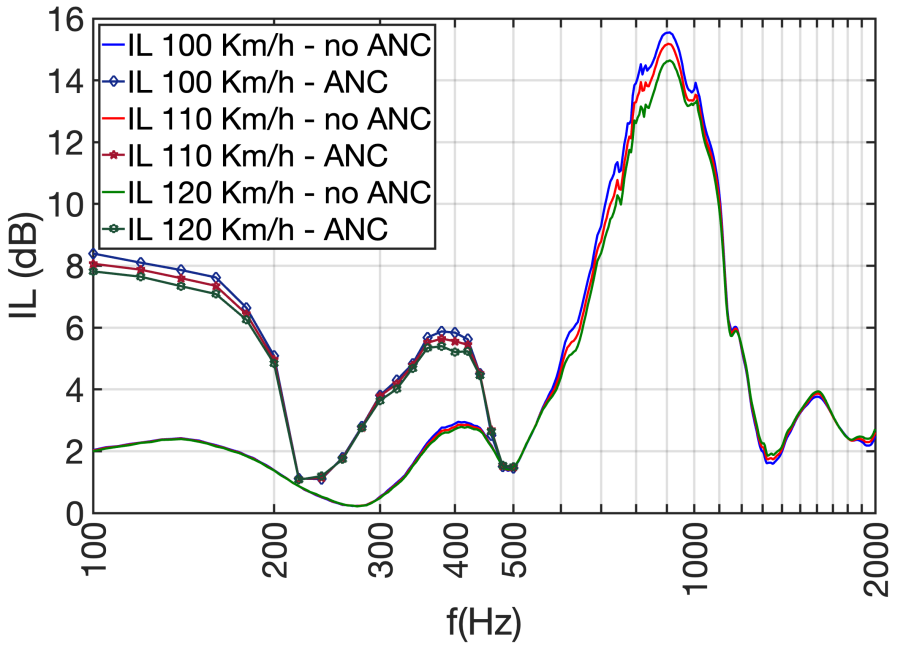

Figure 4.5: Insertion Loss of a SCNB of 3 rows with a moving source of 100, 110 and 120 Km/h incidence, with and without the ANC system working.

For the three deployment scenarios under consideration (100, 110, and 120 km/h), represented by blue diamonds, red stars, and green stars respectively, the rewards obtained for each frequency with the trained agent (as depicted in Fig. 4.4 b) are added to the original IL. In the low frequency range (100-500 Hz), the significant insulation improvement can be seen, and this is obtained without modifying the barrier. The IL shows in dB the difference between having the barrier or not and the noise reduction. At some frequencies, it has been seen that the ANC system is capable to produces bigger improvements (8 and 6 dB in the peaks), but the Fabry-Perot resonances [81] are still present in the IL spectrum.

Finally, an instantaneous representation of the FDTD environment is showed in Fig. 4.6, where the ANC system is switched off in Fig. 4.6 a) and a small modulation of the 200 Hz noise wave is observed close to the reference microphone due to the SCNB. Fig. 4.6 b) shows the ANC working

and producing interferences to mitigate the sound in the evaluation point. Considering that t = 0 ms is when the car is starting to move from the top at 100 Km/h, Fig. 4.6 represents the instant of t = 30 ms, which is the moment after the first step function is executed and the first state is observed from the FDTD environment. The Sound Pressure Level (SPL) maps represent in dB the acoustic pressure distribution in the whole environment at that specific instant. The PMLs are working perfectly preventing reflections as in the deep blue color the 0 dB is obtained at the boundaries.

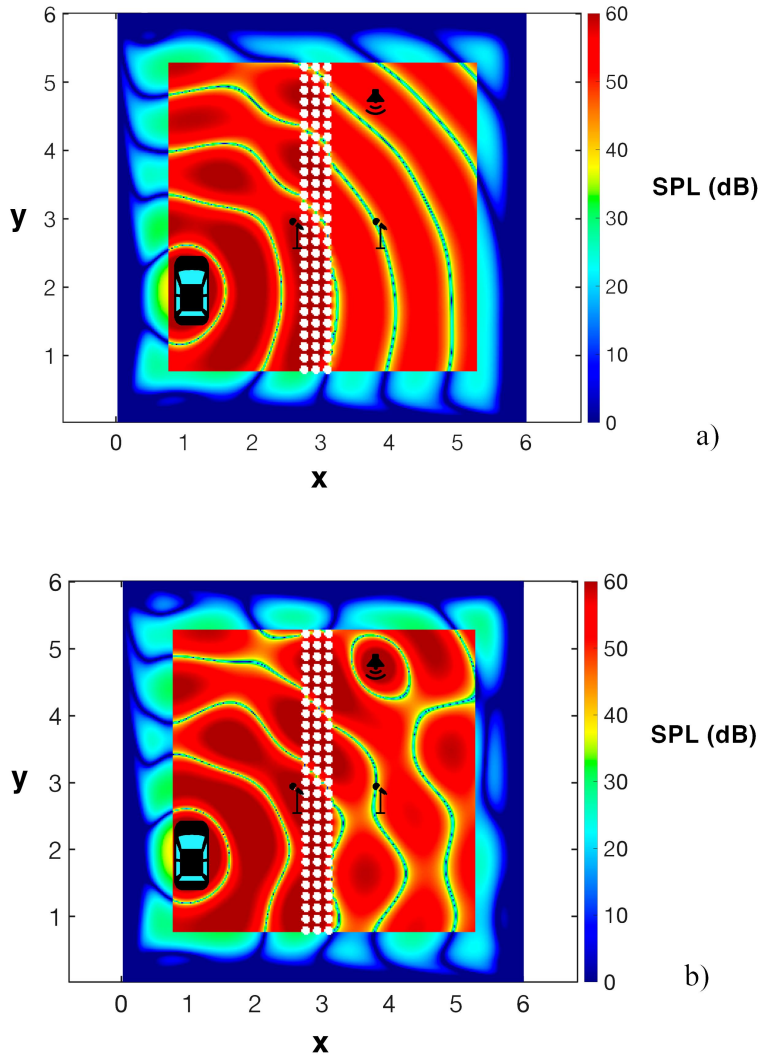

Figure 4.6: FDTD SPL maps at t = 30 ms with the car emitting noise at a frequency of 200 Hz. a) the ANC system switched off; b) the ANC system switched on.

4.5 Conclusion

This work has presented a complete framework to smartly approach the issue of low frequency insulation on SCNB. Without modifying the geometry of the barrier or increas- ing the width, the placement of an ANC system improves the insulation in the lower frequency range of traffic noise spectrum (100-500 Hz) [39]. The use of FDTD numerical simulations extendedly validated in other works previously mentioned, allows the fast calculation of RL steps, and the quick modification of the cancelling secondary source parameters. The case of road traffic noise produced by a mobile source is analyzed. This approach is more realistic than the assumption of normal or diffuse incidence. Since SCNB are designed to insulate specific target frequencies, the ability to address random noise frequencies with the RL system is one of the biggest milestones. Further analysis of doppler effects of the moving source and different locations of the secondary cancelling source will be forthcoming studies. In the future research lines, the search of very low latency systems will be performed to quickly modify the loudspeaker emission parameters and to properly mitigate the noise in an experimental validation. Also, the implementation of speakers in the last row of the scatterers of the SCNB will be consider, for the purpose to have a more compact system.

Part III

Resonant Sonic Crystal Noise Barriers

5 Particle Swarm Optimization of Resonant Sonic Crystals Noise Barriers

5.1 Introduction

In this chapter we overcome the previous drawbacks, by proposing a new technique to optimize the parameters of Sonic Crystal Noise Barrier (SCNB). More precisely, the SCNB is described by 2D simulation models and the best insulation levels of the barriers are obtained by applying a Particle Swarm Optimization (PSO) algorithm [42].

Note that the PSO algorithms have been applied to several acoustics' cases, such as acoustic radiation [82] , porous materials [83], ultrasonic transducers [84], acoustic filters [85], room acoustics [86], all of them having an enormous ranges for the search space, in the optimization process. The numerical technique used for modelling the system and assessing the performance of each possible solution is the Finite Elements (FE) simulations.

In particular, this chapter focuses on a key element of the SCNB: the optimization of the scatterer's topology and the periodicity of the metamaterial that depends on the lattice constant distance.

To assess the results obtained by the proposed approach, the presented PSO algorithm is compared with GA.

PSO and GA are both popular metaheuristic optimization algorithms used to solve complex optimization problems. It is important to note that the performance of PSO and GA can depend on the specific problem being solved [87, 88]. In the considered case, the following advantages of PSO over GA are deduced by the simulation analysis and study.

- **Less prone to getting stuck in local optima:** We verified that in the considered problem PSO is less likely to get stuck in local

optima than GA because it uses velocity and position to update the particles' position in the search space. This allows PSO to escape from local optima and continue exploring the search space. On the other hand, the search space of the presented problem has large 4-dimensional range of possible combinations. All these combinations can bring very different fitness values even modifying only one of the physical parameters to optimize.

- **Smaller computational effort:** In the performed experiments we verified that PSO converged to the optimal solution more quickly than GA. This is because PSO combines global and local search mechanisms which allow exploring the search space more efficiently than GA.

- **Robustness:** PSO resulted more robust than GA because it does not require a fitness function that is differentiable or continuous. PSO can handle noisy and discontinuous fitness functions as the noise barriers global insulation value presented in this study, making it suitable for a wide range of optimization problems.

The results show that the PSO algorithm provides a good solution that pursues the objective of satisfying the acoustic comfort without exceeding some imposed practical constraints. The chapter is organized as follows. Second section presents the employed methodology and third section specifies the case study of SCNB optimization module. Moreover, Section four presents the results and Section five discusses the comparison with GA and random values. Finally, Section VI summarizes the conclusions and the future works.

5.2 Methodology

The tools and procedures to optimize the SCNB are presented in this section. First, the specifications of the model that should be optimized is described, second the applied optimization algorithm is presented, third the GA and random search used to enlighten and compare the obtained benefits are explained.

Finite Elements 2D Model

In this subsection we describe the FE 2D model of the SCNB that needs to be optimized. The aim is to obtain a precise simulation model requiring low computational cost to apply the optimization process that calls for several iterations.

Moreover, an exact estimation of the acoustic performance of the various proposed designs is requested. In addition, since the SCNB are typically built throughout extremely long extensions of kilometers in the borders of highways or railroads, the model showed in Fig. 5.1 represents a semi-infinite width barrier. This barrier receives the sound coming from the left part of the model and the remaining acoustic pressure that pass through the noise mitigation device is evaluated at the right part of the model at the red points.

To eliminate unwanted reflections (free field condition), Perfectly Matched Layers (PMLs)[50] are positioned at the vertical contours (left and right), and the incident plane wave (IPW) travels from left to right. The horizontal contours are periodic conditions that repeat the model in the Y axis, the evaluation points are placed one meter away from the edge of the last scatter. These values are averaged to cover a more general behaviour in the performance zone of the barrier.

The four physical parameters that define the topology of the scatterers and the periodicity of the SCNB are represented in Fig. 5.1:

- The lattice constant x_1 that is the periodicity of the SCNB, i.e., the separation between rows and columns of the center of the scatterers.
- The external radius of the cylindrical scatter x_2;
- The internal radius of the cylindrical scatter x_3;
- The width of the mouth of the Helmholtz resonator embedded in the scatter x_4.

We remark that by using the described model, the computational cost of the result of each simulation is varying depending on the topology and how the elements of the domain are adapting to the shape with the FE mesh.

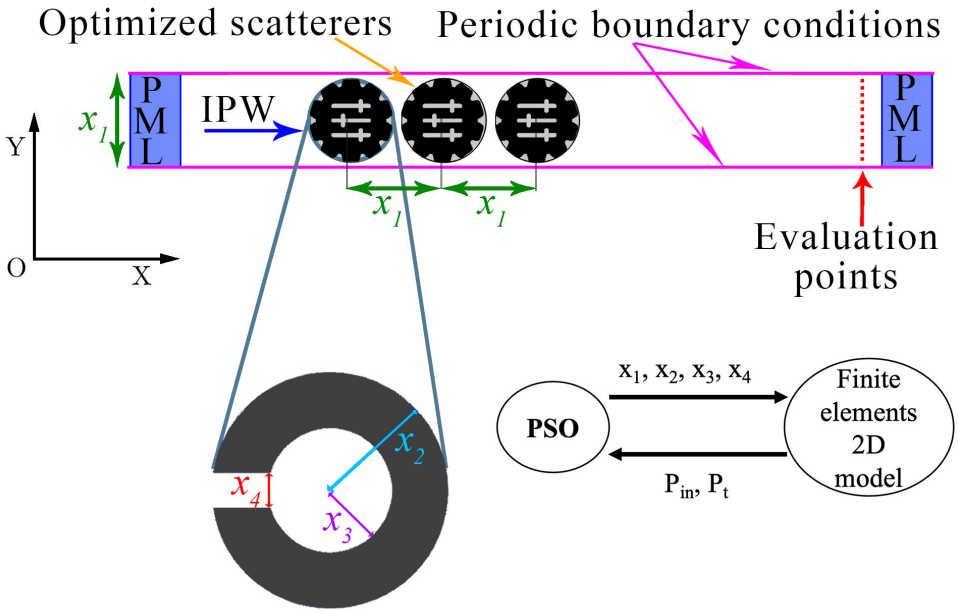

Figure 5.1: 2D Finite elements model of periodic sonic crystal noise barrier. 3 rows of scatters to be optimized and the distance between them too with the PSO algorithm.

The Particle Swarm Optimization

The PSO is part of the evolutionary algorithm's family and is based on the animal behaviour. The original version of the algorithm tried to simulate the social behaviour of the animals to model their fly, changing of position and researching the global best position. In the PSO algorithm several components, called particles, are placed in the search space of the problem, and each of them evaluates the fitness (or objective) function at its current location. Each particle determines its movement through the search space by combining some aspects of the history of its own current and best positions with those of the nearest members of the swarm. The next iteration takes place after all particles have been moved. The swarm as a whole, like flock of birds foraging for food, moves close to an optimum of the fitness function [89]. Each particle of the swarm is composed of three D-dimensional vectors, where D is the dimension of the search space: the

current position X_j, the previous best position $Xbest_j$, and the velocity v_j. The current position X_j, considered as a set of coordinates describing a point in the space, is evaluated as a possible problem solution. If such position results to be better than the previous ones, then its coordinates are stored in the vector n $Xbest_j$. The value of the resulted best function is stored in a variable called previous best $pbest_j$, for comparison on the later iterations. The objective of the algorithm is to find better positions and update n $Xbest_j$ and $pbest_j$ vectors. Moreover, the algorithm iteratively updates the velocity vector v_j and calculates new points by adding the v_j coordinates to X_j. A version of the PSO algorithm can be explained according to the following algorithm steps [90].

PSO Algorithm

- Initialize a population array of N particles with random positions and velocities on D dimensions in the search space.
- At the iteration k execute the loop:
  - For each particle of the N population, evaluate the desired optimization fitness function for particle j in D variables by simulating the described FE model.
  - Compare the particle's fitness evaluation with its $pbest_j$. If the current value is better than $pbest_j$, then set $pbest_j$ equal to the current value, and $Xbest_j$equal to the current location $X_j \in \mathbb{R}+^D$ where $\mathbb{R}+$ is the set of real positive numbers in the $D-$dimensional space.
  - Identify the particle in the group of N particles with the best success so far and assign its index to the vector $Xgbest$ and variable $gbest_j$.
  - Change the velocity and position of the particle according to the following equations, respectively:

$$\begin{aligned} v_j(k+1) = w \cdot v_j(k) + c_1 \cdot r_1^{(k)} \cdot [p\text{best}_j(k) - X_j(k)] + \\ \ldots + c_2 \cdot r_2^{(k)} \cdot [g\text{best}_j(k) - X_j(k)] \end{aligned} \tag{5.1}$$

$$X_j(k+1) = X_j(k) + v_j(k+1) \tag{5.2}$$

  - If a stop criterion is met, then exit the loop.

In the velocity equation 5.1 the w factor is called inertia weight. It was introduced in [91] to reduce the effect of the maximum velocity, affecting the impact of $v(k)$ on $v(k+1)$. In addition, r_1 and r_2 are random numbers in the range $[0, 1]$, c_1 and c_2 are positive constants, called acceleration coefficients, which are responsible for appropriately weighting both the cognitive and social components. Indeed, the velocity of particles drives the optimization process through the cognitive component, based on particle's historical information, and the social component with information about the best solution found by the swarm.

Some parameters must be appropriately chosen, depending on the problem to be solved, to guarantee the algorithm convergence. The number of particles is typically chosen between 10 and 50. But depending on the search space dimension, it can be necessary to increase the number of particles to have a wider exploration. The maximum velocity of each parameter to optimize is given by the following equation:

$$v_{\max} = h * \frac{(X_{\max} - X_{\min})}{2} \tag{5.3}$$

where $0 \leq h \leq 1$ is the clamping factor, and $X_{\max} = [x_{1\max}, x_{2\max}, x_{3\max}, x_{4\max}]$ and $X_{\min} = [x_{1\min}, x_{2\min}, x_{3\min}, x_{4\min}]$ are the vectors including the maximum and minimum values that each element of X can be settled in the optimization process, respectively.

Note that maximum velocity of each particle is limited by the range $[-v_{\max}, +v_{\max}]$.

Generally, the inertia weight w at iteration k is given by the following equation:

$$w(k) = w_{\min} + \frac{(itr_{\max} - k) \cdot (w_{\max} - w_{\min})}{(itr_{\max} - 1)} \tag{5.4}$$

where $itr_{\max}$ is the maximum number of iterations of the algorithm and k is the current iteration. Typically, $itr_{\max} = 10$ and $w(k)$ decrease in the interval $[0.9, 0.4]$, by guaranteeing the equilibrium between exploration and exploitation.

The following relationship between c_1, c_2 and w guarantees the PSO algorithm convergence [91]:

$$w > \frac{1}{2}(c_1 + c_2) - 1 \tag{5.5}$$

In particular, choosing $w = 0.7298$, $c_1 = c_2 = 1.49618$ provides good convergent behaviour [92].

Genetic Algorithms (GA) and Random Tests

With the goal of having a more global vision of the case study, two more cases are compared with the PSO in the SCNB model, GA and Random tests.

As it has been said in the introduction, GA have been already used to optimize SCNB without Helmholtz Resonators(HRs), so in this case the model and the function to optimize would be the same as the PSO case to compare the optimization process and results. On the other hand, depending on the number of simulations needed to find the convergence in the PSO best Fitness value, this number defines the maximum number of models to evaluate. So, with equal probability, all possible values between $X_{\max} = [x_{1\max}, x_{2\max}, x_{3\max}, x_{4\max}]$ and $X_{\min} = [x_{1\min}, x_{2\min}, x_{3\min}, x_{4\min}]$ will be explored by testing randomly SCNB simulation models. In a "box and whiskers" plot, the results of random simulations and its DL_{SI} values will be represented. More specifically, the boxplot represents with the red line the median of all values, and the blue limits of the box are the upper and lower quartiles, respectively. The red crosses are the outliners of the found minimum and maximum values.

By doing this analysis it can be seen how good or bad would be the results of a person trying find the best value found, only with random tests and not following and optimization criteria.

5.3 Case Study: The SCNB Optimization module applying PSO Algorithm

In this section we present the SCNB optimization module. In detail we consider a specified application of the optimization that is applied to determine the optimal topology of the scatterers and periodicity of the 2D model showed in Fig. 5.1. The aim is guaranteeing the biggest attenuation possible in the frequency range [100-5000 Hz] included in the European Standards[39, 40], one of the main objectives of the noise barriers. The problem is solved by using the PSO that turns out to be an effective tool to optimize this type of problems with such a difficult search space. Indeed, the PSO algorithm has the properties of fast execution, not complex implementation, parallel behaviour, and no need to have the problem optimization to be differentiable [93].

Fitness function

The fitness function *gbest* to optimize is a single value to express how good is the barrier insulating noise. The European Standards EN 1793-3 [39] and EN 1793-6 [40] define the calculation proceeding of the single-number rating of the airborne sound insulation for road traffic (sound insulation index DL_{SI}) as follows:

$$DL_{SI} = -10 \cdot \log \left(\frac{\sum_{i=m}^{18} 10^{0.1 \cdot L_i} \cdot 10^{-0.1 \cdot SI_i}}{\sum_{i=m}^{18} 10^{0.1 \cdot L_i}} \right) \text{ dBA} \tag{5.6}$$

where m is the number of the third octave band frequency spectrum and L_i is the dB-value of the *i-th* third-octave band of the traffic noise spectrum, represented in Table 5.1, according to EN 1793-3 [39] .

SI_i is the value in dB of the *i-th* third-octave band of the sound insulation spectrum which is calculated in the FEM Model at the evaluation points:

$$SI = 20 \cdot \log_{10} \left| \frac{P_{\text{in}}}{P_t} \right| \text{ dB} \tag{5.7}$$

where P_{in} is the value of the incident effective pressure without the barrier and P_t is the value of the effective pressure transmitted with the barrier placed. Both pressures are obtained at the same evaluation points showed in Fig. 5.1.

Table 5.1: Normalized Traffic Noise Spectrum

m	Central frequency [Hz]	L_i [dB]
1	100	-20
2	125	-20
3	160	-18
4	200	-16
5	250	-15
6	315	-14
7	400	-13
8	500	-12
9	630	-11
10	800	-9
11	1000	-8
12	1250	-9
13	1600	-10
14	2000	-11
15	2500	-13
16	3150	-15
17	4000	-16
18	5000	-18

Even though the standards only provide the central frequency for each third-octave band, in the FEM model, the average of the three frequencies within each third-octave band has been calculated to achieve a more accurate representation of the full frequency spectrum.

The upper and lower bounds of the 4-dimensional search space ($D = 4$) to optimize are limited to create as maximum, 1 m length of noise barrier and only 3-rows of scatterers, which means according to the external radius and the lattice constant that $2 * (x_1 + x_2) = 1$. Hence, we impose $X^T_{\max} = [0.3900, 0.1755, 0.1667, 0.3301]$ and $X^T_{\min} = [0.1000, 0.0300, 0.0015, 0.0001]$.

In doing this, the models are more realistic approaches to already existing conventional noise barriers length.

Process of the Optimization

The PSO algorithm is described by the following pseudocode that implements the steps described in Section 2.

Algorithm 2 Particle Swarm Optimization Algorithm for SCNB

Initialize particles with $k = 0$
Set the configuration coefficients N, $itr_{\max}$, c_1, c_2, $w_{\min}$, $w_{\max}$
Set search space ($D = 4$), upper and lower bounds of X

for $j = 1$ to N **do**
    Set random values of $X_j = [x_{1j}, x_{2j}, x_{3j}, x_{4j}]^T$
    $p_j = (X_j, (0, 0, 0, 0), (0, 0, 0, 0))$
end for
Evaluate Fitness values
$k = k + 1$ until $k = itr_{\max}$
for $j = 1$ to N **do**
    for $i = 1$ to 18 **do**
        Simulate the Finite Elements Model with X_j
        Obtain P_t and P_{in}
        Calculate SI_i
    end for
    Calculate DL_{SIj}
end for
Analysis
for $j = 1$ to N **do**
    if $DL_{SIj} > DL_{SIpbestj}$ **then**
        $Xbest_j = X_j$
    end if
end for
$DL_{SIgbest} = \max(DL_{SIgbest}, \max_{j=1:N}(DL_{SIpbest}))$
$Xgbest = select_{j=1:N}\{p_j$ such that $DL_{SIj} = DL_{SIgbest}$
Swarm updates
for $j = 1$ to N at k iteration **do**
    Calculate inertia $w(k)$ according to equation 5.4
    Calculate future velocity $v_j(k + 1)$ according to equation 5.1
    Calculate future position $X_j(k + 1)$ according to equation 5.2
    Set $p_j = (X_j(k + 1), Xbest_j, v_j(k + 1))$
end for
if $k < itr_{\max}$ **then**
    Go to **9: Evaluate Fitness values**
end if
End of the process
$X_{\text{optim}} = Xgbest$
Return X_{optim}

The optimization process is carried out according to the block diagram shown in Fig. 5.2. Multiple tests have been run on the extensive 4-dimensional search space, seeking for the optimal PSO coefficients and varying population sizes. It is important to remark that in this iterative procedure, each particle $X_j = [x_1j, x_2j, x_3j, x_4j]^T$ requires a new model set up modification of the one described in Section 2.

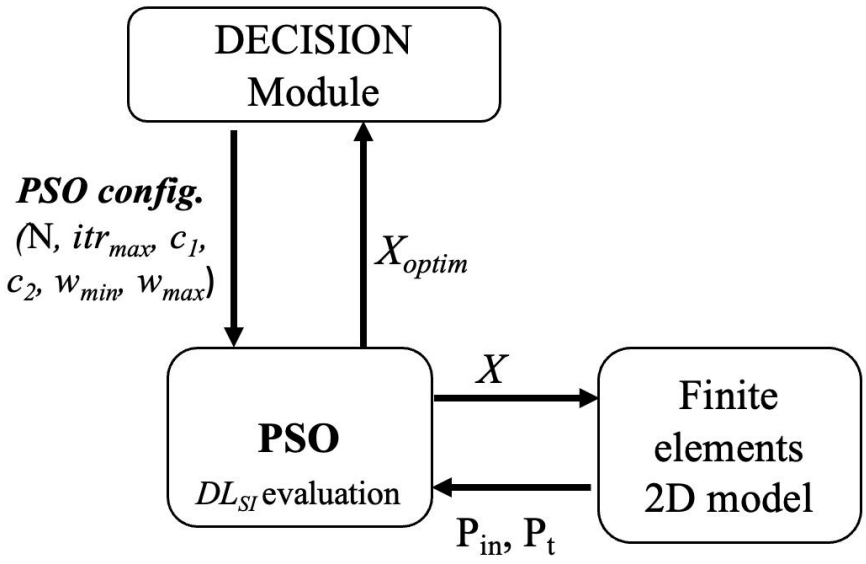

Figure 5.2: Block diagram of the PSO process.

5.4 Results

In this section the results of the PSO application are presented, together with the parameters that assure the best value of the fitness function and the behaviour of the optimized SCNB.

Acceleration Coefficients

Two different configurations of coefficients w, c_1 and c_2 have been chosen to run the optimization. The term c_1 stands for the cognitive component and depicts the tendency of the particles to go to their best positions, while the coefficient c_2 is the social component and depicts the attraction of the particle toward the location connected to the overall best value.

The first configuration is called **coef.1** where $w = 0.7298$, and $c_1 = c_2 = 1.49618$ are settled following the proposal of Shi and Eberhart [92], for a solid and fast convergence.

Moreover, to address the complexity of the $4-$dimensional search space, a second parameter configuration is considered for obtaining a wider exploration of the local maximums. Hence, in the second parameter configuration, called **coef.2**, it holds $w \in [0.9, 0.4]$ (i.e., the value of w decreases at each iteration k following equation 5.4, $c_1 = 1.53$ and $c_2 = 2.03$. In this second case more importance is given to the social behaviour of the particles (c_2) rather than the individual component (c_1) [90].

The faster convergence obtained with the configuration **coef.1** with respect to **coef.2**, is shown in the results of Fig. 5.3 in the 100 particles case.

PSO Computational Performance

The results obtained by considering different populations (50, 100 and 150) and the two proposed sets of coefficients in the $4-$dimentional search space are shown in the Fig. 5.3. We do not report the results obtained with larger number of populations because we verified that the results do not improve with the number of particles greater than 150.

First, population number is as much important as acceleration coefficients, since bigger populations can follow other particles and stop exploring just because the inertia and coefficients force to do it.

Second, as expected, **coef.1** goes into solid convergence results, but falling in local maximums, and it's only with the **coef.2** that allows better exploration when a global maximum is found. This final solution shows its

efficacy since the first iterations of 150 particles population case giving a global best value $\boldsymbol{DL_{SI}}$ **of 16.80 dBA** as Fig. 5.3 illustrates.

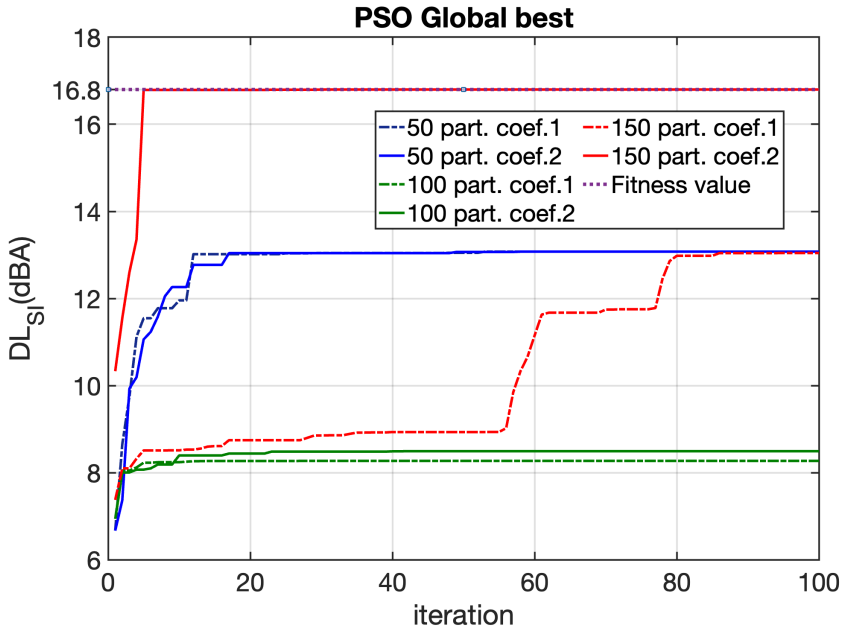

Figure 5.3: Particle Swarm optimization with 100 iterations and different populations and coefficients.

Even though the European standards only consider values with two decimals for the DL_{SI}, in order to model a more precise scatter, values until four decimals are evaluated to find the convergence. In Fig. 5.4, the meticulous adjustment of the fitness value and its convergence for the best optimization case are represented.

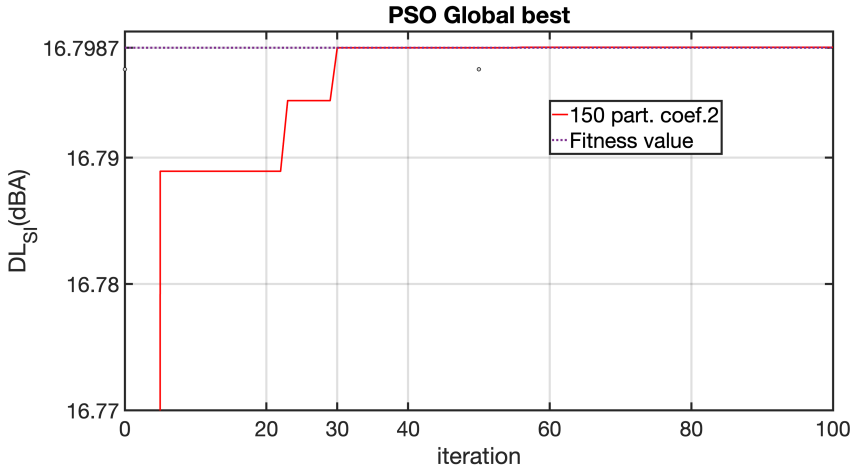

Figure 5.4: Convergence detail for the best configuration of coefficients and population.

In particular, Fig. 5.4 shows that the convergence of the Fitness value is found at iteration number 30 with a population of 150 particles, after simulating 4500 different models of the SCNB. By using the model described in Section 2, the computational cost of the result of each simulation is varying depending on the topology and how the elements of the domain are adapting to the shape with the FE mesh. Computational time of each simulation varies from 7 seconds to 20 seconds. The MATLAB environment is run in a single-thread mode with a computer MAC-mini equipped by a 3 GHz Intel Core i5 of 6 cores and 8 GB of RAM memory.

Fitness Optimization Parameters

Table 5.2 shows the values that maximize the fitness function and yield a ***DL_{SI}* value of 16.80 dBA** . The local maximums are always discovered with the same shape topology as the global optimal solution, but with a different lattice constant x_1. This makes the lattice constant be the dominant parameter and the most crucial one to set in the SCNB. The scatter's parameters (external and internal radius and mouth width) discover the global maximum by setting them to values just below the upper bound's limits. The periodic metamaterial's exterior radius is the 45% of the lattice constant value, the mouth of the resonator is 99% of the internal radius value, and the internal radius is 95% of the external radius.

The final 2D model of the SCNB with the optimized parameters is represented in Fig. 5.5 with a length of 0.81 m. That size will make it easier to place it in the highways and other noisy environments where the barrier

Table 5.2: Optimal Parameters X_{optim} that maximize the DL_{SI}

Parameter	Name	Value
x_1	Lattice constant (m)	0.3121
x_2	External radio (m)	0.1404
x_3	Internal radio (m)	0.1334
x_4	Mouth width (m)	0.2642
gbest	DL_{SI} - Single-number rating of the airborne sound insulation for road traffic (dBA)	**16.80**

will mitigate noise traffic spectrum. It is simple to see from the shape how large the inner resonant air mass is and how thin the surface of the C-shape scatterers is. The tiny amount of stiff material required in the future will reduce the costs associated with fabricating this wide-spectrum SCNB using 3D printing technology.

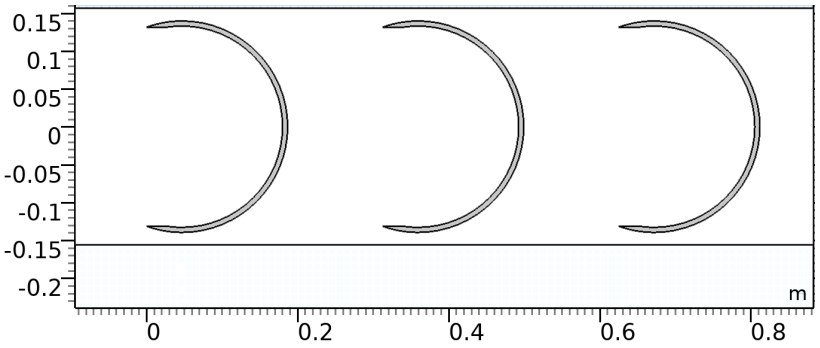

Figure 5.5: Detail of the 2D model with the optimized SCNB.

The Optimized SCNB behaviour

Figure 5.6 shows the outcome of the optimized SCNB sound insulation SI (equation 5.7) at 1 m away from the last scatter in a FEM simulation using the 2D model seen in Fig.5.1. The Helmholtz resonator's wide-open mouth, which is embedded in the scatter, enhances the barrier's low-frequency insulation, particularly in the range of 150–550 Hz, which is a recurring problem with complex real solutions for thin noise barriers (less than 1 m of length). In addition, Fig. 5.6 represents the third-octave band average of the spectrum that is used in equation 5.6 to evaluate the Fitness function. Also, those central frequencies showed in Table 5.1 are the ones considered in the

European Standards EN 1793-3 [39] and EN 1793-6 [40]: the average of values (in red in Fig. 5.6) of each frequency band helps to avoid the uneven behaviour at high frequencies (more than 1000 Hz).

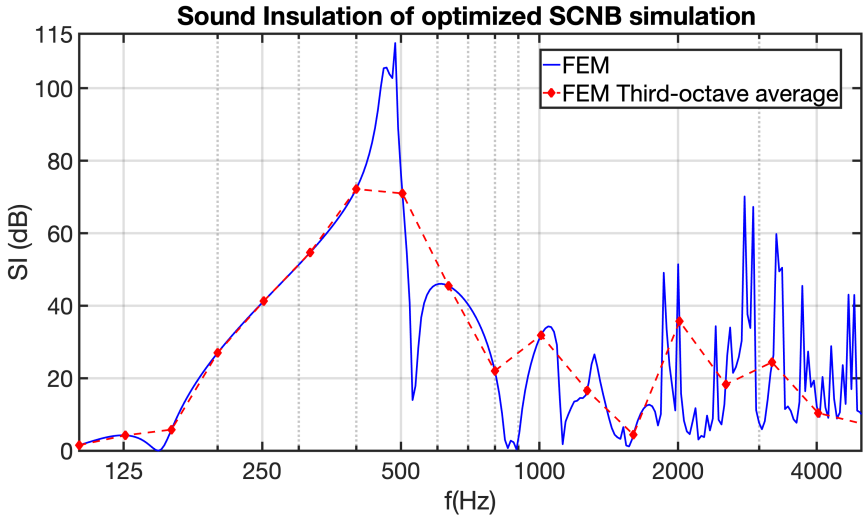

Figure 5.6: Sound Insulation (SI) of the SCNB FEM simulation that maximizes the Fitness function.

To show the noise maximum and minimum levels spatially distributed in the SCNB, Fig. 5.7a displays a Sound Pressure Level (dB) map of the model. In that representation it can be clearly seen the attenuation of approximately 90 dB in Fig. 5.7a at the shadow zone of the barrier, more specifically at the frequency of the maximum in the Insertion Loss spectrum. Fig. 5.6 shows the maximum sound insulation at 486 Hz which reports a value of 103.5 dB.

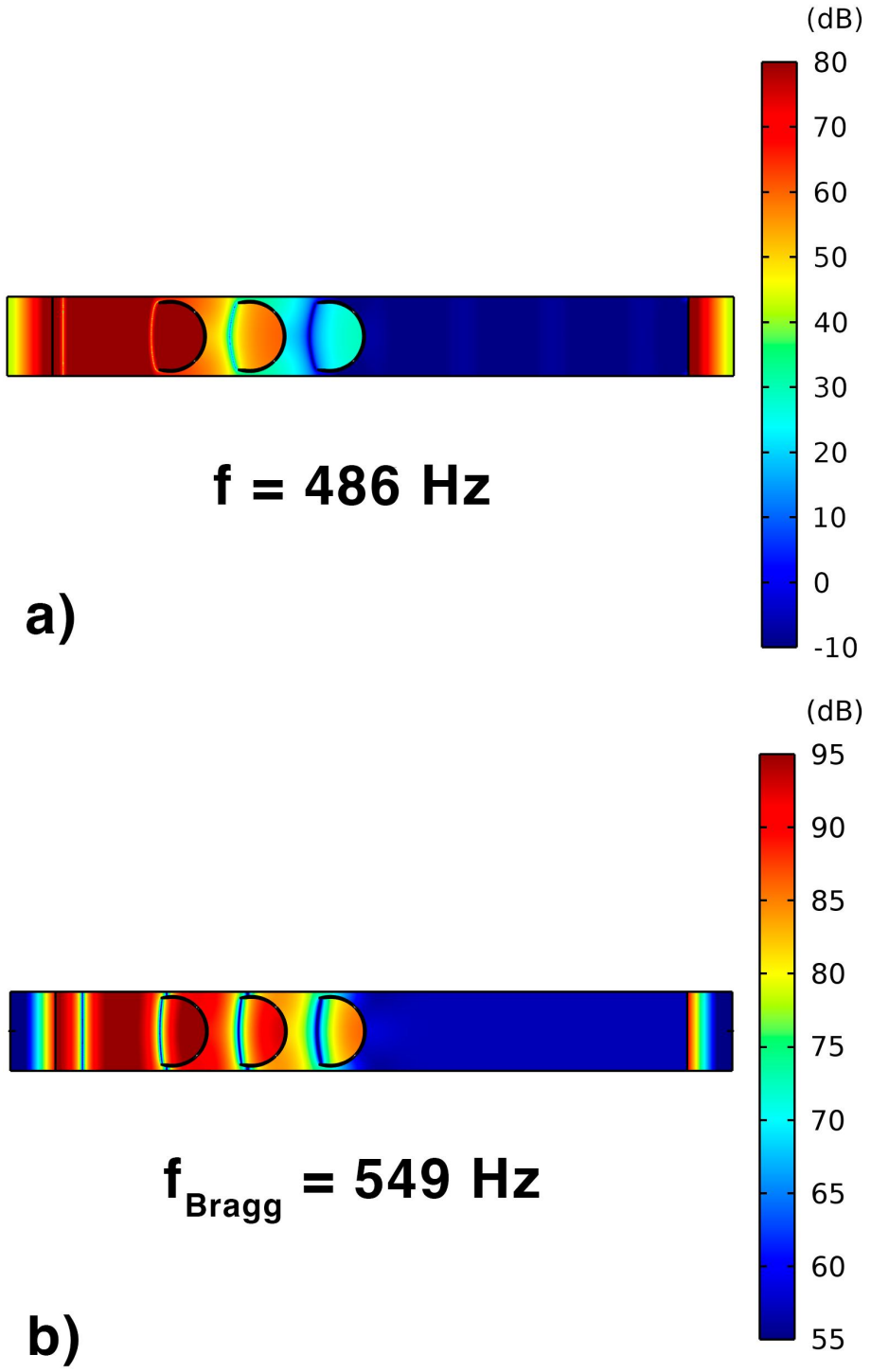

Figure 5.7: Maps of Sound Pressure Level (dB) of the FEM model at maximum attenuation frequency (a) and Bragg's frequency (b).

The first Bragg Band Gap (Bragg-BG) frequency produced physical structure of the barrier, and more specifically depending on the lattice constant (a) occurs at $f_c = 549$ Hz, and Fig. 5.7b illustrates a 40 dB attenuation level at that frequency.

The two noise-control mechanisms in this SCNB model are multiple scattering and Helmholtz resonances, although absorbent materials frequently utilized as a third to improve attenuation of higher frequencies [14]. Above 2 kHz, the harmonics of the BG and Helmholtz resonance frequencies produce enormous attenuation peaks with narrow frequency ranges, which increase the average attenuation of the SCNB, as seen in Fig. 5.6. The optimized barrier is assigned a D2 category in Table 5.3 of the European Standard Classification [40], rounding $DL_{SI} = 16.80$ dBA to 17 dBA.

Table 5.3: Categories of noise barrier according to their airborne Sound Insulation.

Category	Single Number Rating, DL_{SI} (dBA)
D0	Not determined
D1	< 16
D2	**16 to 27**
D3	28 to 36
D4	> 36

5.5 Discussion and Comparison

In this section, the results obtained by the PSO optimizations are compared with two optimization strategies: the GA and the random simulations. With the purpose of comparing the results with the methodology usually applied in these noise barriers optimizations with acoustic metamaterials, a benchmark with a GA is made [41]. In these optimizations, the diagram process is like the diagram shown in Fig. 5.2 but instead of updating the position of the particles, the GA changes the gens of the next generation of the population.

The algorithm parameters for all the population cases are the following: mutation probability equal to 0.1, crossover probability is 0.9, and 0 value of linear crossover. This configuration is established by default in the GA for a best behaviour in almost all cases. In Fig. 8, the performance of the optimization is represented, giving a convergence result of $DL_{SI} = 14.0861$ dBA, rounded to 14.09 dBA. One of the best properties of the PSO algorithm is its ability to avoid local maximums/minimums, and regarding the results obtained by the GA, is proved the fact that in the search space, it was a strong local maximum located at 14.09 that the PSO was capable to overpass, giving a result almost 3 dBA bigger than that value.

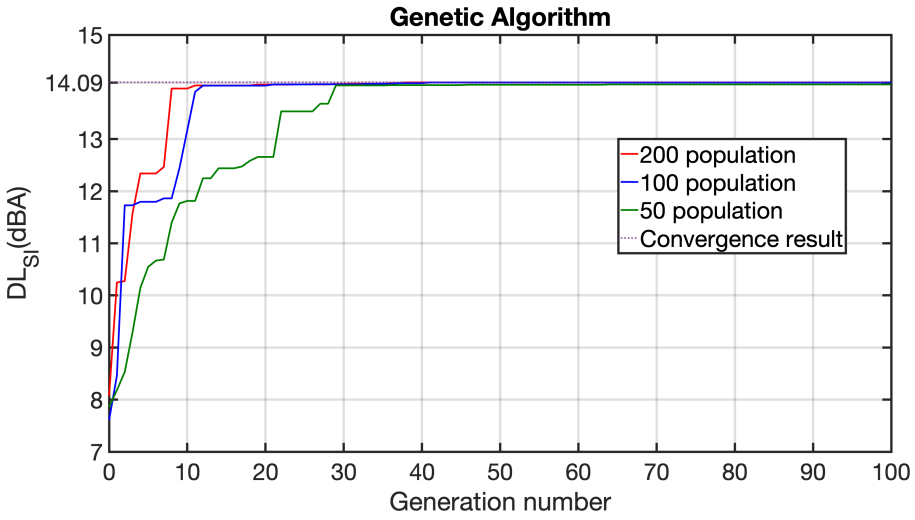

Figure 5.8: Genetic algorithm with 100 generation and different population sizes to optimize the SCNB model.

In order to have a more comprehensive understanding of the study case, a third method is compared to this SCNB model. In particular, the values of the SCNB model parameters are randomly selected in the interval

$[X_{\min}, X_{\max}]$ with uniform probability obtaining 4500 random SCNB models.

Figure 5.9 reports the best values of the fitness function (eq. 5.6) obtained by the GA (with 200 population and 100 generations), the PSO (after 4500 simulations and 150 particles at 30^{th} iteration), and the random methodology, respectively. In particular the random results are plotted by a "box and whiskers". As it clearly seen, both optimization algorithms (GA and PSO) have improved the random results. Also, they have brought values nearly the double of the Fitness function, with 14.09 dBA in the GA case and 16.80 dBA in the PSO case. Being this 16.80 dBA value the convergence result.

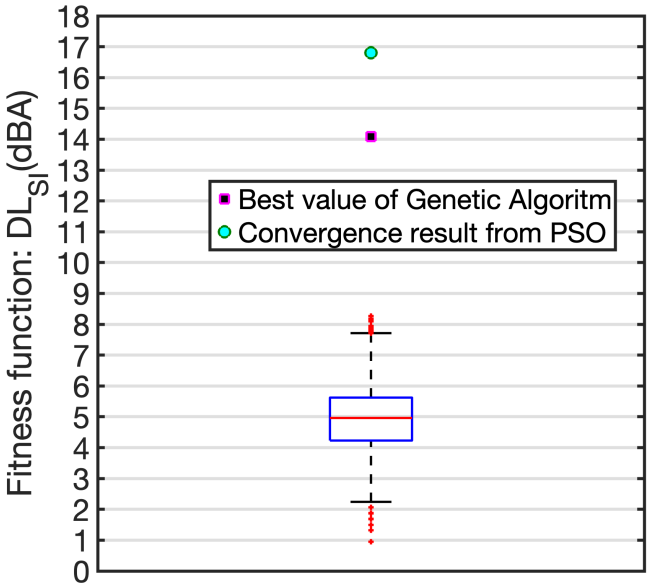

Figure 5.9: Box and whiskers plot of 4500 random simulations of the SCNB model and the best values of PSO and Genetic algorithm optimizations.

5.6 Conclusion

This chapter's main research objective was to optimize a 2D SCNB model, which is typically syntonized to attenuate a few chosen frequency ranges and making it cover the enough spectrum of traffic noise to give a high single value for its insulation. Without the addition of absorbent material, as wide-band sonic crystal existents in literature were prone to do, the PSO algorithm has brought about a novel topology for scatterers. Also, the thin geometry of the final scatterers will help to 3D printed or built it with low costs. This study has demonstrated how metamaterials like Sonic Crystals (SC) can have a strong performance as a noise barrier competing with the traditional barriers attenuation levels and tested with the European Standards by combining a PSO with FEM simulations in a periodic model. In particular, the single-number rating of the airborne sound insulation for road traffic is $DL_{SI} = 17$ dBA in accordance with European Standards EN 1793-6 and EN 1793-3. Regardless of the length of this optimized SCNB is shorter than 1 m (0.81 m), which makes it easy to install it along highway edges, and the Helmholtz resonances help it to achieve a very high level of low-frequency noise insulation. According to the classification of European standards, the sound insulation single value (DL_{SI}) of 17 dBA is a D2 category barrier.

In the future research, a comparison with other numerical methods as Finite Difference Time Domain (FDTD) or the experimental validation of the results will be considered.

6 Parametric modelling of Resonant Sonic Crystal Noise Barriers. Case of Train Brake Noise

6.1 Introduction

In today's industrialized world, noise pollution is a pervasive issue with significant implications for public health and well-being [20]. Road traffic noise, especially mid-to-high-frequency components (1 kHz to 5kHz) have produced several health related depression issues [94].

Among all different transportation vehicles, trains are the ones with highest levels of noise at those frequencies, where human hearing sensitivity has low audibility threshold and the annoyance is greater [95]. In particular, the most annoying noise produced is the train brake noise (TBN), an unpleasant noise that typically ranges from 2.0 to 4.5 kHz as several studies have proved [96, 97, 98, 99, 100]. More precisely, Chiello et al. [96] and Cascetta et al. [97] analysed different models of disc brakes in numerical and laboratory studies, while Jansen et al. [98] and Lázaro et al. [99] measured some trains braking in the railways at different velocities. For effective noise reduction strategies, extensive research has been carried out at three key stages: near the noise source, during transmission and at the receiver. A widely adopted approach, primarily due to its simplicity, is to use devices at the transmission level, in particular Noise Barriers (NB), to mitigate noise propagation [21, 58]. The performance of these NB structures can be enhanced by carefully tailoring their geometrical properties, including the shape of their edges and the curvature of their primary surfaces, to control sound diffraction [101]. In addition, the incorporation of porous materials into NBs further improves their acoustic efficacy, particularly with respect to the reflection of sound waves between the source and

the barrier structure [102, 103].

In this scope of noise mitigation, a novel methodology has gained prominence in recent decades, offering some advantages compared to conventional noise barriers: Sonic Crystal Noise Barriers (SCNBs) [32, 27, 16]. SCNBs incorporate periodic materials known as sonic crystals, which consist of arrays of scatterers embedded in air [26]. SCNBs can be strategically arranged to attenuate noise within specific target frequency ranges and this, a capability that sets them apart from traditional barriers incapable of distinguishing between different types of noise. SCNB are also permeable to fluids, and in the case of train noise mitigation, open barriers have tested its benefits compared with closed ones [104, 105, 106, 107]. Notably, SCNBs exhibit a characteristic feature called Bragg bandgaps (Bragg-BGs), which are frequency ranges where acoustic waves are prohibited from propagating due to the in-terference generated by multiple wave scattering [24]. The central frequency of the first Bragg-BG is determined by $f_c = c/2a$ (eq. 2.10), with c representing the speed of sound in the fluid (m/s), air in this case, and a denoting the lattice constant, which is the distance between scatterers, characteristic of the unit cell in a crystal lattice [8]. Bragg-BGs have revolutionized the control of wave prop-agation and found applications in diverse fields different from NBs such as waveguides [17, 108], diffusers [15] and windows [109, 110].

In addition to Bragg scattering, bandgaps can also be generated through resonant cavities [111, 112, 113, 114, 14]. The resulting bandgaps based on local resonances of Continuous Cavity Resonators (LR-BGs) depend on the alignment of the resonator's mouth with respect to the incident sound wave. It is worth noting that LR-BGs have a more limited frequency range compared to Bragg-BGs. The interaction between LR-BGs and Bragg-BGs has been explored [115, 116, 117] and at times, the interaction between these two wave propagation phenomena fails to yield improvements in the sound insulation ca-pacity of SCNBs [118, 119].

To improve the performance of SCNBs further, additive manufacturing (3D printing) technology has opened up unprecedented flexibility and customizability of products. It is widely recognized as a sustainable technology able to achieve low costs, reduce waste, and simplify the supply chain [54]. Recent research has demonstrated that 3D printing can work in tandem with parametric modeling to produce designs that are easily changeable across all physical parameters. Parametric modeling, a type of computer-aided design (CAD), allows for the exploitation of mathematical equations to build geometry, enabling complex designs to be optimized in an automated manner. Over the past decade, 3D-printed acoustic metamaterials have become popular, especially with porous materials such as Acrylonitrile

Butadiene Styrene samples with Cartesian and octagonal patterns [120], or square and rectangular matrices of Helmholtz resonators [121]. However, most experimental validations have been carried out with small samples in the impedance tube [122], and without testing 3D-printed SCNB [123].

This study aims to bridge the identified gap by examining the impact of the interaction between Local Resonance Bandgaps (LR-BG) and Bragg Bandgaps (Bragg-BG), particularly focusing on the enhancement of Bragg-BG insulation capabilities when the LR-BG exhibits higher frequencies. Emphasis is placed on the orientation of the mouths of locally resonant scatterers relative to the incident waves, significantly influencing the overall noise insulation effectiveness of SCNBs. Also, one of the primary aims is to experimentally validate the optimal configuration of resonant scatterers to maximize the acoustic insulation properties of SCNBs, thereby offering a practical solution to mitigate Train Brake Noise (TBN). The proposed research exploits the synergic combination of parametric modeling, FEM acoustic performance simulation, and 3D printing prototyping to design an effective SCNB, customizable for specific target frequencies. This approach aims to provide a more comprehensive understanding of the factors influencing SCNB performance and demonstrate the practical implications of scatterer orientation on enhancing noise insulation.

The proposed methodology implies the following steps:

- Firstly, thanks to the parametric modeling described in section 3.4, it is possible to design the resonant scatterers and their periodicity in the sonic crystal according to the desired target frequencies.
- Secondly, low computational numerical simulations would help to determine if any modifications should be made in order to achieve the performance of the desired Sonic Crystal Noise Barrier (SCNB).
- Thirdly, a laboratory test following the ISO 10140-2:2021 [124] standard is conducted to experimentally validate the insulation provided by the 3D printed SCNB.
- Afterwards, to evaluate the performance as a noise barrier, the finite shape of the prototype should be evaluated to consider the border diffraction.
- Subsequently, an experiment in an anechoic chamber with normal incidence is carried out to evaluate the previously mentioned effects that were not taken into account when only evaluating the transmission in the initial design process.

- Lastly, the correct placement of the HR mouth in the scatterers of the SCNB will be studied and compared with a conventional barrier (CB).

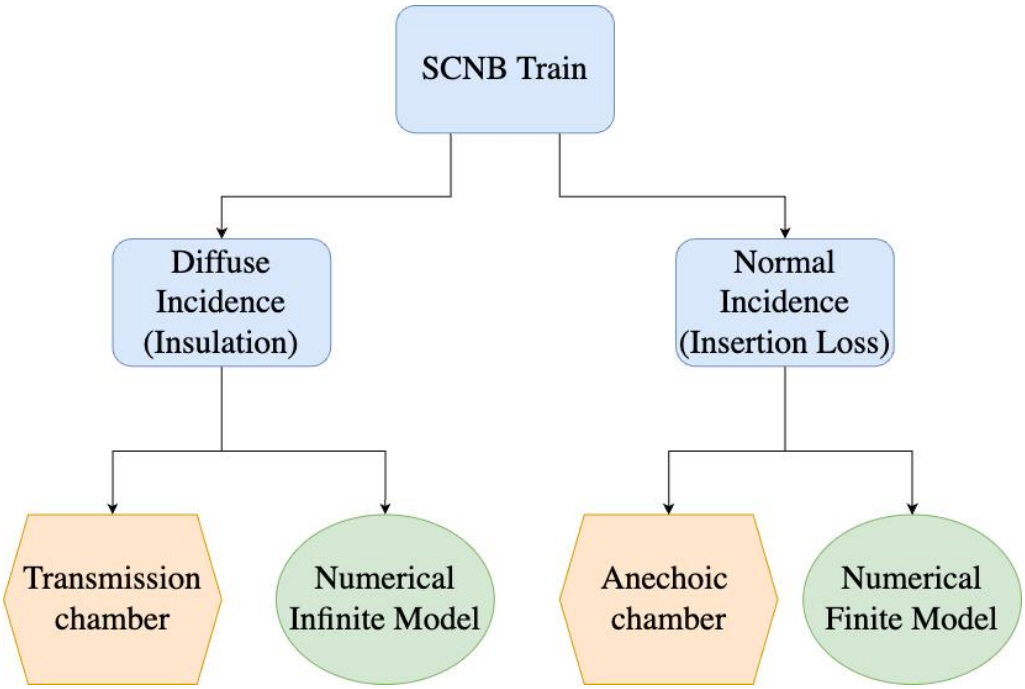

Figure 6.1: Chapter outline: the experimental part is in orange, and the numerical part is in green.

6.2 Materials and Methods

One of the main steps of the methodology are the numerical simulations of the noise barrier acoustic performance by using FEM. Typically, such software can be used to obtain solutions to a broad spectrum of engineering problems including thermal, structural, and acoustic investigations. In the proposed approach, the FEM is used in synergy with parametric modelling by setting an iterative procedure in order to improve the parameters of the model before the 3D printing.

The objective concerns the identification of the best parameters to achieve effective insulation of target frequencies and ensure user comfort related to the perceived noise. In particular, the key dimensions of the model are varied (e.g., thickness or spacing of the resonant SC periodic network) and the FEM analysis is repeated until target performances have been reached (and the effective geometrical dimension has been identified).

Such operation is simpler and faster if the parametric model allows changing all the key parameters influencing the performance of the barrier.

2D Periodic Model

Moreover, for resonant SCNB, since the FEM model of the SCNB has square symmetry and the structure does not change along the Z-axis, a 2D model can be used in the XY plane. Indeed, the 2D model can be easily extracted from the parametric model to analyse the acoustic behaviour of the barrier with a low computational cost. Fig.6.2 shows the SCNB scatterers (with parametrised topology) placed in a periodic network where the horizontal contours (bottom and top) have a periodic condition. Such features allow the model to have the characteristics of a semi-infinite length barrier with the width of the model dependent on the lattice constant. The proposed FEM modelling approach can consistently reduce the computation time while maintaining high accuracy of the result. Indeed, since the model is periodic, we can analyse only one row to evaluate the performance of this barrier. In more detail, in the model the vertical contours have an adapted boundary condition of Perfectly Matched Layer (PMLs) to prevent unwanted reflections (free field condition)[50]. An incident plane wave (IPW) travels from left to right in the domain of the model and the measurement point is placed 1 meter away from the last scatter. This model can be adapted to each case study and target frequencies by modifying the lattice constant a (distance between two scatterers in the network), the

number of rows of the barrier and the topology of the scatterers. The measures are considered in the shadow zone of the barrier, where the insulation is effective.

The noise barrier performance is described by a noise spectrum insulation parameter called Transmission Loss (TL), which the difference in decibel between the direct sound pressure level (SPL) L_d(dB) received before placing the barrier and the sound pressure level L_i(dB) when the barrier is inserted:

$$TL = L_d - L_i \quad [dB] \tag{6.1}$$

Based on the noise target frequencies, a first improvement of the parametric modelling can be achieved by varying the model physical topology or SCBNB parameters, based on information acquired from the physical acoustic theory of Helmholtz resonances and the MS. Indeed, such qualitative adjustment can speed up the subsequent iterative phase of FEM simulation and parameter optimization.

In such a 2D model, the TL parameter is calculated at the measurement point of the FEM simulation model. More precisely, the measurement point is always placed 1 meter away from the last scatterer, meaning its position depends on the number of scatterer rows in the barrier and the length of the SCNB along the X-axis (Fig. 6.2).

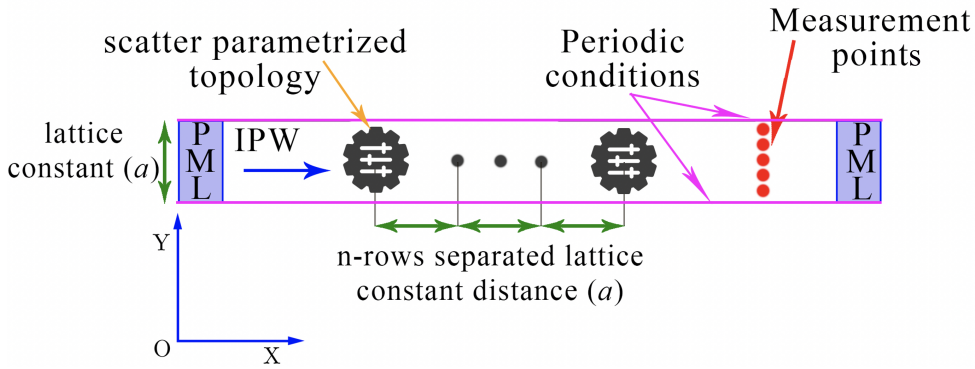

Figure 6.2: Periodic FEM generic parametrized 2D model.

Parametric customization for Target Frequencies

When the target frequencies range from 2.0 to 4.5 kHz (as explained in introduction), the noise-control mechanisms are adjusted to act in this range starting from a geometry following theoretical formulas of Braggs law [7](se eq. 2.10) and Helmholtz Resonator's main frequency (see eq. 2.70).

Fig. 6.3 represents an example of a Helmholtz resonator syntonised for the TBN spectrum to attenuate. Even if the parameter D is not present in Equation 2.70, it is important to obtain the parametric model and it holds L=(External radius - D). According to the specifications shown in Fig. 8, the lattice constant is adjusted to $a = 0.055$ m to obtain the BG with $n = 1$ equal to $f_c = 3.1$ kHz and the Helmholtz resonator syntonized to $f_{HR} = 5.3$ kHz (see Fig. 6.3).

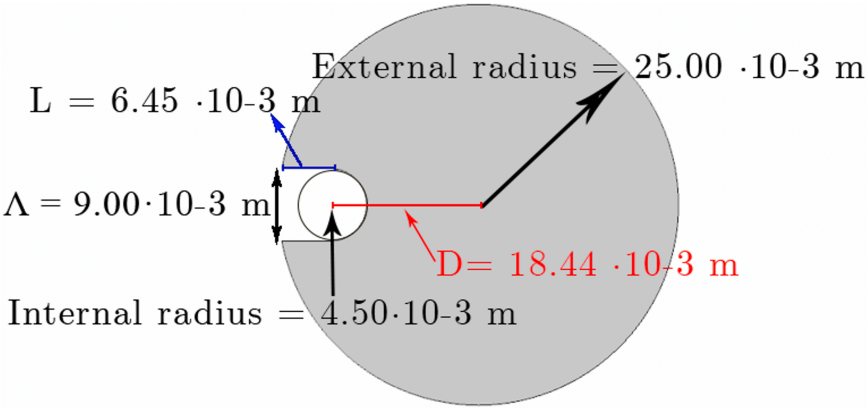

Figure 6.3: 2D design of a cylindrical scatter with a HR.

3D printing and validation tests

The last step of the proposed procedure concerns the effective 3D-printing of the designed noise barriers. In this final phase, the 3D model (customised for specific target frequencies) is processed through "slicing software" to generate the code for the 3D printer, i.e., a toolpath to provide the machine with the instructions for production.

Once the barrier is 3D-printed, the laboratory test is performed by the simulation validation and the performances evaluation. To verify the simulation results of the 3D printed SCNB insulation, an international standard procedure (ISO 10140-2:2021) is applied to exploit a transmission chamber (*ISO 10140-2:2021 "Measurement of airborne sound insulation," in Acoustics — Laboratory measurement of sound insulation of building elements"*).The transmission chamber used for the test is composed of two enclosures (emitting enclosure and receiving enclosure) and separated by a frame (that includes the component to be tested). In such a procedure, the transmission chamber enables on experimentally measured TL defined by equation 6.1 and evaluated in the numerical simulation.

Operatively, in the proposed work the validation is performed by comparing the FEM model and experimental test through the transmission

coefficient $\tau \in [0, 1]$ that expresses how much noise is passing through the barrier. It is related to TL by the following equation:

$$\tau = 10^{-\frac{TL}{10}} \tag{6.2}$$

It is worth noting that τ can be deduced both from the experimental test and FEM simulations and it is widely used to validate acoustic metamaterials insulation [31, 114, 125]. More in detail, in the proposed test, TL is evaluated according to the ISO 10140-2:2021 standard. Applying the diffuse field model and the coupled enclosure theory [126, 127], the TL can be obtained by the following expression:

$$TL = L_1 - L_2 + 10 \cdot \log_{10}\left(\frac{S}{A}\right) \quad \text{[dB]} \tag{6.3}$$

where L_1 is the sound pressure level produced in the emitting enclosure, L_2 is the sound pressure level measured in the receiving enclosure, S is the surface area of the separator element (the component under test) and A is the equivalent sound absorption surface area in the receiving enclosure (a known value that depends on the reception chamber used).

Several works have shown that after 4 rows the increase in the performance of the SCNB is not so remarkable [27, 128], that is why, 4 and 5 rows of scatterers, the prototype and laboratory tests were conducted for these two configurations. The prototypes were made in scale 1:2 by using a FDM 3D printer technology (Fig. 6.4). This scale will make necessary to scale the frequency when testing the acoustic performance of the prototype, as it has been made in most of the related literature previously mentioned works.

The printer used is a Ultimaker S5 chosen for its printing area sufficient to print the prototype and for its high printing quality. The printed material is polylactic acid and it is printed at 220° C with a diameter of 0.4 mm and a heated bed at 60° C. The layer height (printing resolution) is about 100 microns. The software used to operate the slicing and provide the machine with the toolpath instruction is CURA (version 4.13.1) which is chosen for its compatibility with Ultimaker S5 3D printers. In particular, CURA is an open source slicing software able to transform the digital 3D model into data for the Ultimaker S5 3D printer.

With the purpose of verifying the insulation through the metamaterial printed prototype and the main performance of this SCNB, an experimental validation is performed following the international standard ISO 10140-2:2021 ([124]). The experimental validation is conducted at the Escuela Politècnica Superior de Gandía laboratories (in Gandía, Spain) exploiting

a scaled transmission chamber. In particular, the experimental apparatus includes: 1) emission and reception enclosures; 2) a separator frame and 3) noise generation and measurement equipment. The used equipment is compliant with the standards (ISO 10140-2:2021) and is widely used in previous research [129, 130].

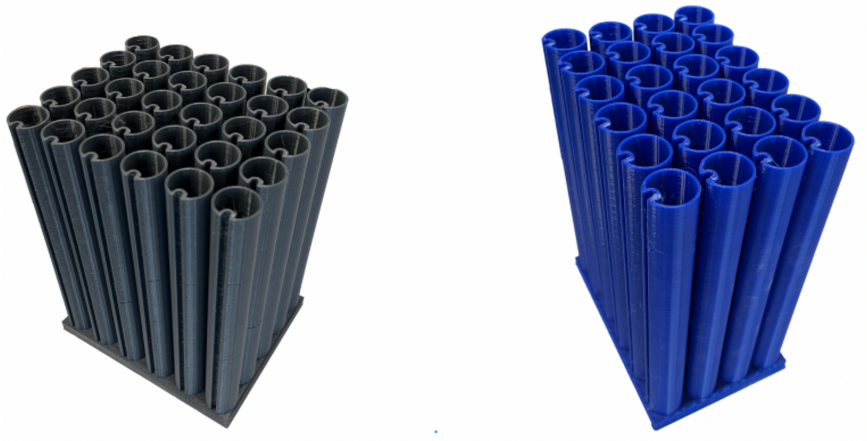

Figure 6.4: 3D-printed prototypes with: (a) five rows; and (b) four rows of scatterers.

The emission chamber has a volume of 0.44 m^3 and an absorption area of 0.17 m^2, while the reception one has a volume of 0.38 m^3 and an absorption area of 0.15 m^2. Regarding the interior cladding, it is covered by a panel consisting of two aluminum layers of different commercial thicknesses, bonded by a core of Low-Density Polyethylene. The sound meter is connected through a wire as shown in Fig. 6.5.

Figure 6.5: Emission and reception chambers.

To adapt the scaled 3D printed prototypes to the separator element between the transmitting and receiving chambers, a solid wood adapter frame is used. The wood employed for the frame is rigid and free of porosities to avoid problems influencing transmission. The 3D printed SCNB is placed in the centre of the frame to evaluate its insulation, as Fig. 6.6 shows.

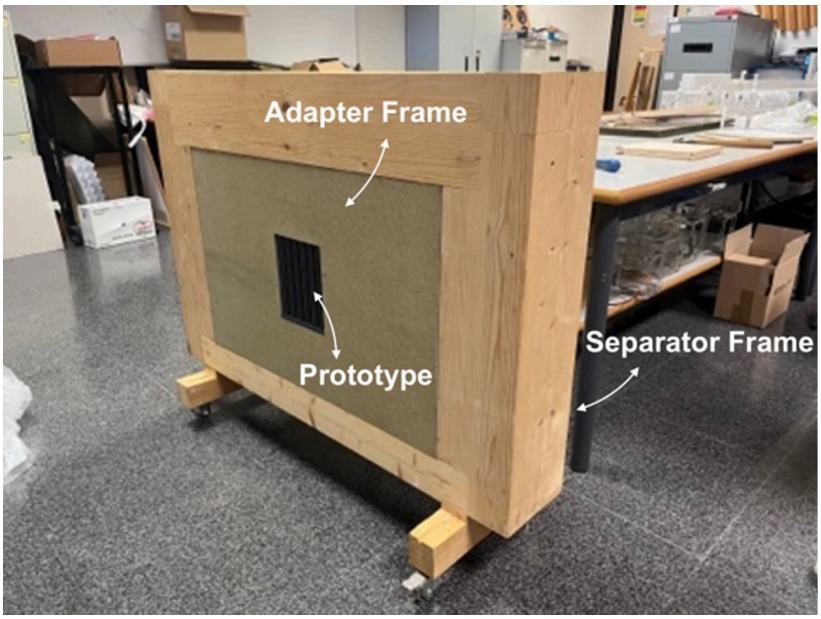

Figure 6.6: Wood frame with the 3D-printed prototype inserted.

According to ISO 10140-2:2021 standard, 5 different microphone positions have been measured in both the emission room and the reception room. The remote rotary webcam, united with a precision sound meter microphone allows easily acquiring data from different samples in emission and reception chambers. Fig. 6.7 shows how the microphone is located according to the webcam image. The source of white noise is generated with the sound meters and reproduced by a sound speaker as Fig. 6.7 illustrates. The experimental tests were executed 3 times to prove the repeatability of the experiment. The microphone used from the sound meter Brüel & Kjær 2250 is model 4189 with a preamplifier type ZC 0032. The active speaker is a Genelec 6010A.

Figure 6.7: Measurement equipment.

In addition, a remote control acquisition software interface is used and shown in Fig. 6.8. The employed software is the remote camera control (*aqprox!*), connected by IP in the same internal university network. The microphone is attached to the camera so, rotating the camera up-down, left-right the direction of the microphone is changed.

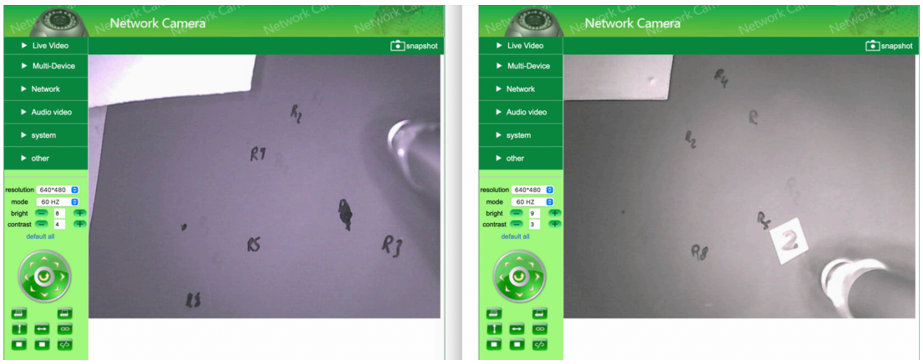

Figure 6.8: Remote control acquisition software interface.

2D Finite Model

Once the final prototype is printed, and its insulation performance would be evaluated according to international Standards, new FEM numerical simulations are performed to evaluate the transmission of two-dimensional SCNBs and compare its performance with a conventional barrier (CB).

The CB is a flat wall with the same dimensions of the SC ones and the SCNB consists of a set of locally resonant scatterers distributed in a square periodic lattice with two different orientations of the resonant cavity with respect to the noise source (0° and 90°) as shown in Figure 6.9. By

evaluating the insulation provided by the rigid flat barrier a comparison is possible to the maximum possible level considering the border diffraction according to the SCNB dimensions.

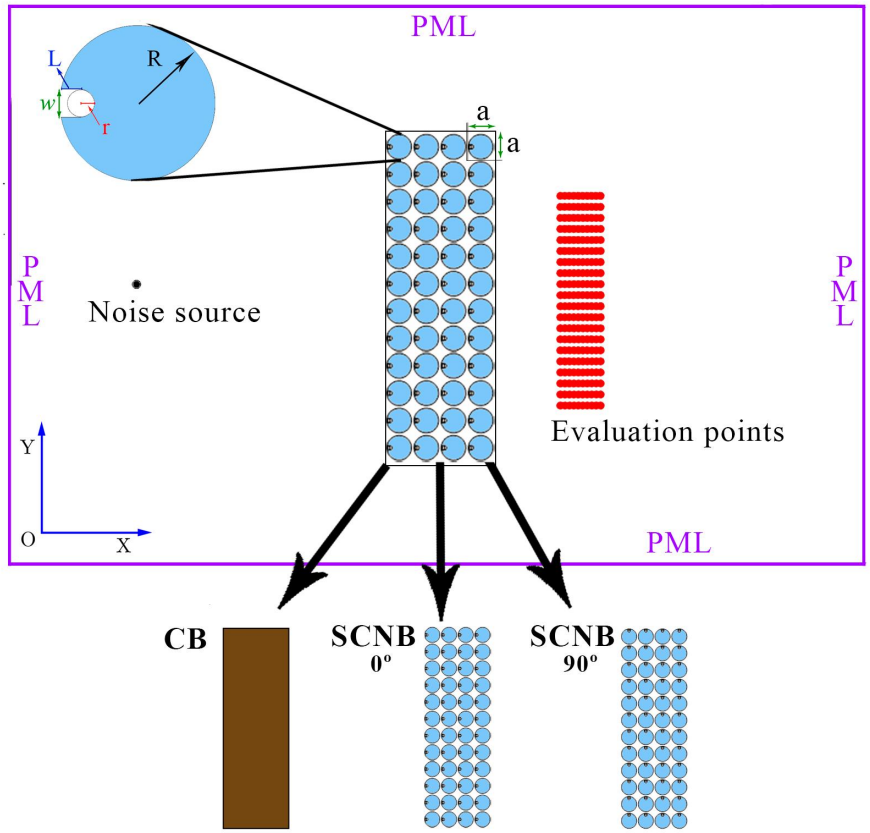

Figure 6.9: Numerical FEM model of the resonant scatter at 0° and 90°(upper part), simulation domain with the 4x12 SCNB at 0^{o}(middle part) and the three different barriers, CB, SCNB 0° and SCNB 90° (lower part).

In Figure 6.9 illustrates the 2D SCNB model under investigation, which is defined by a square-periodic structure of 4 rows and 12 columns. The dimensions of the three barriers are the same, 11.5 cm of width (X-direction) per 0.36 m of length(Y-direction). In the Fig. 6.10 b the dimensions are shown.

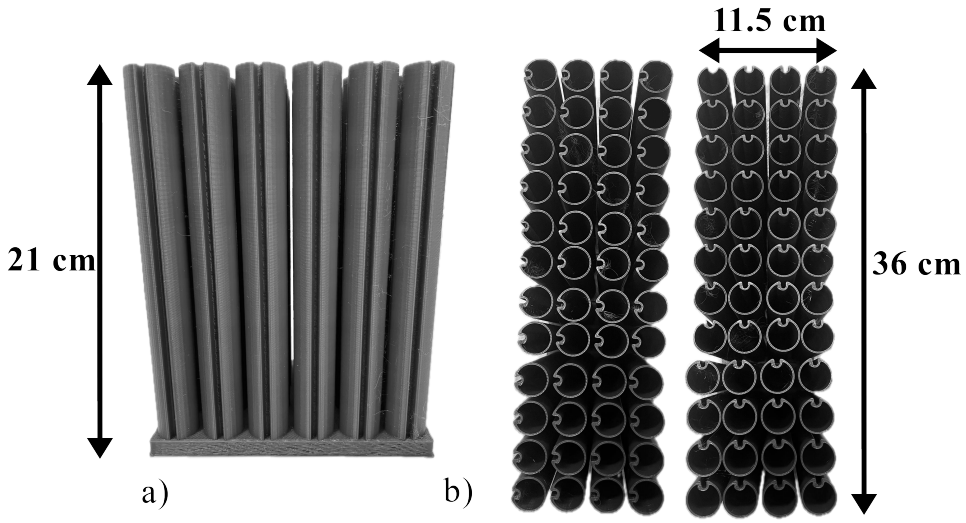

Figure 6.10: 3D Printed 1:2 scaled SCNB PLA prototypes a) Front view of the scaled SCNBs with the resonant cavity at 0º; b) Top view of the scaled SCNBs at 0º and 90º configurations.

The noise source is located at 30 cm from the barrier at the left part of the domain and in the centre of the barrier. It is radiating 1 Pa of acoustic pressure.

It is placed in a rectangular domain of 50 cm of width (X-direction) per 80 cm of length (Y-direction).In this domain, the boundaries are Perfectly Matched Layers (PML) [50], usually applied to absorb waves propagating outward from the domain due to their non-reflective properties.

In this 2D model, 3-node triangular elements were utilized to construct the mesh, ensuring convergence by using mesh elements with a maximum size able to evaluate 8 points per wavelength even at the maximum frequency of the study (4.5 kHz).

The resonant cavity of the scatterers is depending on the length of the neck (L), the width of the mouth (w) and the inner surface area ($S = \pi r^2$), being r the inner radius of the surface of the locally resonant scatterer. The scatterers are assumed to be rigid neglecting the acoustic-structure coupling. In this work, the numerical study and prototyping are carried out on a 1:2 scale model, including viscothermal losses. It is important to note that in full-scale applications, these viscothermal losses are slightly different as they are not directly scalable. Nonetheless, the research proceeds with the understanding that the variations in viscothermal losses do not critically impact the fundamental acoustic performance of the SCNB for reducing TBN. These viscothermal losses in the medium are implemented in the

local resonant slit of the scatterer, according to the following equations of the complex density and the complex impedance [131]:

$$\rho_c = \frac{\rho_0}{\Psi_v} \quad \left[\frac{\text{kg}}{\text{m}^3}\right] \tag{6.4}$$

$$Z_c^2 = \frac{(\rho_0 c)^2}{\Psi_v\left(\gamma - (\gamma-1)\Psi_t\right)} \quad \left[\frac{\text{Pa}\cdot\text{s}}{\text{m}}\right] \tag{6.5}$$

where γ is the specific heat ratio in the air, and Ψ_t, Ψ_v are the analytic expressions of the mean values of the viscous and thermal fields (ϕ is either v or t) in the resonator neck:

$$\Psi_\phi = 1 - \frac{\tan\left(k_\phi \frac{w}{2}\right)}{k_\phi \frac{w}{2}} \tag{6.6}$$

with w being the width of the mouth of the local resonator. For further details on the implementation of viscothermal losses in the FEM model see section 3.3.

The transmission of the system is analysed in the evaluation points at distance from 0.06 m to 0.1 m from the barriers by evaluating the Insertion Loss (IL) in decibels defined by:

$$IL = 10\log_{10}\left(\frac{\langle P_d^2\rangle}{\langle P_b^2\rangle}\right) \quad [dB] \tag{6.7}$$

where <> represents the average value of all evaluation points of the squared direct acoustic pressure without the barrier (P_d) and the squared acoustic pressure after placing the barrier (P_b). This parameter indicates how the sound pressure level at the evaluation points changes when the SCNB is positioned in the acoustic path of the incident wave.

Considering the TBN frequency range (2 kHz - 4.5 kHz), the distribution of the scatterers in a square lattice SCNB was chosen to have a first Bragg-BG at 3.1 kHz, being $a = 0.055$ m. The band structure plotted in Fig. 5 illustrates the complete Bragg-BG and the pseudo-BG in ΓX directions. In aiming to strike a balance between insulation and permeability, a filling fraction of $ff = \pi(R/a)^2 = 0.64$ is established, where R represents the external radius of the scatterer.

Normal incidence experimental test

In order to validate the resonant SCNBs experimentally, a 3D-printed prototype on a 1:2 scale was produced from polylactic acid (PLA) material.

Further details about the 3D printing process were explained in previous sections.

In particular, Fig. 6.10 a displays a frontal view of the SCNBs with the local resonator at 0°, while Fig. 6.10 b presents a top view of the SCNBs in the two configurations, 0° and 90°, respectively on the left and right. Due to the size of the 3D printer, the SCNB was printed in two identical modules. One of them is showed in Fig 6.10 a and the entire SCNB is showed in the Fig. 6.10 b.

To assess the noise insulation produced by the SCNBs and to verify the importance of the orientation of the resonant cavity with respect the noise source, acoustic experiments were carried out in the anechoic chamber of the Higher Polytechnic School of Gandía. In addition, a conventional flat barrier of the same size is tested to compare the results and observe the upper and border edges diffraction limit. The dimensions of the scaled barriers are 21 cm of height, 11.5 cm of depth and 36 cm of width.

A Genelec 8030A active loudspeaker is used as the sound source positioned 30 cm from the centre of the barrier, being the same distance of the 2D numerical model. Two condenser microphones Behringer ECM8000 are used to measure the acoustic pressure at 6 cm and 10 cm of distance from the barrier. The distances of 6 cm and 10 cm were chosen to ensure placement within the "shadow zone" of the barrier according to its dimensions. Two different measurement heights at 10 cm and 12 cm have been chosen to avoid possible resonances due to same wave path length. Before using them, they were calibrated with the Brüel & Kjær Sound calibrator type 4231 Class 1. A device designed for accurate in-field acoustic calibration of microphones and other sound measurement equipment.

They are located in the centre at a distance of 8 cm from the central edge and at a distance of 10 cm on the right and left sides of the barrier as shown in Fig. 6.11. At these positions, the CB, the 0° SCNB, the 90° SCNB and the case without barrier are measured to obtain the IL results. The measurements were carried out with a M-Audio M-Track MKII soundcard and emitting sine sweeps signals from 2 to 9 kHz. In all barriers, three sine sweeps meas-urements were averaged. This type of signal facilitates the assessment of the impulse response for a time-invariant linear system by cross-correlating the recorded signal from the microphone.

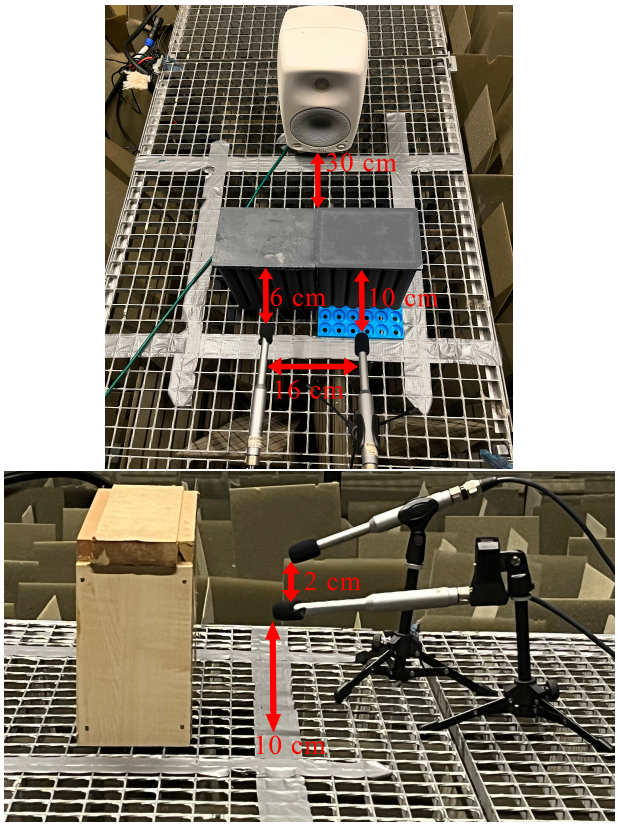

Figure 6.11: Experimental set up measurement system. up) SCNB measurement; down) CB measurement.

6.3 Results

This section presents first the results of the insulation provided according to the international standard ISO 10140-2:2021, both numerically and experimentally.

After, the numerical results of the 2D Finite FEM model described. And finally, the experimental results obtained by measuring the scaled 3D-printed prototype with 0^{o} and 90^{o} orientation, comparing both with the CB.

ISO 10140-2:2021 results: Numerical and Experimental

The results of the experimental phase emphasize a double aspect. First, it is possible to validate the FEM model by comparing the numerical simulation with the data acquired during the laboratory test. Second, the results confirm that the insulation of the barrier in the TBN range is effective with better performances if the number of scatterer rows increases.

To validate the FEM model, the transmission coefficient τ is calculated in both the numerical simulation and the 3D-printed prototypes. This parameter shows how much noise is passing through the barrier. Such normalized parameter can be used to compare and validate the experimental result.

The experimental test and consequent validation are repeated for the two different 4 and 5 rows barriers that can insulate the defined target noise spectrum. The comparison between the numerical simulation and their experimental validation is shown in Fig. 6.12. In particular, the figure shows a small deviation between the two curves (experimental and numerical) in the insulation of the SCNB according to the TBN frequency range. The FEM model can be considered validated since the average differences between the experimental and numerical curves of (τ) results less than 5.62% in the 4-rows case and 2.82% in the 5-rows case in the defined TBN range. The slight differences with the experimental results are related to the use of a 2D periodic model, where the upper-edge and border-edge diffractions are not considered and are evaluated in the next section. On the other hand, such slight error is acceptable and in line with other investigations simulating noise barriers [31].

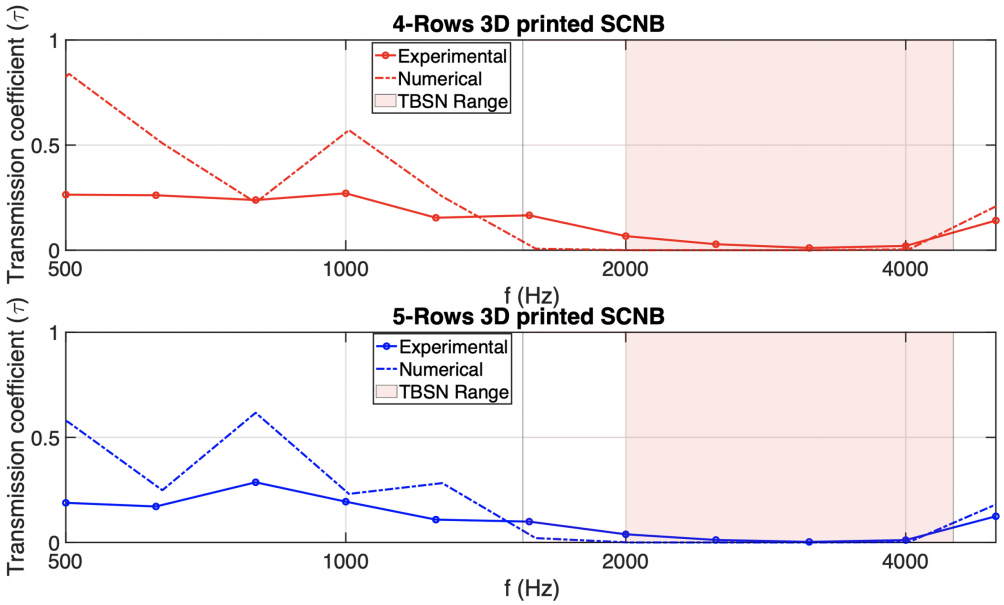

Figure 6.12: Transmission coefficient (τ) of four-row and five-row SCNBs with the FEM results and its experimental validation tests.

The second aspect of the validation concerns the noise mitigation in the required frequency range. The results confirm that the proposed metamaterial barrier is perfectly tuned to the target frequency noise range. Indeed, the evaluated coefficient (τ) illustrates that there is almost no noise passing through the barrier in the TBN range and that's why the value is zero or very close to zero. More in detail, for the 5 rows case, the insulation (in the interest range) is bigger than the 4 rows case, with values closer to 0 transmission and small transmission passing in the rest of the spectrum. These additional results confirm that the 4 and 5 rows cases are effective but with a slightly more efficacy in the barrier with 5-rows.

Numerical

Since the main purpose of SCNB is to achieve a similar insulation level that a CB could provide, the comparison is necessary to get a more global picture of the case under study.

Figure 4 shows the numerical results of the FEM simulations obtained from the 2D model explained in section 2.1. With the same dimensions of the proposed SCNB, a CB can achieve 20 to 25 dB of IL in the studied TBN frequency range (2 kHz - 4.5 kHz). The numerical IL is calculated at the evaluation points from the acoustic pressure with and without the barrier for each case, following from 6.7.

An open barrier such as the SCNB, has lower levels but is competitive at some frequencies. One of the most important points to consider is the orientation of the mouth of the resonant cavity according to the noise source. With this rotation, a high reduction is observed when the mouth is set to 90°. In a large part of the target frequency range (2.85 to 4.2 kHz, with colour gradient) of the TBN (green colour), differences of up to 27 dB in the IL are observed when the scatterers are rotated by 90° compared to the 0° case. This reduction results in a smaller Bragg-BG and the destructive interaction of the LR-BG with the Bragg-BG. This illustrates how important it is to correctly localize the aperture of local resonators with respect to the incident noise. In addition, from 2.85 kHz to 3.7 kHz, the 0° SCNB produces similar levels of insulation compared with the CB with two peaks of maximums in the IL at approximately 3.5 kHz.

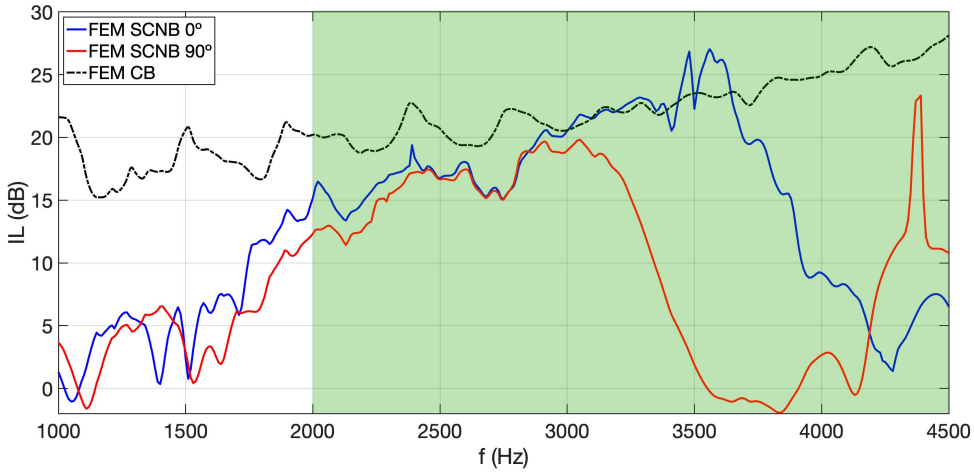

Figure 6.13: Insertion Loss of Numerical FEM Models with 0° SCNB (blue), 90° SCNB (red) and CB (black).

To gain a deeper insight into the noise control mechanisms that influence both 0° SCNB and 90° SCNB, the band structure is calculated with FEM simulation. With a unit-cell model we compute the dispersion curves diagram and BG structure of two configurations of scatterers. We utilized the conventional representation using wave-vectors, where directions ΓX corresponds to specific pairs of (k_x, k_y) values, namely (0, 0), $(\pi/a, 0)$, and $(\pi/a, \pi/a)$, where kx and ky represent the wavenumbers in the two orthogonal directions of an infinite periodic structure with a lattice constant (a).

In Fig. 6.14, 0° SCNB and 90° SCNB configurations have two complete band gaps (grey colour). The first one is related to Bragg-BG centred in 3.1 kHz, and the second one is related to the LR-BG, located in 4.37 kHz.

Examining the BG structures, computed for both 0° SCNB and 90° SCNB, significant differences in the BG structure are observed. Specifically, the analysis of 0° SCNB reveals the increase of the pseudo-gap around 3.1 kHz in ΓX (blue colour). For the propagation directions of interest in our experimental measurements and simulations, the relevant part of this band gap structure is between the directions ΓX.

In the case of 0° SCNB, a pseudo-band gap is observed between 1.54 kHz and 4.28 kHz, corresponding to the target frequency range of TBN, while for 90° SCNB, it occurs between 1.73 kHz and 3.47 kHz not covering the full range of interest.

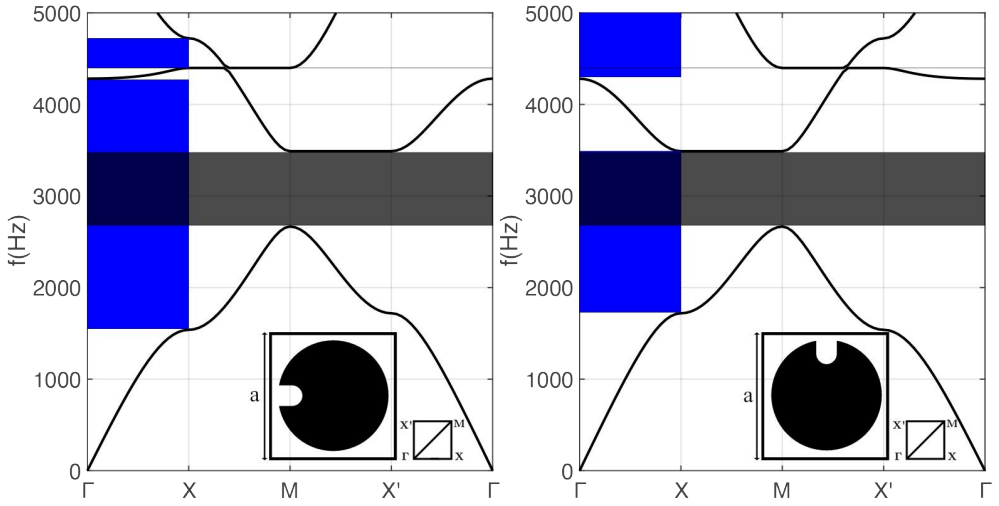

Figure 6.14: Band structure diagrams for 0° SCNB (left), 90° SCNB (right) both including the unit cell of the two-dimensional scatterer with LR, which forms the periodic system defining the SCNB and irreducible Brillouin zone of the square lattice SC based on the Bloch-Floquet theory for the calculation of the band structure.

Experimental

In this section, the results of the experimental measurements are analysed and the two different configurations of SCNB at 0° and 90° are compared. Fig. 6.15 shows a significant difference between the configurations in the lower frequency range (1 to 1.8 kHz) , while the CB reaches levels of IL around 15 dB, and in the 0° and 90° cases, peaks about 6 and 9 dB are obtained respectively. Nevertheless, almost in the same frequency range as the numerical result, from 2.85 kHz to 4.0 kHz, some peaks with better

insulation levels are found in the experimental measurement with 0° SCNB compared to the CB measurement. At some frequencies, such as 3.95 kHz, approx. 7 dB peaks higher insulation values are measured in the 0° SCNB case compared to the rigid barrier. This value is also observed in the numerical simulation, but with a small frequency shift. When comparing the experimental cases, it is important to consider that the maximum levels reached with the CB are the goal to achieve in the target frequency range of TBN. Due to small 3D printing defects in the small local resonator cavity, the dimensions were slightly different from model to prototype. A shift to higher frequencies can be observed throughout the frequency range, from lowest frequency of interest to the highest peaks in the 3.5 -4.0 kHz range [132]. A remarkable increase in IL is measured in the frequency range from 3.0 to 4.5 kHz, with an insulation value around 15 dB. Due to the already mentioned frequency shift and the effect of viscothermal losses (see3.3), it is possible that the decrease is actually smoother and less abrupt.

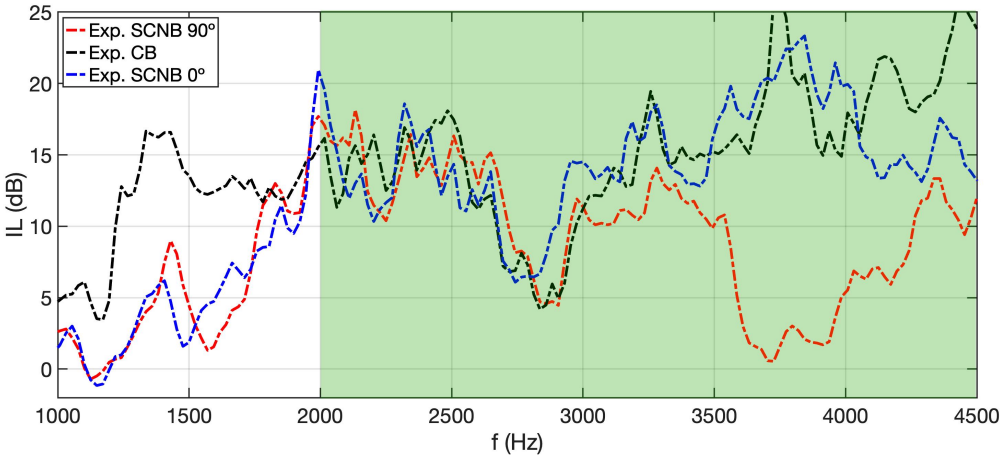

Figure 6.15: Insertion Loss of the experimental measurements, with 0° SCNB Experimental (blue dashed-dotted), 90° SCNB Experimental (red dash-dotted) and experimental CB (black dot-dashed).

From 2.85 kHz to 4.0 kHz, the insulation performance in the case of the 0° SCNB exceeds the CB, but with the 90° SCNB only poorer IL results are achieved due to the 90° rotation of all scatterers. In fact, from 2.85 to 4.5 kHz, the 90° SCNB measurement is always lower than the 0° SCNB case, resulting in a reduction of the main Bragg-BG and thus of the target frequency range where the TBN may be most annoying.

6.4 Conclusions

This chapter introduces the issue of noise pollution, particularly that posed by TBN in the 2 to 4.5 kHz range. The most annoying frequencies of TBN are mitigated by the introduction of SCNBs, which strategically attenuate noise within certain frequency ranges, offering a promising solution for this type of noise. More specifically, large dif-ferences were observed in numerical simulations (20 dB) and in the experimental results (25 dB) between the 0° SCNB and the 90° SCNB in the TBN frequency range.

The present research explores the integration of LRs and their interaction with Bragg scattering in resonant SCNBs, emphasizing the crucial role of resonator orientation. Advanced numerical simulations, employing FEM, assess the acoustic efficacy of 2D SCNB models, while experimental validation using 3D-printed prototypes confirms their competitive noise reduction levels compared to conventional barriers.

The appropriate configuration of the SCNBs, particularly the orientation of the resonant cavity, proves to be crucial for effective noise reduction, especially when the local resonators are oriented at 0°. Our study designed for to the specific frequency range of TBN, from 2 kHz to 4.5 kHz, focusing on this spectrum allows for in-depth analysis and targeted solutions for TBN mitigation.

Beyond the performances, another advantage of the proposed methodological approach concerns the use of a parametrized model to support the adjustment of the barrier geometries to select specific noise control frequency insulation ranges. If compared with the proposed approach, previous research was less easy to customise and usually there was a single design for an unique noise target case. Indeed, the innovative parametric modelling helps to easily 3D-print acoustic metamaterials and, more specifically, SCNB, which have complex and customised shapes that can change a lot depending on the noise frequencies that the barrier must insulate. This useful design tool brings closer the application of this metamaterial barrier to real applications. In addition, based on the intensity of the noise to be reduced, the barrier can be improved by including any number of rows to increase the insulation by maintaining wind and light permeability (as shown by simulation and experimental tests). To sum up, the flexibility and adaptability of the proposed procedure allow the application of the proposed barriers in different contexts.

Additionally, we highlight the potential for scalability of our findings, with a note that large-scale applications should consider the role of viscothermal losses. This opens avenues for future research, allowing for the

exploration of our model's adaptability and its impact across various scales and contexts. The study opens up new avenues for future investigations in noise reduction and SCNBs. Potential future research areas include exploring scalability to diverse transportation environments, optimizing SCNB materials and resonator designs, integrating smart technologies for active noise mitigation, and assessing long-term durability and maintenance requirements.

Part IV

Multiresonant Scatterers in Sonic Crystal Transmission Applications

7 Increasing the Insertion Loss of Sonic Crystal Noise Barriers with Multiple Helmholtz Resonators

7.1 Introduction

A major problem in today's industrialized world is noise and its effects on people's health. Various solutions have been proposed to solve this problem using noise reduction techniques, which are applied at three different stages: near the source, at the transmission and at the receiver. The most common solution, and the most widely used because of its simplicity, is the use of devices at the transmission level or, more precisely, the installation of Noise Barriers (NB) between the source and the receiver [21]. The insulation performance of NB can be improved by a suitable choice of shape; the geometry of the edge or the curvature of the main flat surface to modify the diffraction of the upper part [133]. Incorporating porous materials into the NB also helps to improve their acoustic performance, especially with regard to the reflection of sound waves between the source and body of the NB [99].

In this field, a new method has emerged in the last decades, which has new properties in contrast to conventional flat walls for noise reduction: Sonic Crystal Noise Barriers (SCNB) [134, 16, 28, 27]. SCNBs consist of periodic materials called sonic crystals, which are arrays of scatterers embedded in air [11]. While conventional barriers do not allow air or water to pass through, SCNBs are permeable to fluids. Moreover, they can be arranged to attenuate noise in specific target frequency ranges, which is one of the advantages over conventional barriers that cannot distinguish between different noises. SCNGs exhibit the property of Bragg bandgaps (Bragg-BGs), with frequency ranges for which acoustic waves are not al-

lowed to propagate due to the interference generated by the multiple scattering of waves [11, 135, 24]. The central frequency of the first Bragg- BGs is $f_c = c/2a$, where c is the speed of sound in the fluid [m/s] and the lattice constant (a), which is the distance between scatterers and is characteristic of the unit cell of a crystal lattice [8]. Bragg-BGs have improved the ability to control wave propagation through many additional applications such as waveguides [17] or diffusers[15]. Some approaches have been developed to improve the insulation level and range of Bragg-BGs, e.g. by using fractal geometries [136] or different radius of the scatterers that make up the SCs [137].

In addition to Bragg scattering, BGs are also produced by local resonances. In particular, they are used to induce low-frequency BGs in SCs and have been studied in one- and two-dimensional periodic arrays based on local resonance [114, 138, 139, 140]. In acoustic systems, these resonances are usually generated by Helmholtz Resonators (HRs) [2]. The BGs based on local resonances of HRs (HR-BGs) depend on the alignment of the mouth of the resonator with respect to the incident sound wave. Some studies have shown that an opposite arrangement of the HRs mouths can help to achieve sound insulation and air ventilation simultaneously [71] and that the maximum of the absorption coefficient is extremely angle dependent [112]. The HR-BG has a smaller frequency range than the Bragg-BG, but several authors have proposed to extend the BGs of SCs by multiresonant scatterers [141, 142, 34, 31, 52]. HR-BG and Bragg-BG influence each other [115, 117] and sometimes the interaction between the two wave propagation phenomena does not improve the insulation capacity of the SCNB [118]. As far as we know, there are no studies on the effect of this interaction on the transmission of a SCNB and on the specific influence of the resonator on the Bragg-BG. The main purpose of this chapter is to study the effect of the interaction between the local resonance and the Bragg interference in order to increase the noise insulation produced by SCNBs.

7.2 Methodology

The development and validation of innovative solutions for noise reduction usually requires an enormous amount of time, specific laboratory resources and high costs with little scope for change until a new prototype is manufactured. To circumvent these drawbacks, the scientific community has developed and validated several numerical algorithms to evaluate the acoustic performance of new devices, as it is crucial to accurately predict their acoustic properties even before they are designed. These simulation techniques have contributed to the advancement of acoustic technology, especially to the development of novel periodic materials, such as SCs. These numerical simulation techniques, in combination with optimization strategies, are efficient design tools as they allow the development of devices with improved acoustic performance and new features [143, 144, 145].

The periodicity and symmetries of SCs allow to simplify the calculation of the model and to achieve an approximation to the real case of long domains with high accuracy, e.g. the evaluation of the insulation solution for an extended path such as highways or railways. In recent years, a variety of simulation methods have been used to evaluate the effectiveness of periodic structures in acoustics. In the present chapter, domain-discretised techniques such the previously explained FEM and FDTD techniques are used for numerical simulations.

Numerical Model

We consider a two-dimensional SC, which consists of a set of HRs distributed in an infinite square periodic lattice. Figure 7.1 a) shows the unit cell of the two-dimensional periodic system under investigation, which is defined by a scatterer with the outer radius (R) and a HR inside. Periodic boundary conditions are set at the (X) and (Y) boundaries so that the infinitely extended SC is defined by a periodic structure with a square lattice and constant lattice (a), and the irreducible Brillouin zone in the reciprocal space [6] . The resonator is characterized by the length of the neck L, the width of the mouth w, the inner surface area ($S = \pi r^2$), where r is the inner radius of the surface of the HR. The first resonance frequency of the resonator is given by Equation 2.12.

The band structure is performed in two different directions in reciprocal space based on the Bloch-Floquet theory [4, 5]: 0° (ΓX) and 90° ($\Gamma X'$) Numerical simulations using the FDTD method are performed to evaluate the transmission of two SCNBs with a design based on the unit cell de-

fined in Figure 7.1a). Periodic Boundary Conditions (PBC) are considered to reproduce an infinite SC in the Y-direction but truncated to three layers of scatterers in the X-direction (see Fig. 7.1b and 7.1c) [146]. In the two transmission models, both the distance between the scatterers and the transversal dimension of the models are ($a = 0.17$ m), with a filling fraction ($ff = \pi \left(\frac{r}{a}\right)^2 = 0.4$). Thus, the geometric model of the SCNBs and the unit cell have the same topology, namely a two-dimensional square-periodic structure. An incident plane wave with frequency (f) and acoustic pressure (P_i) propagates along the (X)-axis from left to right in such a way that it is aligned with the mouth of the HR in Fig. 7.1b and perpendicular to it in Fig. 7.1 c (hereafter referred to as the 0° and 90° alignments). 'Perfectly Matched Layers' (PMLs) [50] are applied to both (X)-axis boundaries of the models to absorb waves propagating outward from the domain.

The transmission of the system is analysed in the evaluation points of aline at a distance of 1 meter from the SC by evaluating the transmission coefficient (τ) defined by:

$$\tau = \frac{\langle P_t^2 \rangle}{\langle P_i^2 \rangle}, \tag{7.1}$$

where $< >$ stands for the averaging of both, the squared incident acoustic pressure (P_i) and the squared transmitted acoustic pressure (P_t) at the evaluation points. From τ the equation for the Insertion Loss (IL) in decibels can be derived as follows:

$$\text{IL} = -10 * \log_{10}(\tau), \ [\text{dB}] \tag{7.2}$$

and indicates how the sound pressure level at the evaluation points changes when the SCNB is positioned in the acoustic path of the incident wave.

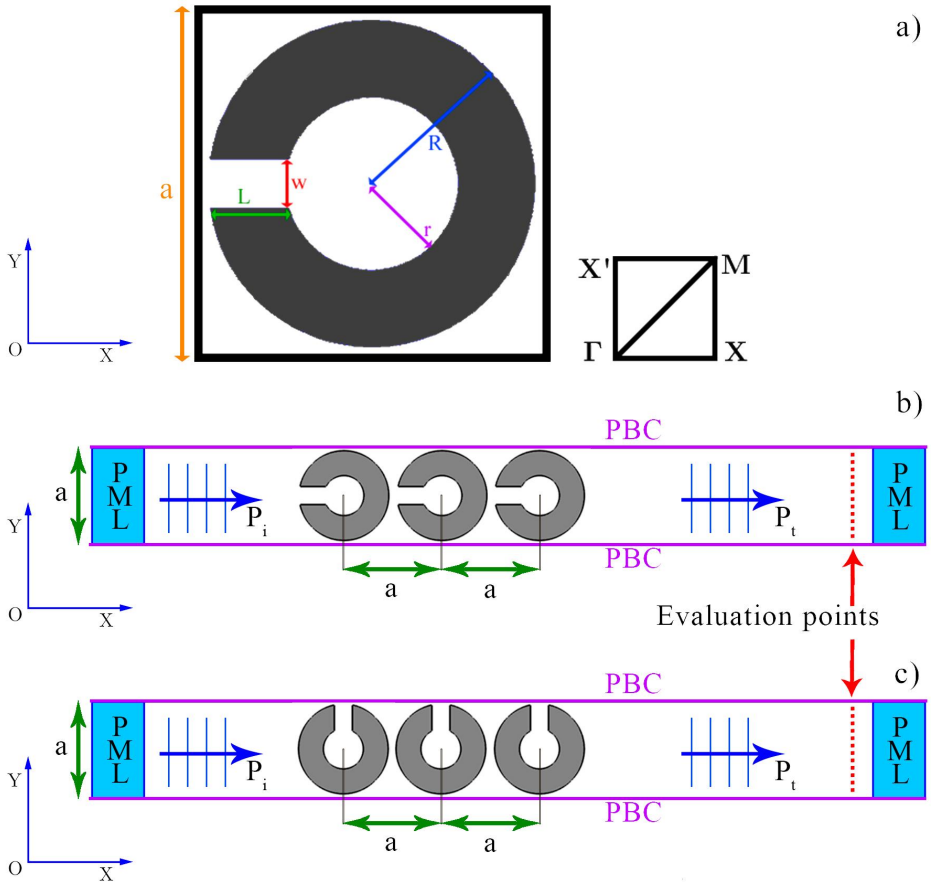

Figure 7.1: a) Unit cell of the two-dimensional scatterer with HR, which forms the periodic system defining the SC and irreducible Brillouin zone of the square lattice SC based on the Bloch-Floquet theory for the calculation of the band structure. Numerical models for the SCNBs with 3-row scatterers for the evaluation of the IL with b) 0^{o} aligned and c) 90^{o} aligned HRs.

7.3 Bragg and Helmholtz resonances interaction

The effect of multiple scattering interference significantly reduces the transmission of a SCNB in the BGs and increases its insulation. In general, this phenomenon applies not only to the Bragg-BG, but also to the HR-BG [138] In the model proposed here, the scatterers have a local resonator. Depending on the central frequencies and the width of their BGs, both Bragg-BG and HR-BG can overlap, leading to a different type of interaction between the phenomena [117, 118, 147].

Next, the transmission of an incident plane wave from a SCNB is investigated numerically using the models shown in Fig. 7.1 b for the 0° alignment and Fig. 7.1 c for the 90° alignment. The aim is to analyse the physical interaction between the first Bragg resonance and the first local resonance and their mutual interaction. The value of the specific central frequency of the HR-BG influences the width and the insulation of the Bragg-BG. Two SCNBs are studied with their HR-BG below and above the Bragg-BG with a fixed lattice constant ($a = 0.17$ m), i.e. a central Bragg frequency of $f_c = 1000$ Hz. According to 2.12, the HR resonance frequency depends on the neck, the mouth and the volume of the resonator. The resonant frequency of the HR could be changed by suitably varying each of these parameters according to (2.12). However, due to geometric constraints in the design of the resonator inside the scatterer, it is appropriate to vary the surface of the resonator to cover a wide range of HR resonant frequencies with realistic geometries. Fig. 7.2 shows results of FDTD simulations of the transmission coefficient of a SCNB in a solid line based on the models shown in Fig. 7.1b) and 7.1c) together with the band structure of the SC with circles with 0° alignment in red and 90° alignment in blue for ΓX and ΓX', respectively. For reference, the SCNB is shown with closed cylinders, SCNB-CC, i.e. without local resonance, in black. The scatterers of the SCNB have a HR with a mouth of width $w = 1$ cm, a neck of length $L = 1$ cm and an inner radius $r = 4.5$ cm corresponding to a resonant frequency $f_{\mathrm{HR}} = 400$ Hz $< f_c$. The frequency range includes the first Bragg-BG with the central frequency f_c and the first HR-BG, with resonance frequency fHR. Both phenomena have higher resonances, but they are far from interacting with the first resonances and their mutual interactions are beyond the scope of this work.

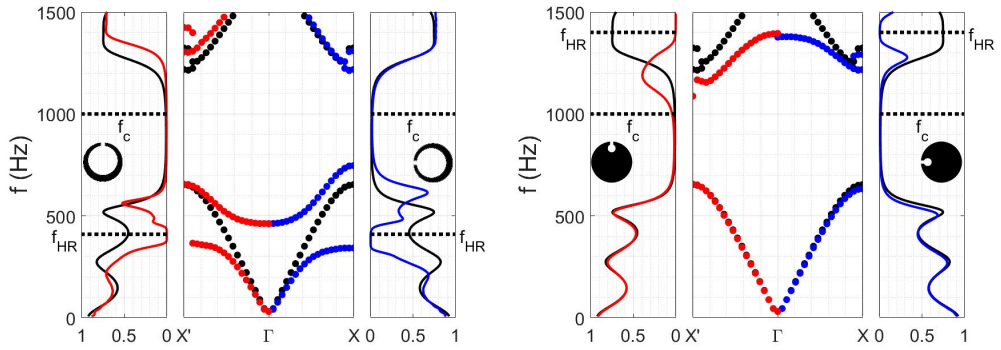

Figure 7.2: Transmission coefficient of the SCNB and band structure of the corresponding SC with **(left)** $f_{\mathrm{HR}} < f_c$ and **(right)** $f_{\mathrm{HR}} < f_c$ of the configurations with 0° alignment(blue) and 90° alignment (red). The SCNB-CC case is plotted in black for reference

Although the band structure was obtained from an infinite periodic SC and the transmission loss from the SCNB with an array of three layers of resonators, the agreement between the presence of BGs and transmission minima is significant. Figure 7.2-left shows the case of a HR with a small surface and, thus, a resonant frequency lower than the central frequency of the Bragg-BG ($f_{\mathrm{HR}} < fc$). At low frequencies, below and around the local resonance, oscillations are observed in the transmission, which are due to Fabry-Perot interference phenomena [81] due to the multiple reflections of the waves at the truncated ends of the SC. This is thus a phenomenon caused by the finite length of the crystal and cannot be explained by the band structure of the infinite SC. The interaction between the two BGs is visible in the frequency range of the HR-BG below the Bragg-BG, where the greatest difference from the case of the SCNB-CC is observed. A significant reduction in transmission is observed for both 0° alignment and 90° alignment due to the local resonance. Fig. 7.2-right shows the case where the resonance frequency of the HR has been tuned above the Bragg-BG (higher surface). The scatterers of the SCNB have a HR with a mouth of width $w = 1$ cm, a neck of length $L = 1$ cm and an inner radius $r = 1.2$ cm corresponding to a resonant frequency $f_{\mathrm{HR}} = 1400$ Hz $> f_c$. Again, the reduction of the transmission coefficient can be observed in the frequency range where the local resonance and the Bragg resonance interact.

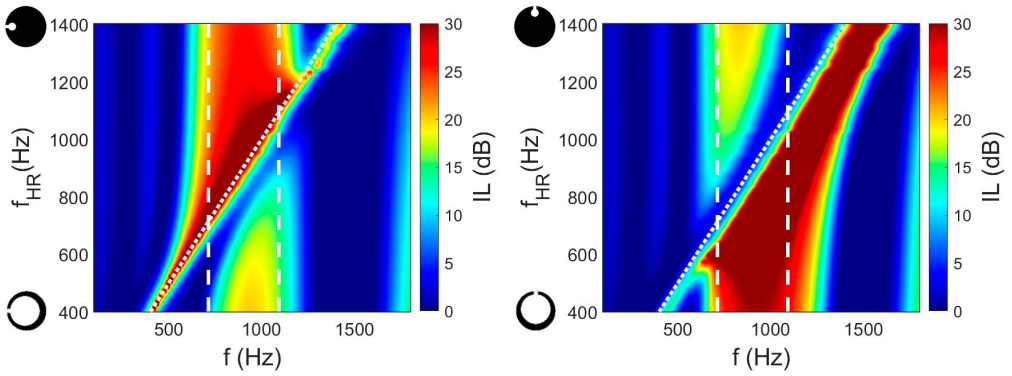

Figure 7.3: Insertion Loss of SCNB with varying HR resonant frequency for the configuration with **left**) 0° alignment and **right**) 90° alignment. The dashed vertical lines represent the lower and upper Bragg-BG limits of the SCNB-CC. The value of the theoretical resonant frequency of the HR is rep-resented by the white dotted line.

Figure 7.3 shows the numerical results of IL for several SCNBs consisting of arrays of HRs tuned to $f_c = 1000$ Hz ($a = 0.17$ m) in a colour scale. Each sub-figure contains the results of IL for 60 numerical simulations of arrays of HRs with different resonant frequencies. The resonant frequency of the HR is plotted on the Y-axis and the frequency of the propagating waves on the X-axis. For illustration, the lower and upper limits of the Bragg-BG of the SCNB-CC are drawn with vertical white dashed lines at $f = 713$ Hz and $f = 1092$ Hz, respectively (criterion IL = 18 dB). Since the phenomenon of local resonance does not occur in an SCNB-CC, the IL is identical for all SCNBs along the entire Y-axis. The white dotted line corresponds to the value of the theoretical resonance frequency of the HR, calculated from (2.12). Fig. 7.3-left shows the case of the SCNB with 0° alignment. The IL depends strongly on the resonance frequency of the HRs. The nature of the interaction between Bragg-BG and HR-BG is determined by their relative frequency resonances. When f_{HR} is far from f_c($f_{\mathrm{HR}} < 600$ Hz and $f_{\mathrm{HR}} > 1200$ Hz), both resonances are well separated. When the resonances are closed (600 Hz $< f_{\mathrm{HR}} <$ 1200 Hz), the interaction is significant and important changes in the IL are observed with respect SCNB-CC. The IL has an asymmetric shape because the transmission is much higher at frequencies $f < f_{\mathrm{HR}}$ than at frequencies $f > f_{\mathrm{HR}}$. For example, at $f_{\mathrm{HR}} =$ 1400 Hz, the Bragg-BG is similar to that of the SCNB-CC at the same frequency, which agrees quite well with the white vertical dashed lines. The interaction between the resonances of the IL of the SCNB with 90° alignment is shown in Fig. 7.3-right. It is also asymmetric with respect to the local

resonant frequency, but the insulation increase occurs at frequencies below the Bragg frequency. The increase of IL due to the interaction between the Bragg resonance and the local resonance thus strongly depends on the specific orientation of the HRs of the SCNB with respect to the incident plane wave.

Figure 7.4 shows the IL as a function of frequency for specific cases with $f_{\mathrm{HR}} = 400$ Hz ($f_{\mathrm{HR}} < f_c$) and $f_{\mathrm{HR}} = 1400$ Hz ($f_{\mathrm{HR}} > f_c$) in red and blue respectively. Figure 7.4-left shows the 0° alignment. The SCNB-CC is shown in dashed black. The coloured area visually shows the change of the IL of the SCNB with HRs with respect to the SCNB-CC. It can be observed that in the case where fHR is above the Bragg-BG, the IL increases compared to the SCNB-CC. If the resonance frequency is below, the opposite is true: the insulation of the SCNB decreases. Instead, the IL decreases compared to the SCNB-CC when the fHR is above the Bragg-BG, as can be seen in Fig. 7.4-right for a 90° alignment. The IL of the SCNB, on the other hand, increases when the resonance is below. The above results prove that the orientation of the HR mouth in a SCNB is directly related to its insulating properties. Moreover, the resonant frequency of the resonator can be tuned to increase the IL of the SCNB at the Bragg-BG by choosing the alignment of the HRs accordingly. It should be noted that the coexistence of Bragg resonances and HR resonances not only leads to an increase or decrease of IL at the Bragg-BG, but also to a frequency shift of fc. This is due to the phase shift produced by the HR, which can be explained by a change in the lattice constant experienced by that the wave during propagation [118].

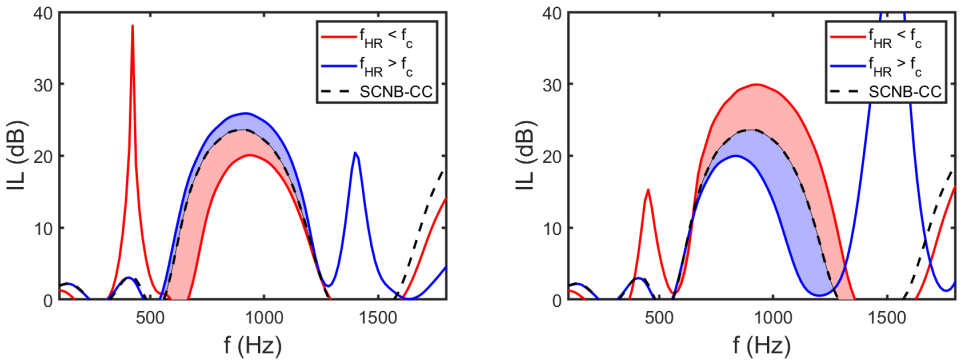

Figure 7.4: Insertion loss as a function of frequency of SCNBs with $f_{\mathrm{HR}} < f_c$ (red) and $f_{\mathrm{HR}} > f_c$ (blue) with **left**) 0° alignment and **right**) 90° alignment. The coloured area graphically represents the variance of the IL of the SCNB with HRs with respect to the SCNB-CC (dashed black).

7.4 SCNB scatterer with two HRs

As a result of the interaction between the Bragg resonance and the local resonances, the increase in insulation of the SCNB depends strongly on the alignment of the mouth of the HR. The relative value of the local resonance (f_{HR}) with respect to the central frequency of the Bragg bandgap (f_c) is an important factor as it determines the interaction between the two phenomena. The use of resonators in SCNBs does not necessarily increase their sound insulation. Therefore, careful attention should be paid to the alignment of the mouths and the resonant frequencies of the HRs in the scatterers of SCNBs. Figure 7.5 shows a scatterer for a SCNB consisting of two HR aligned at 0° and 90°, with variable and coupled surfaces. The inner moving wall can be rotated by an angle θ, and simultaneously changes the resonances of the two HRs. Both HR have identical mouths with size $w = 3$ cm. and length $L = 1.5$ cm. As in Section 3 of this chapter, IL is computed numerically in a SCNB consisting of scatterers arranged in a two-dimensional square lattice with a filling fraction $ff = 0.4$ and the central frequency of the Bragg-BG is $f_c = 1000$ Hz.

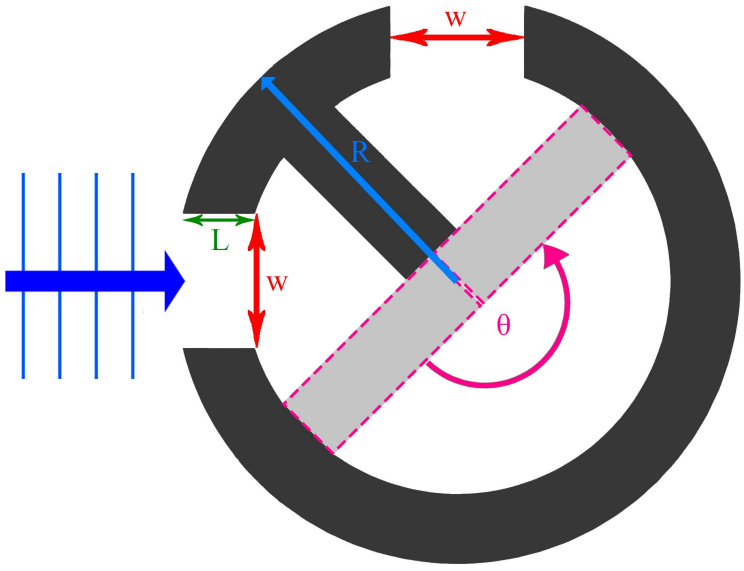

Figure 7.5: Cylindrical scatterer consisting of two HRs with identical mouth and variable coupled surfaces through a rotating inner wall.

Figure 7.6 shows the behaviour of a SCNB with cylinders with two HRs and the influence of the change in change due to the movement of the inner

moving wall. Figure 7.6-left shows the IL in colour scale for the SCNB with scatterers with coupled HRs as a function of the rotation angle θ of the wall analysed with the same numerical model as in Fig. 7.1b and Fig. 7.1c. The change in SCNB insulation behaviour results from θ-driven surfaces changes in the HRs. Thus, if the HR with 0° alignment has a smaller surface (θ= 0°), the HR with 90° alignment has the largest surface and the IL in the BG -Bragg is high. However, the surfaces ratio of the HRs is changed, IL varies. When the surfaces of the HRs are inverted (θ= 180°), the IL in the BG-Bragg decreases drastically and only the resonances of the respective HRs are observed. HRs do not behave the same with identical surfaces due to the uneven alignment of their mouths in relation to the incident wave. This asymmetry favours the increase of the insulation of the structure when frequencies of the HRs are properly tuned for each alignment.

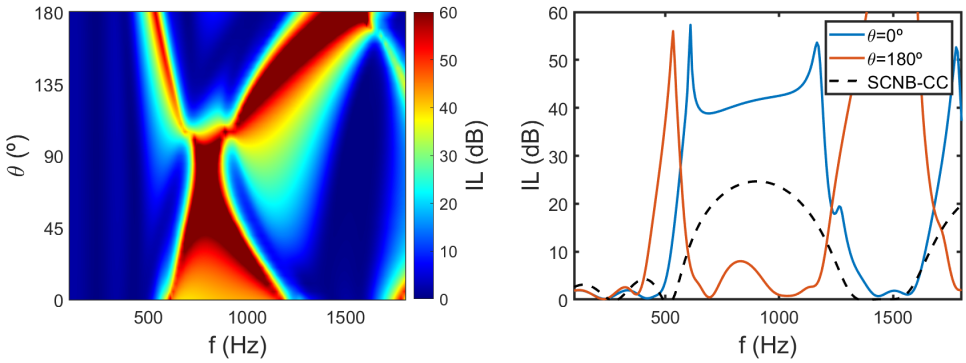

Figure 7.6: Insertion loss in colour scale as a function of frequency for SCNB with scatterers with coupled-surface HRs as a function of the inner wall rotation angle. (Right) Cases $\theta = 0°$ and $\theta = 180°$ and SCNB-CC..

Figure 7.6-right shows the IL as a function of frequency for the cases θ= 0°, θ= 180° and the SCNB-CC. As seen in section 3 of this chapter, the IL of SCNB at the Bragg-BG increases in 0° alignment for $f_{\mathrm{HR}} < f_c$ and decreases in 90° alignment for $f_{\mathrm{HR}} > f_c$. This condition is fulfilled for both coupled-surface HRs when θ= 0°. In this case, the surface of the HR with 0° alignment is actually minimum and the surface of the 90° alignment is maximum. It can be seen that the frequency range corresponding to the Bragg-BG (between 500 Hz and 1300 Hz), the IL increases by about 20 dB compared to the SCNB-CC due to the interaction between Bragg and local resonances. The central frequencies of HR-BG of both HRs appear as local maxima in the IL at $f = 610$ Hz and $f = 1165$ Hz for the HR aligned at 90°. When the inner wall is rotated to $\theta = 180°$, the surfaces of the HRs are reversed and the acoustic behaviour of the SCNB changes drastically. The

IL of the Bragg-BG changes by more than 30 dB when the wall is rotated from $\theta = 0°$ to $\theta = 180°$ and the resonance frequencies now shift to $f = 534$ Hz and $f = 1520$ Hz. Although both configurations are geometrically equivalent because their HRs have identical surfaces, the central frequencies of the HR resonances are different because of the different alignment of the cylinders with respect to the incident wave.

As Figure 7.6-right shows, the IL reaches SPL = 40 dB in the Bragg-BG frequency range. In [141], the combination of concentric closed-cylinders and cylinders with HR gives numerical and experimental results with less than 20 dB in the Bragg-BG frequency range. Several settings of HRs scatterers have been tested numerically and experimentally in [140], including porous materials inside the cylinder, but none of the combinations brought more than 25 dB in the whole Bragg-BG frequency range. Thus, our proposal of a barrier with resonators tuned at the edges of Bragg-BG offers a very significant increase in IL compared to other proposals in the literature.

Since SC is not an isotropic material, the acoustic behavior of SCNB with other incidences may be considered. This approach is made considering that the noise source is far away enough, so when source is closer, it would be interesting analyze how the SCNB performs. Instead of rotating the separator of the two HR cavities, rotate the whole cylinder can be also a good choice. By doing this, each scatter will have two different degrees of freedom. Implementing automatic control according to different stimulus could also be an extremely complex and versatile system, with the adaptative ability to perform several cases. Another interesting prospect to study would be now explore periodical configu-rations and see how the resonant scatterer performs.

7.5 Conclusions

The insulation of noise barriers based on sonic crystals with HRs is analysed for different configurations and orientations with respect to the incident wave. The interaction between local resonance and Bragg interference phenomena and the alignment of the mouth with respect to the incident wave is crucial for the design of SCNB with high insulation capacity. When the orientation of the HR aligns with the incident acoustic wave, the transmission of the barrier is reduced if the local resonant frequency is lower than the Bragg bandgap. IL also becomes higher when it is perpendicular to the incident wave and the local resonant frequency is higher than the Bragg bandgap. Based on this mechanism, a cylindrical scatterer composed by two HRs is proposed, which increases the Insertion Loss of a SCNB by up to 20 dB compared to a noise barrier made of closed cylinders.

7.6 Appendix: Viscothermal Losses

This section explains why viscothermal losses do not necessarily need to be considered in the numerical simulations presented in some chapters of this thesis. To this end, a model of viscothermal losses is presented and verified by numerical simulations that its acoustic effects are negligible compared to an equivalent lossless system.

The whole explanation of the theoretical background employed to analyse the viscothermal losses in the necks of the resonants scatterers have been explained in chapter 3.3.

So according to 3.15 and 3.16 , the viscous and thermal layers have a greater width for long wavelengths[131]. Therefore, if their influence is negligible at low frequencies, this will also be the case at higher frequencies. For this reason, only the case where HR is tuned to low frequency is considered here to prove that viscoelastic losses can be neglected in this work. Figure 7.7, shows two scatterers with embedded HR. Figure A1-left shows the HR used on the work with a neck of $w = 1$ cm and $L = 1$cm, called HR1 and Fig. 7.7-right, the HR2 with the same theoretical resonance frequency $f_{\mathrm{HR}} = 400$ Hz, the same length of the neck $L = 1$ cm and consequently a thinner mouth ($w = 0.2$ cm).

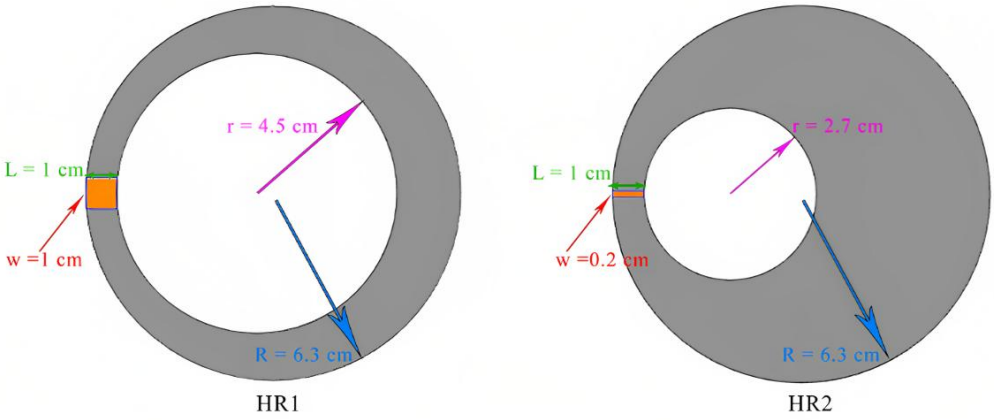

Figure 7.7: **Left**: Scatterer with HR with wider mouth ($w = 1$ cm) and. **Right**: Scatterer with HR with narrower mouth ($w = 1$ cm). HR1 and HR2 have the same resonance frequency $f_{\mathrm{HR}} = 400$ Hz

The IL of two 3-row SCNBs with both HR1 and HR2 are calculated numerically using the model presented in previous sections. It is shown that the viscothermal losses for the HR studied in this work can be neglected in the working frequency range. Figure 7.8 illustrates the IL in the frequencies

of the HR-BG. Since the mouth of the resonator is quite large, no significant viscothermal losses occur in the neck of HR1.

However, when the size of the mouth is reduced, the losses are no longer negligible and the acoustic properties of the SCNB change significantly. For HR2, the peak of the resonance shifts from 400 Hz to 378 Hz when viscothermal losses are taken into account. Since the acoustic model used in this work is not scalable, the results shown in this section onlyapply to geometries where the viscothermal losses are negligible.

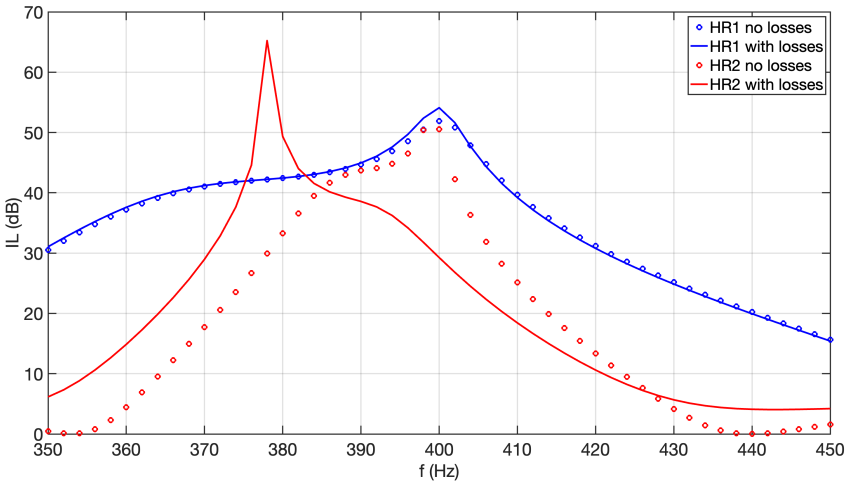

Figure 7.8: Insertion Loss of a SCNB with HR1, used in the paper (blue) and with HR2, with a thin mouth (red) with (continuous) and without (circles) losses

8 Acoustic Switch based on Rotatable Sonic Crystal with Multiresonant Scatterers

8.1 Introduction

In the previous chapter, it has been deeply explained that in SC, Bragg Bandgaps (Bragg-BGs) can be smartly combined with other noise control mechanisms in the scatterers. Due to Helmholtz Resonators (HRs) forbidden frequency bands are also produced [114], in addition to those produced by Bragg Band Gaps.

Most phononic and acoustic metamaterial designs so far exhibit a non-adaptative response and function within fixed frequency ranges, which restricts their potential applications [148]. To create tunable and switchable systems, research has demonstrated that Bragg-type band gaps can be adjusted through pattern transformations induced by instability. In the literature, there are examples of asymmetric scatterers in phononic crystals (with water as host medium) where exploring different angles independently for each scatterer in the periodic structure can yield multiple applications with a single device, one of them resulting into a switch in the high frequency regime [149].

This chapter explores the possibility of tuning the HRs-BGs based on two perpendicular positions of the multiresonant SC, creating a device capable of filtering certain frequencies, allowing others to pass through, and switching this filtering by rotating all its scatterers 90^{o}.In low frequency regime, this switchable device need for a rotatable mechanical modification in all of the scatterers like recent works have also exploited to obtain insulation chambers with HRs in higher frequencies [150, 151].

Recently, also topological metamaterials have been used to develop a phononic switch that can transition between a topological waveguide and a trivial insulator through mechanical compression[152, 153]. Both works

obtaining about 20 dB in the desired high frequency range. However, many of these designs are complex or require precise control of external conditions. Thus, there is a need for a straightforward and efficient method to design an acoustic switch.

By undertanding the phenomena behind HR-BGs and Bragg-BGs interaction, their frequency ranges of interaction and the mouth orientation with respect the incident wave, a simple design was developed in the previous chapter in ordrer to improve the IL of a SCNB . With two different HRs, both with the same mouth width but wisely dividing the inner volume of the scatterer, the multiresonant scatterer was a cylinder with an angled separation wall. After conducting a thorough analysis of the phenomena ilustrated in Figure 7.6, an appropriate behaviour for a switch device in transmission could already be observed. Therefore, while maintaining some of the structure's variables, it was decided to modify the internal wall that separates the HRs of the multiresonant scatterer and the width of their mouths.

This chapter focus on the transmission of an incident plane wave and the computation of the band structure for both perpendicular positions of the multiresonant scatterers, numerically and experimentally. The objective is to analyze the Bandgaps (BGs) that emerge at opposite orientations and how they complement each other in terms of frequency for the cases under investigation. The central frequency value (f_{HR}) of the Helmholtz Resonators-based Bandgaps (HRs-BGs) plays a pivotal role in influencing the width and transmission level of the Bragg-BG.

8.2 Methodology

For the sake of brevity, and given that the numerical models are the same as in the previous chapter 7, the methodology will focus on explaining in detail the chosen optimization algorithm, the variables, objective functions, and the entire process for obtaining a multiresonant SC with properties of a tunable switch for transmission through it.

Furthermore, the constancy of the lattice constant (a) in both the Bragg-BG and HRs-BGs cases underscores the significance of the HR alignment as a key tuning parameter. This alignment, intricately linked to the transmission properties, emerges as a critical factor in optimizing the acoustic performance of the multiresonant SC. The subsequent sections delve into a detailed analysis of the optimization process, exploring the nuanced interactions and providing a comprehensive understanding of the mechanisms governing the interaction between Bragg scattering and Helmholtz resonances in SC.

Optimization procedure

In this section, we provide a brief overview of the evolutionary algorithm used in this study. A Multiobjective (MO) approach is employed to obtain solutions that simultaneously satisfy multiple objectives. When dealing with several objectives, improving one may result in the deterioration of others, implying the absence of a single optimal solution. The standard method for addressing this issue is to identify the set of optimal solutions, known as the Pareto set, which is then represented in the objective space as the Pareto front. The final step in Multiobjective optimization involves selecting one of these optimal solutions based on the designer's preferences.

A general multi-objective problem can be expressed as:

$$minJ(\vec{x}) = min[J_1(\vec{x}), J_2(\vec{x}), \ldots, J_M(\vec{x})], \tag{8.1}$$

subject to $\vec{x} \in S$

Where $\vec{x}$ is the vector of the decision variables to modify during the optimization, $J : A \to \mathbb{R}^M$ is the objective function vector, M is the number of objectives, A is the decision variable space, and $S \subseteq A$ is the feasible solution space. The basic concept to obtain the Pareto set is known as Pareto dominance and it is defined as follows: a solution $\vec{x}_1$ dominates another solution $\vec{x}_2$, denoted by $\vec{x}_1 \prec \vec{x}_2$, if $\forall i \in \{1, \ldots, M\}, J_i(\vec{x}_1) \leq J_i(\vec{x}_2)$ and $\exists k \in \{1, \ldots, M\} : J_k(\vec{x}_1) < J_k(\vec{x}_2)$.

The Pareto optimal set is defined as:

$$P = \{\vec{x} \mid \vec{x} \in S, \nexists \vec{x}' \text{ such that } \vec{x}' \prec \vec{x}\}$$

And for each $\vec{x} \in P$, there corresponds a nondominated vector in objective space which together form what is called the Pareto front:

$$PF = \{J(\vec{x}) \mid \vec{x} \in P\}$$

The Pareto set P is composed of all the non-dominated solutions, and the associated Pareto Front is denoted as $J(PF)$ Usually, the Pareto set has infinite solutions, and it is very difficult to reach the exact set. Multi-objective optimization algorithms try to obtain a well-distributed approximation P^* and its corresponding PF^*.

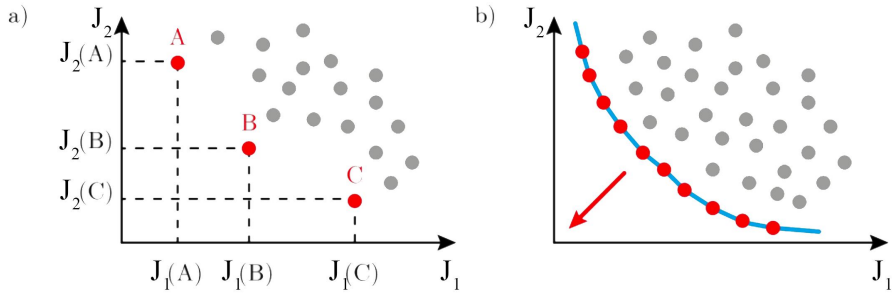

Figure 8.1: a)Three Pareto points within a group, b) Pareto front. The red arrow indicates the direction that the optimization process should pursue, guiding the algorithm to generate new individuals and, as a result, achieve improved outcomes in subsequent generations of groups.

In this work, a multi-objective evolutionary algorithm based on the concept of e-dominance, named ev-MOGA [43, 44] is used.

Epsilon Variable Multi-Objective Genetic Algorithm (ev-MOGA)

The Epsilon Variable Multi-Objective Genetic Algorithm (ev-MOGA) is an evolutionary optimization method designed to efficiently solve multi-objective problems by balancing convergence and diversity in the Pareto front. The algorithm integrates the concept of ϵ-dominance to maintain a manageable number of Pareto-optimal solutions while preserving the spread of solutions across the objective space.

Key Features of ev-MOGA:

1. **ϵ-dominance:** The use of ϵ-dominance allows the algorithm to discard solutions that do not provide significant improvement, thereby reducing the computational cost and simplifying the Pareto set. The ϵ parameter defines a threshold, ensuring that only solutions contributing meaningful diversity are retained.

2. **Variable ϵ:** Unlike traditional approaches that use a fixed ϵ, ev-MOGA adapts the value of ϵ dynamically during the optimization process. This flexibility enhances the algorithm's ability to explore the objective space and adjust to the problem's complexity as the search progresses.

3. **Fitness Assignment:** Solutions are ranked based on their ϵ-dominance level. Non-dominated solutions are assigned the highest fitness, and a secondary fitness criterion is applied to promote diversity among solutions.

4. **Pareto Set Approximation:** ev-MOGA generates a well-distributed approximation of the Pareto front by focusing on both convergence towards the optimal solutions and maintaining a diverse set of trade-offs across the objectives.

5. **Selection and Variation Operators:** Standard genetic algorithm operators such as selection, crossover, and mutation are used. However, the selection process is guided by the ϵ-dominance criterion to ensure that only diverse and high-quality solutions are propagated to subsequent generations.

The adaptive nature of ev-MOGA, particularly with the variable ϵ, makes it well-suited for complex multi-objective optimization problems where the objective functions may have competing trade-offs. By dynamically adjusting the ϵ threshold, the algorithm ensures a balance between exploring new solutions and refining the existing ones, yielding a well-distributed and representative Pareto front.

Algorithm 3 shows the pseudocode of ev-MOGA.

Initially, the A population is empty, and the main population P is created randomly (uniform distribution). The value of the objectives for each member of the populations is calculated (using the "eval" function) and used for further dominance tests. The actualization of A is performed with the "store" function (based on e-dominance concept). In each iteration (evolution step), the auxiliary population G is obtained with individuals of A and P randomly selected. Crossover and mutation operators are applied

Algorithm 3 Pseudocode of ev-MOGA

```
1: t := 0
2: A_t := ∅
3: P_t := ini_random(D)
4: eval(P)
5: A := store(P, A)
6: while t < t_max do
7:     G := create(P, A);
8:     eval(G);
9:     A_{t+1} := store(G, A);
10:    P_{t+1} := update(G, P);
11:    t := t + 1;
12: end while
```

to obtain the final composition of G. A and P are updated with the values of G (applying e-dominance and dominance respectively). When the finalization condition is achieved, the solution Pareto set is available at A.

Acoustic Simulation framework

If there is one conclusion to be drawn from the previous chapter, it is that for a constructive interaction with the Bragg-BG, the HRs must be properly oriented. The HR↑ ($f_{\mathrm{HR}} < f_c$)must be placed at 0 degrees relative to the incident wave, and the HR↓ ($f_{\mathrm{HR}} < f_c$) at 90 degrees. Therefore, the initial design and all possible combinations of the optimization will adhere to this criterion.

The methodology for interconnecting the optimization algorithm and the FEM numerical model is implemented in the same manner as described in chapter 5, using an FEM model that communicates with the algorithm implemented in Matlab.

Moreover, as will be explained in the section "3D printed Prototype", for faster printing and a more robust cylindrical scatterer, one of the printability constraints is that the width of the openings must be 0.006 m, which corresponds to two passes of the nozzle of the printer that will be used to print the final prototype. As a result, the new neck length ($L*$) is set to $L* = 0.006$ m. In this initial design, the lattice parameter, a, is fixed at 0.012 m for a Bragg frequency, $f_{Bragg} = 1400$ Hz, with Radius $R = 0.045$ m.

The initial design already provided the switchable behaviour that a desirable tunable device should have, but it was not entirely satisfactory. It

produced frequency ranges where, in one of the wave propagation directions (ΓX or $X'\Gamma$), the transmission coefficient was zero, but in that range, the perpendicular direction still reduced transmission by more than 50%. In the "Comparison" section that will be deeply explained.

Fig. 8.2 shows the diagram of the optimization process, where the three decision variables to modify are part of $\vec{x}$:

- x_1 and x_2: The widths of the 90° HR mouth and 0° HR mouth respectively.
- x_3 The angle θ of the internal separation wall of both HRs. The 90º HR with $f_{\mathrm{HR}} < f_c$ and the 0° with $f_{\mathrm{HR}} < f_c$. With f_c as explained in the previous chapter, the central frequency of the first Bragg-BG.

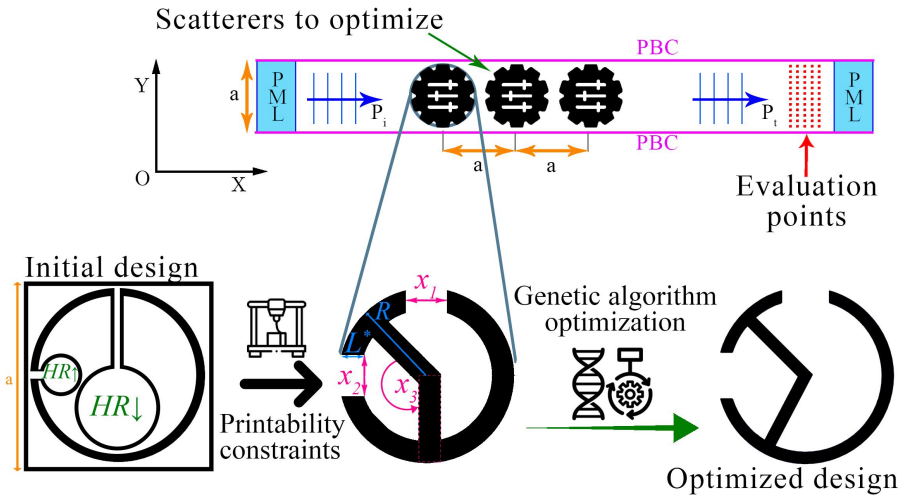

Figure 8.2: Flowchart of the process to optimize the behaviour of the multiresonant SC.

Contrast Ratio:

The first parameter has been referred to in the literature by different names, such as non-reciprocity [154] or Contrast Ratio [155, 156, 157, 158, 159]. In this chapter, we have opted for the latter term, although our approach presents some important differences worth noting. Typically, asymmetric transmission and the CR refer to the difference between left and right incidence when the structure is placed along the y-axis, with "left" and "right" indicating the direction of the incident waves on the x-axis.

In this chapter, the incidence is fixed from left to right (along the x-axis), and the contrast is evaluated based on the orientation of the scatterers in the SC at 0^{o} (ΓX) or 90^{o} ($X'\Gamma$). This normalized function is given by the following equation:

$$CR = \frac{|\tau_{X'\Gamma} - \tau_{\Gamma X}|}{|\tau_{X'\Gamma} + \tau_{\Gamma X}|}, \tag{8.2}$$

where $\tau_{\Gamma X}$ and $\tau_{X'\Gamma}$ represent the transmission coefficients in the ΓX and $X'\Gamma$ directions, respectively. The CR parameter measures the level of non-reciprocal transmission, in the perpendicular settings of the multiresonaont scatterers between the two directions to achieve effective switching behaviour in the SC.

Absolut Difference:

Although the Contrast Ratio (CR) is a well-established objective function for evaluating non-reciprocity, it is incomplete when applied to the specific goal of optimizing the switchable behaviour of the SC. In cases where either $\tau_{\Gamma X}$ or $\tau_{X'\Gamma}$ equals zero, CR fails to provide information about the perpendicular transmission. For instance, when one of the τ values is equal to zero, the Contrast RatioCR is equal to one, regardless of the value of the other τ, as Equation 8.2 can demonstrate.

To overcome this limitation, we introduce a second parameter, which captures the absolute difference in transmission between the two directions. This parameter ensures that variations in transmission are accounted for even when one of the directions shows no transmission:

$$Diff = |\tau_{X'\Gamma} - \tau_{\Gamma X}|, \tag{8.3}$$

This second parameter provides a more complete evaluation of the SC's switching performance by emphasizing the difference between the two transmission settings, regardless of whether one perpendicular transmission is completely blocked.

In the context of the ev-MOGA optimization of a Multiresonant SC with two HRs, these two parameters, CR and $Diff$, work in tandem to optimize the switchable acoustic behaviour. By maximizing the Contrast Ratio (CR) and the Absolut Difference ($Diff$), the optimization process aims to enhance the non-reciprocal behaviour of the SC, ensuring that transmission is maximized in one direction while minimized in the perpendicular direction.

In the next step, a set of cost functions (J_1 and J_2) must be established to carry out the optimization process. It is important to note that the goal of an optimization process is to minimize at least one of the two cost function.

Since the ev-MOGA algorithm is designed to minimize cost functions, as explained previously, and the goal in this case is to maximize the previously defined acoustic parameters, J_1 and J_2 will be transformed accordingly. Specifically, the cost functions will be redefined as $J_1 = 1 - CR$ and $J_2 = 1 - \text{Diff}$, where CR represents the Contrast Ratio and Diff stands for the Difference parameter.

This transformation ensures that the ev-MOGA algorithm can still be used effectively to optimize the acoustic performance, as it now minimizes the complement of the desired metrics.

Although these cost functions have as many values as the calculated frequencies within the range of interest (500-2500 Hz), both J_1 and J_2 will use the mean of all values during the calculation process. This will provide a single value for each function, which will then place each design within the search space and the Pareto front.

3D printed Prototype

To assess the behaviour of the multiresonant SC device, a 3D-printed prototype was created to evaluate its transmission and switchable performance. Specifically, a 3D printer from the Fused Deposition Modelling (FDM) category, the WASP 3MT HDP (Wasp, Massa Lombarda, Italy), was employed due to its large printing area (1000 mm in diameter by 1000 mm in height) and printing quality. Ingeo™ Biopolymer 2003D PLA pellets were used as the printing material, processed at 220°C with a 3 mm-diameter nozzle and a heated bed at 60°C. The layer height, indicative of printing resolution, was set at approximately 1 mm resulting in printing times of around 8 hours.

The 3D model was created using computer-aided design (CAD) software, specifically Rhinoceros 3D (v.7.19.22165.13002). The slicing and toolpath instructions for the WASP 3MT HDP were generated using Simplify3D (version 5.2.1), a slicing software selected for its compatibility with the 3D printer.

To 3D print prototypes with effective rigidity and printing quality, the internal thickness of the multiresonant SC device was set at 6 mm (twice the nozzle diameter). This allows for continuous printing in the slicer software (without interruptions between layers) and achieves a 6 cm thickness with two adjacent passes of the 3 mm extruder. To achieve this, specific printing settings for the extruder's toolpath were implemented to prevent imperfections such as bubbles or gaps. Figure 8.3 on the left shows the extruder's path as configured in the slicer software. In the center, Figure 8.3 displays a digital image of multiple overlapping layers. On the right, there

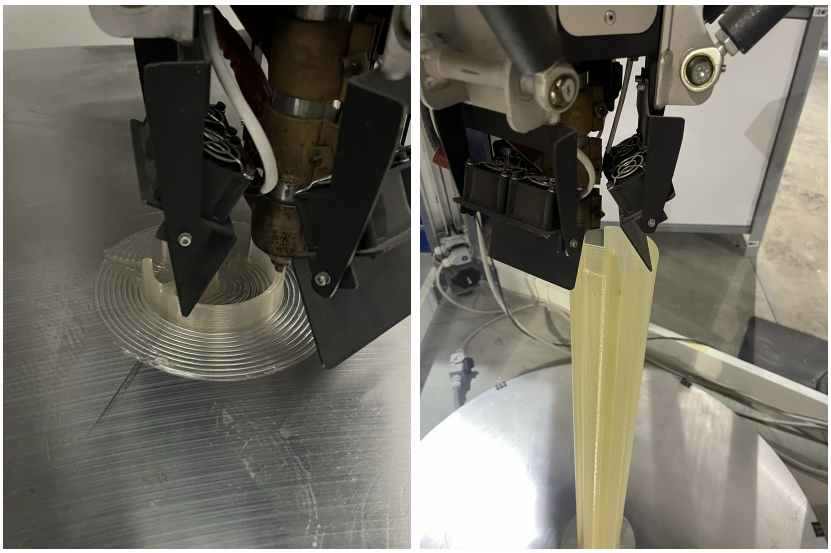

Figure 8.3: Brim that provides support and adhesion for the prototype on the print bed and initial layers(left). Almost completed prototype, with only a few layers remaining(right).

is a zoomed-in view of the toolpath during the transition from one layer to another, highlighting the continuity of the extrusion.

Additionally, given the slenderness of the printed device, a 'brim' was applied to increase adhesion to the print bed. In this case, the brim acts as the first layer, forming a base that anchors the cylindrical scatterer, helping to maintain stability as the 3D printing process builds up the final height, layer by layer. This base results in a circular surface with a diameter ($2R$) of 12 cm.

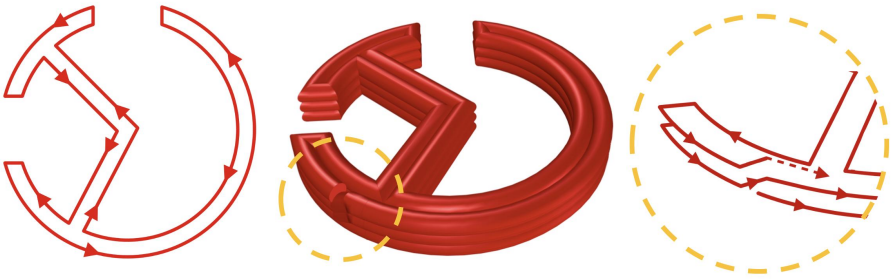

Figure 8.4: Continuous extruder path(left); Digital image of multiple overlapping layers (center); Zoom on the toolpath during the transition, with continuous flow, from one layer to another(right).

Figure 8.4 shows the brim on the left, which supports and adheres the

prototype to the print bed during the initial layers. On the right, the nearly completed prototype is displayed, with only a few layers remaining.

Once completed, the toolpath data were transferred in G-code format to the 3D printer, which then received all the necessary control information to produce the prototype in three dimensions

For "$Ingeo^{\mathrm{TM}}$ Biopolymer 2003D" Polylactic Acid (PLA) , according to the provided technical sheet, the density ρ_{PLA} is approximately $1240 kg/m^3$. The speed of sound in PLA, $c_{\mathrm{PLA}} = 2200$ m/s. Thus: $Z_{\mathrm{PLA}} \approx 1240, \mathrm{kg/m^3} \times 2200, \mathrm{m/s} \approx 2,728,000, \mathrm{Pa{\cdot}s/m}$

The acoustic impedance of PLA is significantly higher than that of air: $\frac{Z_{\mathrm{PLA}}}{Z_{\mathrm{air}}} \approx \frac{2{,}728{,}000}{420} \approx 6495$ The large impedance change results in PLA behaving almost like a acoustically perfectly rigid material.

Experimental Set up

With the goal of experimentally validating the switchable performance of the SC device, after 3D printing a prototype, acoustic tests were conducted in the anechoic chamber of the Polytechnic School of Gandia (Valencia, Spain).

An experimental set-up is designed to characterize the transmission properties of the multiresonant SC device in an anechoic chamber and to obtain quantitative data of the acoustic field behind the switch. The dimensions of the echo-free chamber are $8 \times 6 \times 4\,\mathrm{m}^3$. The automatized acquisition system consists of a 3D Robotized Acoustic Measurement System that was used to scan the acoustic field distribution. Both the source and the SC were placed and accurately oriented.

The source is located in front of the SC at a distance of 0.5 m and at a height of 0.4 m. It is placed at the midpoint of the 0.8 m height of the scatterers. To maintain the correct distance between the 3D-printed cylindrical scatterers, they are placed on a rigid wooden base with predrilled holes. The measurement area is a rectangle with dimensions of 1.1×0.5 m, leaving 0.09 m on each side of the barrier (y-axis) and starting 0.05 m from the edge of the last row of scatterers. Samples are taken using a rectangular grid with a spacing of $a/4$, i.e., 0.003 m.

A Genelec 8030A active loudspeaker serves as the sound source. It emits white noise, and at each measurement position, the microphone takes an average of three measurements. The frequency range of interest is from 500 to 2500 Hz.

A prepolarized free-field 1/2 microphone Type 4189 B&K has been used throughout the experiments. Before using it, it has been calibrated with a B&K Sound calibrator type 4231. In order to obtain precise sound pressure

maps, the three-dimensional Robotized Acoustic Measurement System is capable of sweeping the microphone through a 3D grid of measuring points located at any trajectory inside the anechoic chamber.The motion of the robot is controlled by a computer outside the chamber.

Figure 8.5 shows the side view of the experimental set-up.

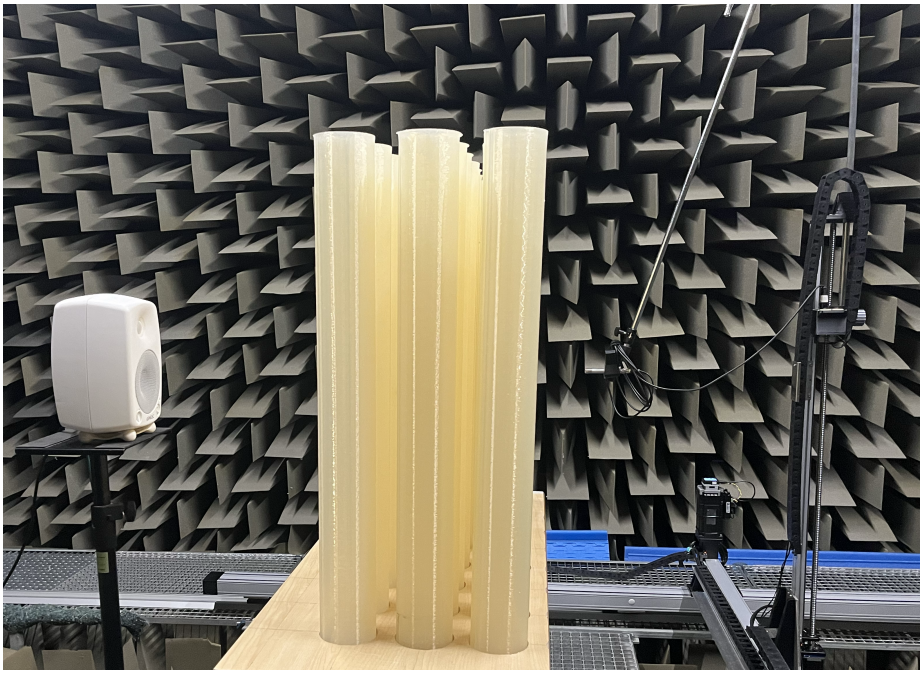

Figure 8.5: Experimental set up.

8.3 Results

Optimization Results

In Figure 8.6, the variation of the Pareto front as a function of the generations of the optimization is observed. On the X-axis, the cost function J_1 is plotted, and on the Y-axis, the cost function J_2, which is the more restrictive one. The initial design with the internal wall at 90^{o} proposed in the previous chapter gave average values in the range of 500-2500 Hz of $J_1 = 0.196$ and $J_2 = 0.565$.

Therefore, the individual selected from the Pareto front is the one with the lowest J_2 value since the J_1 values are much lower. This is because the CR is less restrictive as previously explained, meaning it is easier to contribute values = 1 since it does not take into account the other transmission that is not equal to 0. The multi-objective optimization process was carried out with 200 population individuals and over 350 generations.

As can be seen in the colors of the Pareto fronts, from approximately generation 200 onwards, there have not been significant variations in the upper part of the Pareto, but observing the Y-axis and the lower part of the Pareto, it has decreased considerably. The final selected individual has values of $J_1 = 0.182$ and $J_2 = 0.476$.

Seen this way, it may not seem like a great improvement, but it is true that it started from a fairly good initial design. Moreover, when these average values are broken down by frequency, the improvement in behavior as a tunable switch through the rotation of all scatterers to 90^{o} can be better appreciated.

In the next section, a deeper analysis of the improvement obtained after optimization is carried out, analyzing the band diagrams and the transmission coefficient.

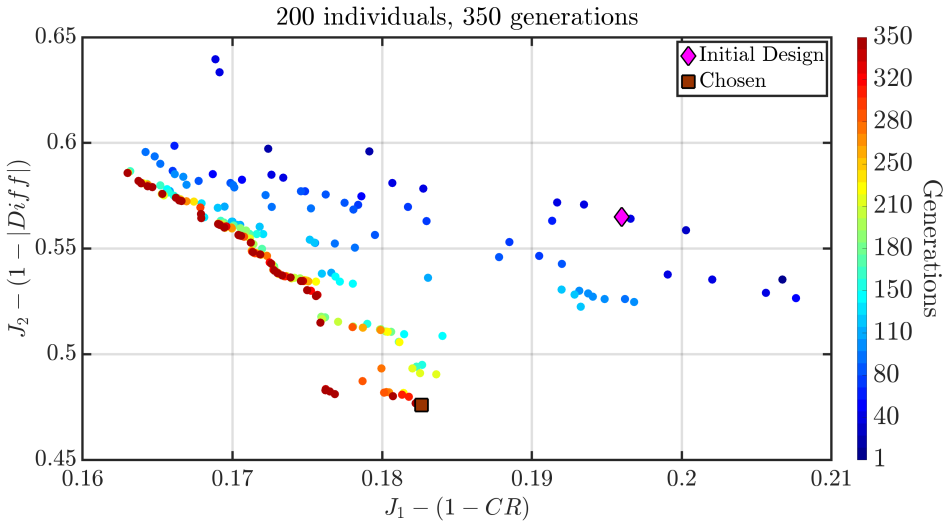

Figure 8.6: Pareto Front variation with colours depending on the generation.

Numerical Comparison

The relative value of the local resonances of the HRs (f_{HR}) with respect to the central frequency of the Bragg-BG (f_{Bragg}) is an important factor as it determines the interaction between the two BGs. The use of HRs in CS does not necessarily reduce the transmission through the crystal. Therefore, special attention must be paid to the alignment of the mouths and the fundamental frequencies of the HRs incorporated into the scatterers. Figure 8.2 shows a scatterer consisting of two HRs aligned at 0° and 90°, with coupled surfaces. The internal separation angle is $\theta = 110°$, which defines the wall between the two HRs. The central frequency of the Bragg-BG is $f_{\text{Bragg}} = 1400$ Hz, and the fundamental frequencies of the HRs satisfy that the larger cavity (90°) has $f_{\text{HR}} < f_{\text{Bragg}} = 760Hz$, and the smaller cavity (0°) has $f_{\text{HR}} > f_{\text{Bragg}} = 1800$ Hz. Both HRs have identical mouths with a size of $w = 0.025m$ and length $L = 0.006m$. The subsequent section delves into a detailed analysis of the simulation results, exploring the interactions and providing a comprehensive understanding of the mechanisms governing the interaction between Bragg scattering and local resonances in SC.

In the band structure of figure 8.7 ploted in grey, complete Band Gaps (BGs) are represented for all propagation directions (ΓX, XM, MX', $X'\Gamma$). In blue, partial BGs are shown for 0° (ΓX), and in red, BGs for 90° ($X'\Gamma$). A dashed black line in the left band diagram depicts the band structure of a Sonic Crystal (SC) with rigid scatterers and no HRs, with a radius equal

to the outer radius of the multiresonant scatterers under study [116].

The same numerical model as in Figure 7.1 of previous chapter is used. Changes in transmission behaviour result from variations in incidence on the HR surfaces, when rotating scatterers 90º.

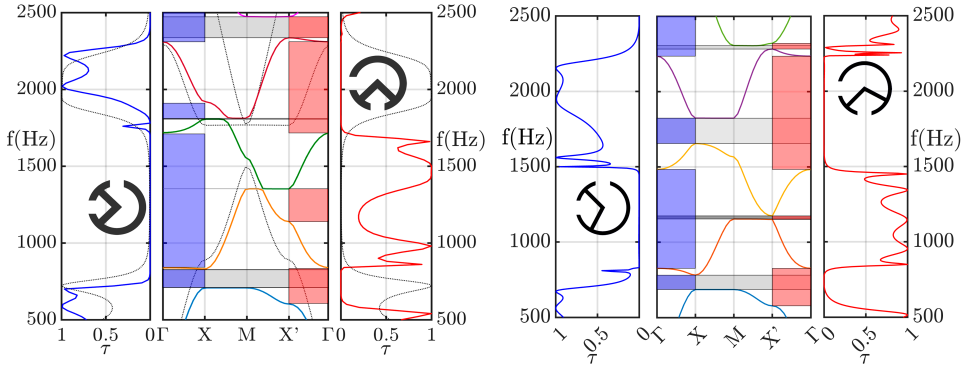

Figure 8.7: Band diagram comparison before (left) and after optimization process (right).

To provide a comprehensive comparison, it is prudent to analyze the plots by parts. First, we examine the partial Band Gap (BG) at 0° (blue), followed by the partial BG at 90° (red), which ideally should complement the blue BG. Finally, we consider the complete BGs, represented in gray, which impede or reduce transmission across those ranges for any incident wave orientation relative to the scatterers.

In the left side of Figure 8.7, prior to optimization, at an orientation of 0° (ΓX), it is observed that there is no transmission within the frequency range of the Bragg BG (750-1700 Hz). However, for that same frequency range, we can see that between 1040-1320 Hz, the value of τ (red) is less than 0.5, thereby attenuating more than half of the transmitted energy, which is undesirable since the 0° configuration should not permit transmission.

Concerning the optimized device, ilustrated on the right part of Figure 8.7, at an orientation of 0° (ΓX), $\tau = 0$ indicates no propagation within the Bragg BG frequency range (830-1485 Hz). As can be observed, the 0° BG (blue) has been reduced in width, affecting fewer frequencies. However, within this same range, its complementary counterpart in red exhibits values greater than $\tau = 0.5$ across the optimized case, which did not occur prior to optimization.

On the other hand, the partial BG at 90° ($X'\Gamma$, red) that spans from 1720 - 2470 Hz in the left image shifts to 1500 - 2250 Hz after optimization, but it does not reduce in width, maintaining a span of 750 Hz. Before

optimization, only in the range of 1940 - 2280 Hz were there values exceeding 0.5 in the transmission coefficient (blue τ), indicating that in the remaining range, transmission was also reduced.

Finally, it is worth noting that the complete BGs are represented in gray, indicating frequencies for which transmission is reduced regardless of the scatterer's orientation. These BGs were not included in the cost function parameters for optimization, but they have been modified before and after the optimization process. Prior to optimization, the BGs were located at 710-826 Hz, 1352 Hz, 1810 Hz, and 2334-2470 Hz. After optimization, they appear for the following frequency ranges: 685-781 Hz, 1151-1174 Hz, 1655-1824 Hz, and 2282-2304 Hz. Those frequencies above and below the Bragg frequency $f_{\text{Bragg}} = 1400$ Hz coincide with the resonance frequencies of the HRs (f_{HR}).

Experimental Results

In this subsection, a comparison is made between the measurements conducted for experimental validation and the finite numerical model.

As outlined in previous chapters, the requirement for a computationally efficient approach to optimization has resulted in the utilization of a periodic model during the optimization phase and a finite structure for comparison with validation under normal incidence, as discussed in chapter 6.

It is noticeable in Figure 8.8 that τ values exceeding unity are observed at certain frequencies. Such values are considered unphysical, arising from the calculations of τ, which were based on the assumption of a plane wavefront propagating perpendicularly to the sample surface. This methodology represents an approximation to the complete two-dimensional problem, presuming that the incident, reflected, and transmitted waves all exhibit plane wavefronts traveling in the direction normal to the surfaces of the sample.

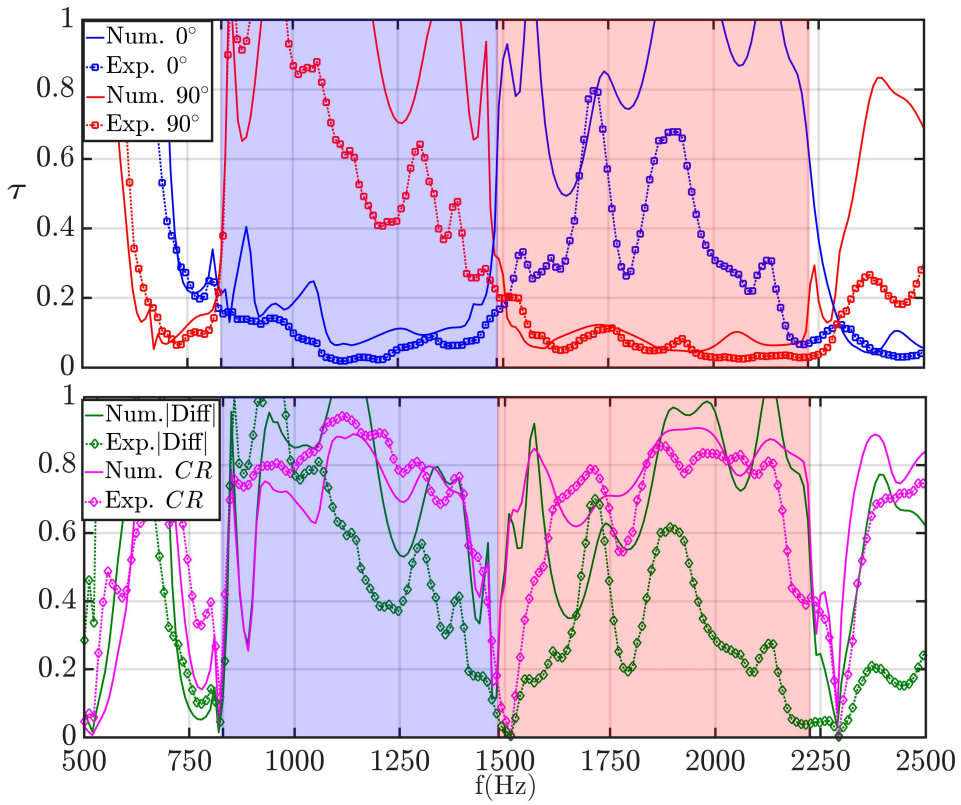

Figure 8.8: Transmittance, Numerical and Experimental (up); Optimization objectives, Numerical and experimental (down).

This assumption is deemed valid in our setup, as the loudspeaker is positioned sufficiently far from the sample. It has also been widely employed in prior studies [160, 161], where a strong correlation between experimental data and simulations based on this approach has been consistently observed.

Furthermore, the authors propose additional reasons for the occasional occurrence of transmittance values greater than one. These include potential diffraction effects at the edges of the barriers due to their finite dimensions and interference patterns induced by the scattered waves. The interaction of waves with the edges and base of the structure, particularly given the periodic arrangement of the scatterers, may lead to constructive interference in specific directions, resulting in localized sound wave amplification. Additionally, reflections from the rigid base could further alter the overall sound field, complicating the measurement of τ.

The pronounced decrease in the CR observed in the range between 1500 and 1800 Hz aligns closely with the predictions made by the band structure in Figure 8.7(rigth) and the complete BG present at 1655-1824 Hz.

Given that previous chapter have utilized SCs with various HRs as noise barrier, in addition to the linear parameter that evaluates transmission (τ), it has been chosen to represent the more commonly used parameter in noise barriers, the Insertion Loss in dB (7.2). Figure 8.9 shows that the frequency ranges coincide. It is true that the expected levels from the 2D simulation only account for diffraction at the lateral edges, and experimental measurements indicate that the upper edge also creates a diffraction limit. Even with a completely opaque and rigid barrier, the finite size would lead to saturation in the IL as it was deeply anaylysed in chapter 6.

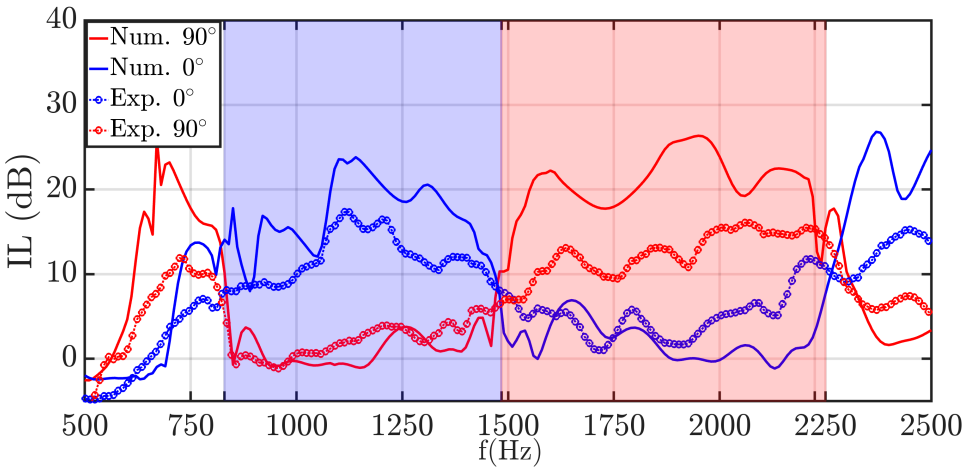

Figure 8.9: Insertion Loss of the Multiresonant SC with scatterers at $0^{\underline{o}}$ and $90^{\underline{o}}$.

8.4 Conclusions

In conclusion, this chapter presents an innovative approach to a Multiresonant SC device, focusing on the interaction between Bragg-BGs and HRs-BGs in a simple and cost-effective 3D printed multiresonant structure. The chapter demonstrates that by tuning the orientation of these scatterers, a significant change in the acoustic insulation performance can be achieved, effectively switching between different frequency ranges. The device operates in the low-mid-frequency range (500-2500 Hz), addressing the limitations of existing acoustic switches that often require complex geometries or work at higher frequencies. The simplicity of the design, combined with the absence of infill in the 3D printed cylindrical scatterers, minimizes absorption phenomena and enhances the practicality of the concept.

Future research could explore the integration of this technology with advanced materials or further optimize the geometry and orientation of the resonators to enhance the tunability and performance of the acoustic switch. Back in 2001, an application of automatic silencer was implemented with FFT calculations to tune HRs [162]. For future works, artificial Intelligence control could be very useful to dynamically control the orientation of the scatterers leading to the development of intelligent noise-canceling systems capable of adapting to varying acoustic environments such as recent works have proved [163].

The potential practical applications for this technology are numerous, ranging from noise reduction in urban landscapes and industrial settings to the creation of adaptive acoustic environments within buildings and vehicles. It could also find use in the design of acoustic sensors, sonar devices, and acoustic logic gates [164]. Moreover, the perspective to harvest acoustic energy [165] from the environment presents exciting prospects for powering small electronic devices, contributing to sustainable and eco-friendly technologies. The versatility and ease of implementation of this sonic crystal design open new avenues for researchers and engineers to explore in the realms of wave manipulation and acoustic metamaterials.

Part V

Conclusions

Conclusions

The present doctoral thesis, "Control and Optimization Strategies for Noise Transmission Reduction in Sonic Crystal Acoustic Barriers," tries to be a significant advancement in the field of acoustic metamaterials, with a particular focus on Sonic Crystal Noise barriers (SCNBs). The research presented herein has sought to address the challenges associated with the design and implementation of these innovative materials in real-world noise control applications. Through a comprehensive study of the interactions between SCNBs, active noise control (ANC) systems, Helmholtz resonators (HRs), and advanced modeling techniques, the thesis has made several key contributions to the knowledge base.

The primary objective was to enhance the performance of noise reduction devices, specifically SCNBs, through innovative design and optimization strategies. This was achieved through the integration of metamaterial theory with computational methods such as finite difference time domain (FDTD) simulations and evolutionary algorithms. The study has successfully demonstrated the potential of these materials to minimize unwanted sound in various environments, thereby improving the acoustic quality of life.

The thesis has highlighted the importance of a multidisciplinary approach to the development of effective noise control solutions. By combining the principles of acoustics with advanced computational techniques and machine learning, the study has developed a novel framework for optimizing the design of SCNBs. This approach has led to the creation of prototypes that exhibit significant improvements in insertion loss, especially in the low-frequency range where traditional passive barriers tend to be less effective.

Furthermore, the integration of ANC systems with reinforcement learning (RL) has shown promise in enhancing the adaptive capabilities of noise control devices. The proposed methods can continuously learn and adapt to changing environmental conditions, providing a dynamic solution that is responsive to the complex and often unpredictable nature of real-world noise.

The study has also explored the potential of 3D printing technology in the fabrication of SCNB in Pellet, and FDM. This has allowed for greater flexibility in the design and testing of prototypes, which is essential for the rapid iteration required in the optimization process. The use of parametric modeling has facilitated the creation of complex and customizable structures that can be easily modified and scaled to meet the specific requirements of various applications.

The experimental validation of the theoretical models has been conducted under both normal and diffuse incidence conditions, which is crucial for assessing the performance of these devices in real-world scenarios. The results obtained have not only corroborated the numerical findings but also provided valuable insights into the practical limitations and potential.

References

[1] Lawrence E. Kinsler, Austin R. Frey, Alan B. Coppens, and James V. Sanders. *Fundamentals of Acoustics*, volume 72. John Wiley & Sons, New York, US, 2000. ISBN 978-0-471-84789-2.

[2] Floyd Alton Everest and Ken Pohlmann. *Master Handbook of Acoustics*. McGraw-Hill/TAB Electronics, June 2009. ISBN 0-07-160332-8. doi: 10.1036/9780071603331.

[3] Auguste Bravais. *Mémoire Sur Les Systèmes Formés Par Des Points Distribués Régulièrement Sur Un Plan Ou Dans l'espace*. Bachelier, Paris, 1850. ISBN 557593632.

[4] Felix Bloch. Über die Quantenmechanik der Elektronen in Kristallgittern. *Zeitschrift für Physik*, 55:555–600, 1928. doi: 10.1007/bf01339455.

[5] Gaston Floquet. Sur les équations différentielles linéaires à coefficients périodiques. *Annales Scientifiques de l'Ecole Normale Superieure*, 12: 47–88, 1883. doi: 10.24033/asens.220.

[6] Leon Brillouin. *Wave Propagation in Periodic Structures*. Dover, New York, 1953.

[7] Lawrence Bragg. X-Ray Crystallography. *Scientific American*, 219 (1):58–74, 1968.

[8] Charles Kittel. *Introduction to Solid State Physics*. Wiley, Hoboken, NJ, 8th ed edition, 2005. ISBN 978-0-471-41526-8.

[9] Eleftherios Economou and Michael M. Sigalas. Elastic and acoustic wave band structure. *Journal of sound and vibration*, 158(2):377–382,, 1992. doi: 10.1016/0022-460x(92)90059-7.

[10] Manvir S. Kushwaha. The phononic crystals: An unending quest for tailoring acoustics. *Modern Physics Letters B*, 30(19):1630004, July 2016. ISSN 0217-9849, 1793-6640. doi: 10.1142/S0217984916300040.

[11] M.M. Sigalas and E.N. Economou. Elastic and acoustic wave band structure. *Journal of Sound and Vibration*, 158(2):377–382, October 1992. ISSN 0022460X. doi: 10.1016/0022-460X(92)90059-7.

[12] C. Rubio, D. Caballero, J.V. Sanchez-Perez, R. Martinez-Sala, J. Sanchez-Dehesa, F. Meseguer, and F. Cervera. The existence of full gaps and deaf bands in two-dimensional sonic crystals. *Journal of Lightwave Technology*, 17(11):2202–2207, Nov./1999. ISSN 07338724. doi: 10.1109/50.803012.

[13] Winston E. Kock and F. K. Harvey. Refracting Sound Waves. *The Journal of the Acoustical Society of America*, 21(5):471–481, September 1949. ISSN 0001-4966, 1520-8524. doi: 10.1121/1.1906536.

[14] Vicente Romero-García, Juan Vicente Sánchez-Pérez, and Luis Miguel Garcia-Raffi. Tunable wideband bandstop acoustic filter based on two-dimensional multiphysical phenomena periodic systems. *Journal of Applied Physics*, 110(1):014904:1–014904:11, July 2011. ISSN 0021-8979, 1089-7550. doi: 10.1063/1.3599886.

[15] Javier Redondo, Rubén Picó, Victor Sánchez-Morcillo, and Wieslaw Woszczyk. Sound diffusers based on sonic crystals. *The Journal of the Acoustical Society of America*, 134(6):4412–4417, December 2013. ISSN 0001-4966, 1520-8524. doi: 10.1121/1.4828826.

[16] Juan V. Sanchez-Perez, Constanza Rubio, Rosa Martinez-Sala, Rafael Sanchez-Grandia, and Vicente Gomez. Acoustic barriers based on periodic arrays of scatterers. *Applied Physics Letters*, 81(27):5240–5242, December 2002. ISSN 0003-6951, 1077-3118. doi: 10.1063/1.1533112.

[17] Toyokatsu Miyashita. Sonic crystals and sonic wave-guides. *Measurement Science and Technology*, 16(5):R47–R63, May 2005. ISSN 0957-0233, 1361-6501. doi: 10.1088/0957-0233/16/5/R01.

[18] P.K. Tang and W.A. Sirignano. Theory of a generalized Helmholtz resonator. *Journal of Sound and Vibration*, 26(2):247–262, January 1973. ISSN 0022460X. doi: 10.1016/S0022-460X(73)80234-2.

[19] Giuseppe Catapane, D. Magliacano, G. Petrone, A. Casaburo, F. Franco, and S. Rosa. Semi-analytical estimation of Helmholtz resonators' tuning frequency for scalable neck-cavity geometric couplings. *CEAS Aeronautical Journal*, 13(3):797–808,, 2022. doi: 10.1007/s13272-022-00592-4.

[20] European Commission. Directorate General for Environment. and The European Parliament and the Council of the European Union. Implementation of the Environmental Noise Directive in accordance with Article 11 of Directive 2002/49/EC. Technical report, European Comission, Brussels, 2023.

[21] Cyril M. Harris. *Handbook of Acoustical Measurements and Noise Control*. McGraw-Hill, New York, 1991.

[22] U.S. Department of Transportation Federal Highway Administration. United States Department of Transportation Annual Modal Research Plans Fiscal Year 2019 -. Technical Report FHWA FY2019-FY2020 AMRP, 2018.

[23] Luca Fredianelli, Lara Ginevra Del Pizzo, and Gaetano Licitra. Recent Developments in Sonic Crystals as Barriers for Road Traffic Noise Mitigation. *Environments*, 6(2):14, January 2019. ISSN 2076-3298. doi: 10.3390/environments6020014.

[24] You-Yu Chen and Zhen Ye. Theoretical analysis of acoustic stop bands in two-dimensional periodic scattering arrays. *Physical Review E*, 64(3):036616:1–036616:16, August 2001. ISSN 1063-651X, 1095-3787. doi: 10.1103/PhysRevE.64.036616.

[25] M. M Sigalas and E. N Economou. Attenuation of multiple-scattered sound. *Europhysics Letters (EPL)*, 36(4):241–246, November 1996. ISSN 0295-5075, 1286-4854. doi: 10.1209/epl/i1996-00216-4.

[26] Manvir S. Kushwaha. Stop-bands for periodic metallic rods: Sculptures that can filter the noise. *Applied Physics Letters*, 70(24):3218–3220, June 1997. ISSN 0003-6951, 1077-3118. doi: 10.1063/1.119130.

[27] Federica Morandi, Marco Miniaci, Alessandro Marzani, Luca Barbaresi, and Massimo Garai. Standardised acoustic characterisation of sonic crystals noise barriers: Sound insulation and reflection properties. *Applied Acoustics*, 114:294–306, December 2016. ISSN 0003682X. doi: 10.1016/j.apacoust.2016.07.028.

[28] Gino Iannace, Giuseppe Ciaburro, and Amelia Trematerra. Metamaterials acoustic barrier. *Applied Acoustics*, 181:108172, October 2021. ISSN 0003682X. doi: 10.1016/j.apacoust.2021.108172.

[29] Jose Maria Bravo-Plana-Sala, Fernando Buchón-Moragues, Javier Redondo, Marcelino Ferri, and Juan Vicente Sánchez-Pérez. Integrated Photogrammetric-Acoustic Technique for Qualitative Analysis of the Performance of Acoustic Screens in Sandy Soils. *Sensors*, 19(22):4881, November 2019. ISSN 1424-8220. doi: 10.3390/s19224881.

[30] José Sánchez-Dehesa, Victor M. Garcia-Chocano, Daniel Torrent, Francisco Cervera, Suitberto Cabrera, and Francisco Simon. Noise control by sonic crystal barriers made of recycled materials. *The Journal of the Acoustical Society of America*, 129(3):1173–1183, March 2011. ISSN 0001-4966, 1520-8524. doi: 10.1121/1.3531815.

[31] Clément Lagarrigue, Jean-Philippe Groby, and Vincent Tournat. Sustainable sonic crystal made of resonating bamboo rods. *The Journal of the Acoustical Society of America*, 133(1):247–254, January 2013. ISSN 0001-4966, 1520-8524. doi: 10.1121/1.4769783.

[32] Tommaso D'Orazio, Francesco Asdrubali, Luís Godinho, Matheus Veloso, and Paulo Amado-Mendes. Experimental and Numerical Analysis of Wooden Sonic Crystals Applied as Noise Barriers. *Environments*, 10(7):116:1–116–20, July 2023. ISSN 2076-3298. doi: 10.3390/environments10070116.

[33] Sergio Castiñeira-Ibáñez, Constanza Rubio, Vicent Romero-García, Juan Vicente Sánchez-Pérez, and Luís Miguel García-Raffi. Design, Manufacture and Characterization of an Acoustic Barrier Made of Multi-Phenomena Cylindrical Scatterers Arranged in a Fractal-Based Geometry. *Archives of Acoustics*, 37(4):455–462, December 2012. ISSN 0137-5075. doi: 10.2478/v10168-012-0057-9.

[34] Vicente Romero-García, Anton Krynkin, Luis M. García-Raffi, Olga Umnova, and Juan Vicente Sánchez-Pérez. Multi-resonant scatterers in sonic crystals: Locally multi-resonant acoustic metamaterial. *Journal of Sound and Vibration*, 332(1):184–198, January 2013. ISSN 0022460X. doi: 10.1016/j.jsv.2012.08.003.

[35] L Chalmers, D P Elford, F V Kusmartsev, and G M Swallowe. ACOUSTIC BAND GAP FORMATION IN TWO-DIMENSIONAL LOCALLY RESONANT SONIC CRYSTALS COMPRISED OF HELMHOLTZ RESONATORS.

[36] M.P. Peiró-Torres, M. Ferri, L.M. Godinho, P. Amado-Mendes, F.J. Vea Folch, and J. Redondo. Normal in-cidence sound insulation provided by Sonic Crystal Acoustic Screens made from rigid scatterers – assessment of different simulation methods. *Acta Acustica*, 5(28), 2021.

[37] Jaime Galiana Nieves, Rubén Picó, Romina Del Rey, Jesús Alba, and Javier Redondo. Assessment of the sound reduction index provided by noise barriers with low sound insulation. *Applied Acoustics*, 220: 109967, April 2024. ISSN 0003682X. doi: 10.1016/j.apacoust.2024.109967.

[38] EN 1793-2: Road traffic noise reducing devices - Test method for determining the acoustic performance - Part 2: Intrinsic characteristics of airborne sound insulation under diffuse sound field conditions.

[39] EN 1793-3: Road traffic noise reducing devices - Test method for determining the acoustic performance - Part 3: Normalized traffic noise spectrum., 1998.

[40] EN 1793-6: Road traffic noise reducing devices - Test method for determining the acoustic performance - Part 6: In situ values of airborne sound insulation under direct sound field conditions., 2023.

[41] Xavier Blasco. Basic genetic algorithm", "MATLAB central file exchange, 2022.

[42] James Kennedy and Russel Eberhart. Particle swarm optimization. In *IEEE International Conference on Neural Networks*, Perth, WA (Australia, 1995. doi: 10.1109/icnn.1995.488968.

[43] J.M. Herrero, X. Blasco, M. Martínez, C. Ramos, and J. Sanchis. Non-linear robust identification of a greenhouse model using multi-objective evolutionary algorithms. *Biosystems Engineering*, 98(3):335–346, November 2007. ISSN 15375110. doi: 10.1016/j.biosystemseng.2007.06.004.

[44] J. M. Herrero, S. García-Nieto, X. Blasco, V. Romero-García, J. V. Sánchez-Pérez, and L. M. Garcia-Raffi. Optimization of sonic crystal attenuation properties by ev-MOGA multiobjective evolutionary algorithm. *Structural and Multidisciplinary Optimization*, 39(2): 203–215, August 2009. ISSN 1615-147X, 1615-1488. doi: 10.1007/s00158-008-0323-7.

[45] Timothy P. Lillicrap, Jonathan J. Hunt, Alexander Pritzel, Nicolas Heess, Tom Erez, Yuval Tassa, David Silver, and Daan Wierstra. Continuous control with deep reinforcement learning, 2016.

[46] Richard S. Sutton and Andrew Barto. *Reinforcement Learning: An Introduction*. Adaptive Computation and Machine Learning. The MIT Press, Cambridge, Massachusetts London, England, second edition edition, 2020. ISBN 978-0-262-03924-6.

[47] Vincent Francois-Lavet, Peter Henderson, Riashat Islam, Marc G. Bellemare, and Joelle Pineau. An Introduction to Deep Reinforcement Learning. 2018. doi: 10.48550/ARXIV.1811.12560.

[48] J. Redondo, R. Picó, B. Roig, and M. R. Avis. Time Domain Simulation of Sound Diffusers Using Finite-Difference Schemes. *ACTA ACUSTICA UNITED WITH ACUSTICA*, 93:611–622, 2007.

[49] Allen Taflove, Susan C. Hagness, and Melinda Piket-May. Computational Electromagnetics: The Finite-Difference Time-Domain Method. In *The Electrical Engineering Handbook*, pages 629–670. Elsevier, 2005. ISBN 978-0-12-170960-0. doi: 10.1016/B978-012170960-0/50046-3.

[50] Jean-Pierre Berenger. A perfectly matched layer for the absorption of electromagnetic waves. *Journal of Computational Physics*, 114(2): 185–200, October 1994. ISSN 00219991. doi: 10.1006/jcph.1994.1159.

[51] F. Mbailassem, E. Gourdon, Q. Leclère, E. Redon, and T. Cambonie. Sound absorption prediction of linear damped acoustic resonators using a lightweight hybrid model. *Applied Acoustics*, 150:14–26,, 2019. doi: 10.1016/j.apacoust.2019.01.031.

[52] Iván Herrero-Durá, Alejandro Cebrecos, Rubén Picó, Vicente Romero-García, Luis Miguel Garcia-Raffi, and Victor Sánchez-Morcillo. Sound Absorption and Diffusion by 2D Arrays of Helmholtz Resonators. *Applied Sciences*, 10:1690,, 2020. doi: 10.3390/app10051690.

[53] Ronald Kampinga. *Viscothermal Acoustics Using Finite Elements, Analysis Tools for Engineers*. University of Tweente, The Netherlands, 2010.

[54] Valentino Sangiorgio, Fabio Parisi, Francesco Fieni, and Nicola Parisi. The New Boundaries of 3D-Printed Clay Bricks Design: Printability

of Complex Internal Geometries. *Sustainability*, 14(2):598, January 2022. ISSN 2071-1050. doi: 10.3390/su14020598.

[55] Rhinoceros 3D. (2023, November). Rhinoceros 3D website. https://www.rhino3d.com/.

[56] Jiangyi Zhang, Bo Hu, and Shibo Wang. Review and perspective on acoustic metamaterials: From fundamentals to applications. *Applied Physics Letters*, 123(1):010502, July 2023. ISSN 0003-6951, 1077-3118. doi: 10.1063/5.0152099.

[57] María Pilar Peiró-Torres, Javier Redondo, Jose Maria Bravo-Plana-Sala, and Juan Vicente Sánchez-Pérez. Open Noise Barriers Based on Sonic Crystals. Advances in Noise Control in Transport Infrastructures. *Transportation Research Procedia*, 18:392–398, 2016. ISSN 23521465. doi: 10.1016/j.trpro.2016.12.051.

[58] Zyun Maekawa. Noise reduction by screens. *Applied Acoustics*, 1(3): 157–173, July 1968. ISSN 0003682X. doi: 10.1016/0003-682X(68)90020-0.

[59] S.M. Kuo and D.R. Morgan. Active noise control: A tutorial review. *Proceedings of the IEEE*, 87(6):943–975, June 1999. ISSN 00189219. doi: 10.1109/5.763310.

[60] Francesco Mori, Andrea Santoni, Patrizio Fausti, Francesco Pompoli, Paolo Bonfiglio, and Pietro Nataletti. The Effectiveness of Least Mean Squared-Based Adaptive Algorithms for Active Noise Control System in a Small Confined Space. *Applied Sciences*, 13(20):11173, October 2023. ISSN 2076-3417. doi: 10.3390/app132011173.

[61] Guoqiang Lu, Renwen Chen, and Hao Liu. Active Noise Control Scheme for Smart Beds Based on a Wide and Narrow Band Hybrid Control Algorithm. *IEEE Access*, 11:92617–92627, 2023. ISSN 2169-3536. doi: 10.1109/ACCESS.2023.3308694.

[62] Fareeha Jabeen, Alina Mirza, Ayesha Zeb, Muhammad Imran, Farkhanda Afzal, and Ayesha Maqbool. FxRLS Algorithms Based Active Control of Impulsive Noise With Online Secondary Path Modeling. *IEEE Access*, 9:117471–117485, 2021. ISSN 2169-3536. doi: 10.1109/ACCESS.2021.3105902.

[63] Shiro Ise, Hiroo Yano, and Hideki Tachibana. Basic study on active noise barrier. *Journal of the Acoustical Society of Japan (E)*, 12(6): 299–306, 1991. ISSN 0388-2861, 2185-3509. doi: 10.1250/ast.12.299.

[64] Shahin Sohrabi, Teresa Pàmies Gómez, and Jordi Romeu Garbí. Suitability of Active Noise Barriers for Construction Sites. *Applied Sciences*, 10(18):6160, September 2020. ISSN 2076-3417. doi: 10.3390/app10186160.

[65] Jingnan Guo and Jie Pan. Increasing the insertion loss of noise barriers using an active-control system. *The Journal of the Acoustical Society of America*, 104(6):3408–3416, December 1998. ISSN 0001-4966, 1520-8524. doi: 10.1121/1.423924.

[66] Weisong Chen, Wei Rao, Hequn Min, and Xiaojun Qiu. An active noise barrier with unidirectional secondary sources. *Applied Acoustics*, 72(12):969–974, December 2011. ISSN 0003682X. doi: 10.1016/j.apacoust.2011.06.006.

[67] Gaetano Volpe, Agostino Marcello Mangini, and Maria Pia Fanti. A Deep Reinforcement Learning Approach for Competitive Task Assignment in Enterprise Blockchain. *IEEE Access*, 11:48236–48247, 2023. ISSN 2169-3536. doi: 10.1109/ACCESS.2023.3276859.

[68] Fabio Parisi, Valentino Sangiorgio, Nicola Parisi, Agostino M. Mangini, Maria Pia Fanti, and Jose M. Adam. A new concept for large additive manufacturing in construction: Tower crane-based 3D printing controlled by deep reinforcement learning. *Construction Innovation*, January 2023. ISSN 1471-4175, 1471-4175. doi: 10.1108/CI-10-2022-0278.

[69] Behrooz Raeisy, Shapoor Golbahar Haghighi, and Ali Akbar Safavi. Active noise control system via multi-agent credit assignment. *Journal of Intelligent & Fuzzy Systems*, 26(2):1051–1063, 2014. ISSN 10641246. doi: 10.3233/IFS-130797.

[70] Seyed Amir Hoseini Sabzevari and Majid Moavenian. Application of reinforcement learning for active noise control. *TURKISH JOURNAL OF ELECTRICAL ENGINEERING & COMPUTER SCIENCES*, 25(4):2606–2613, 2017. ISSN 13000632, 13036203. doi: 10.3906/elk-1602-189.

[71] Yi-Jun Guan, Yong Ge, Hong-Xiang Sun, Shou-Qi Yuan, and Xiao-Jun Liu. Low-Frequency, Open, Sound-Insulation Barrier by Two Oppositely Oriented Helmholtz Resonators. *Micromachines*, 12(12):1544, December 2021. ISSN 2072-666X. doi: 10.3390/mi12121544.

[72] María Pilar Peiró-Torres, Marcelino Ferri, Luis Godinho, Paulo Amado-Mendes, Francisco Jose Vea Folch, and Javier Redondo. Normal incidence sound insulation provided by Sonic Crystal Acoustic Screens made from rigid scatterers – assessment of different simulation methods. *Acta Acustica*, 5(28), 2021. ISSN 2681-4617. doi: 10.1051/aacus/2021021.

[73] David Ramírez-Solana, Javier Redondo, Agostino Marcello Mangini, and Maria Pia Fanti. Particle Swarm Optimization of Resonant Sonic Crystals Noise Barriers. *IEEE Access*, 11:38426–38435, 2023. ISSN 2169-3536. doi: 10.1109/ACCESS.2023.3267972.

[74] Fauzi Aslan and Roshun Paurobally. Modelling and simulation of active noise control in a small room. *Journal of Vibration and Control*, 24(3):607–618, February 2018. ISSN 1077-5463, 1741-2986. doi: 10.1177/1077546316647572.

[75] Yee, K. Numerical solution of initial boundary value problems involving maxwell's equations in isotropic media. *IEEE Transactions on Antennas and Propagation*, 14(3):302–307, May 1966. ISSN 0018-926X, 1558-2221. doi: 10.1109/TAP.1966.1138693.

[76] J. Redondo, R. Picó, M. R. Avis, and T. J. Cox. Prediction of the Random-Incidence Scattering Coefficient Using a FDTD Scheme. *Acta Acustica united with Acustica*, 95(6):1040–1047, November 2009. ISSN 16101928. doi: 10.3813/AAA.918236.

[77] Matteo Cingolani, Giulia Fratoni, Luca Barbaresi, Dario D'Orazio, Brian Hamilton, and Massimo Garai. A Trial Acoustic Improvement in a Lecture Hall with MPP Sound Absorbers and FDTD Acoustic Simulations. *Applied Sciences*, 11(6):2445, March 2021. ISSN 2076-3417. doi: 10.3390/app11062445.

[78] Javier Redondo, Pau Gaja-Silvestre, Luis Godinho, and Paulo Amado-Mendes. A Simple Method to Estimate the In Situ Performance of Noise Barriers. *Applied Sciences*, 12(14):7027:1–7027:13, July 2022. ISSN 2076-3417. doi: 10.3390/app12147027.

[79] Adam Kurowski and Bozena Kostek. Reinforcement Learning Algorithm and FDTD-Based Simulation Applied to Schroeder Diffuser Design Optimization. *IEEE Access*, 9:136004–136017, 2021. ISSN 2169-3536. doi: 10.1109/ACCESS.2021.3114628.

[80] David Ramírez-Solana, Valentino Sangiorgio, Nicola Parisi, Javier Redondo, Agostino Marcello Mangini, and Maria Pia Fanti. Parametric Design and Assessment of 3D Printable Open Noise Barrier: Device Customization to Protect Buildings from Train Brake Noise. *Journal of Architectural Engineering*, 30(2), 2024. doi: 10.1061/jaeied.aeeng-1605.

[81] Charles Fabry and Alfred Pérot. Sur les franges des lames minces argentées et leur application à la mesure de petites épaisseurs d'air. *Journal of Theoretical and Applied Optics*, 12(459-501), 1897.

[82] Jin-Young Jeon and Masaaki Okuma. Acoustic radiation optimization using the particle swarm optimization algorithm. *Jsme International Journal Series C-mechanical Systems Machine Elements and Manufacturing*, 47:560–567,, 2004. doi: 10.1299/jsmec.47.560.

[83] X. Xu and P. Lin. Parameter identification of sound absorption model of porous materials based on modified particle swarm optimization algorithm. *PLoS ONE*, 16(5), 2021. doi: 10.1371/journal.pone.0250950.

[84] D. Chen, J. Zhao, C. Fei, D. Li, Y. Zhu, Z. Li, R. Guo, L. Lou, W. Feng, and Y. Yang. Particle swarm optimization algorithm-based design method for ultrasonic transducers. *Micromachines*, 11(8):715,, 2020. doi: 10.3390/mi11080715.

[85] Renato Barbieri, Nilson Barbieri, and Key Fonseca Lima. Some applications of the PSO for optimization of acoustic filters. *Applied Acoustics*, 89:62–70,, 2015. doi: 10.1016/j.apacoust.2014.09.007.

[86] M. Szczepanik, A. Poteralski, J. Ptaszny, and T. Burczyński. Hybrid particle swarm optimizer and its application in identification of room acoustic properties. In *Swarm and Evolutionary Computation. EC SIDE 2012 2012. Lecture Notes in Computer Science*, volume 7269, pages 386–394. Springer, Berlin, 2012.

[87] Arindam Deb, Jibendu Sekhar Roy, and Bhaskar Gupta. Performance Comparison of Differential Evolution, Particle Swarm Optimization and Genetic Algorithm in the Design of Circularly Polarized Microstrip Antennas. *IEEE Transactions on Antennas and Propagation*, 62(8):3920–3928, August 2014. ISSN 0018-926X, 1558-2221. doi: 10.1109/TAP.2014.2322880.

[88] Vincent Roberge, Mohammed Tarbouchi, and Gilles Labonte. Comparison of Parallel Genetic Algorithm and Particle Swarm Optimization for Real-Time UAV Path Planning. *IEEE Transactions on Industrial Informatics*, 9(1):132–141, February 2013. ISSN 1551-3203, 1941-0050. doi: 10.1109/TII.2012.2198665.

[89] Monica Clemente, Maria Pia Fanti, Giorgio Iacobellis, Massimiliano Nolich, and Walter Ukovich. A decision support system for user-based vehicle relocation in car sharing systems. *IEEE TRANSACTIONS ON SYSTEMS*, 48(8), 2018.

[90] R. Poli, J. Kennedy, and T. Blackwell. Particle swarm optimization, an overview. *Swarm Intelligence*, 1(1):33–57,, 2007. doi: 10.1007/s11721-007-0002-0.

[91] Y. Shi and R. Eberhart. A modified particle swarm optimizer. In *World Congress on Computational Intelligence and IEEE International Conference on Evolutionary Computation*, 1998. doi: 10.1109/icec.1998.699146.

[92] Russel Eberhart and Yuhui Shi. Comparing inertia weights and constriction factors in particle swarm optimization. In *Proceedings of the IEEE Congress on Evolutionary Computation*, San Diego, USA, 2000. doi: 10.1109/cec.2000.870279.

[93] Gaetano Volpe, Agostino Marcello Mangini, and Maria Pia Fanti. Job Shop Sequencing in Manufacturing Plants by Timed Coloured Petri Nets and Particle Swarm Optimization. *IFAC-PapersOnLine*, 55(28):350–355, 2022. ISSN 24058963. doi: 10.1016/j.ifacol.2022.10.365.

[94] Jia-Yi Lin, Wan-Ju Cheng, Chang-Fu Wu, and Ta-Yuan Chang. Associations of road traffic noise and its frequency spectrum with prevalent depression in Taichung, Taiwan. *Frontiers in Public Health*, 11:1116345:1–1116345:9, January 2023. ISSN 2296-2565. doi: 10.3389/fpubh.2023.1116345.

[95] Krzysztof Polak and Jarosław Korzeb. Modelling the acoustic signature and noise propagation of high speed railway vehicle. *Archives of Transport*, 64(4):73–87, December 2022. ISSN 0866-9546, 2300-8830. doi: 10.5604/01.3001.0016.1051.

[96] Olivier Chiello, Jean-Jacques Sinou, Nicolas Vincent, Guillaume Vermot Des Roches, Franck Cocheteux, Selim Bellaj, and Xavier Lorang. Squeal noise generated by railway disc brakes: Experiments

and stability computations on large industrial models. *The Journal of the Acoustical Society of America*, 133(5_Supplement):3461–3461, May 2013. ISSN 0001-4966, 1520-8524. doi: 10.1121/1.4806160.

[97] Francesco Cascetta, Francesco Caputo, and Alessandro De Luca. Squeal Frequency of a Railway Disc Brake Evaluation by FE Analyses. *Advances in Acoustics and Vibration*, 2018:1–10, April 2018. ISSN 1687-6261, 1687-627X. doi: 10.1155/2018/4692570.

[98] Erwin H. Jansen, Michael G. Dittrich, and Erik L. Sikma. Brake noise measurements on mixed freight trains with composite brake blocks. *The Journal of the Acoustical Society of America*, 123(5):3266–3266, May 2008. ISSN 0001-4966, 1520-8524. doi: 10.1121/1.2933586.

[99] João Lázaro, Matheus Pereira, Pedro Alves Costa, and Luís Godinho. Performance of Low-Height Railway Noise Barriers with Porous Materials. *Applied Sciences*, 12(6):2960:1–2960:18, March 2022. ISSN 2076-3417. doi: 10.3390/app12062960.

[100] C E Tickell, P Downing, and C J Jacobsen. Rail Wheel Squeal — Some Causes and a Case Study of Freight-Car Wheel Squeal Reduction. In *Proceedings of Acoustics 2004*, pages 239–244, Gold Coast, Australia, 2004-11-03/2004-11-05.

[101] Alexandre Jolibois, Jerôme Defrance, Harry Koreneff, Philippe Jean, Denis Duhamel, and Victor W. Sparrow. In situ measurement of the acoustic performance of a full scale tramway low height noise barrier prototype. *Applied Acoustics*, 94:57–68, July 2015. ISSN 0003682X. doi: 10.1016/j.apacoust.2015.02.006.

[102] Gioia Fusaro and Massimo Garai. Acoustic Requalification of an Urban Evolving Site and Design of a Noise Barrier: A Case Study at the Bologna Engineering School. *Applied Sciences*, 14(5):1837:1–1837:18, February 2024. ISSN 2076-3417. doi: 10.3390/app14051837.

[103] Laura Sousa, Luís Pereira, David Montes-González, Denilson Ramos, Paulo Amado-Mendes, Juan Miguel Barrigón-Morillas, and Luís Godinho. Experimental Analysis and Simulation of a Porous Absorbing Layer for Noise Barriers. *Applied Sciences*, 13(4):2638:1–2638:21, February 2023. ISSN 2076-3417. doi: 10.3390/app13042638.

[104] Guglielmo Minelli, Hua-Dong Yao, Niklas Andersson, Daniel Lindblad, Jens Forssén, Patrik Höstmad, and Siniša Krajnović. Using

horizontal sonic crystals to reduce the aeroacosutic signature of a simplified ICE3 train model. *Applied Acoustics*, 172:107597:1–107597:12, January 2021. ISSN 0003682X. doi: 10.1016/j.apacoust.2020.107597.

[105] Xiaoping Wu, Xuanyi He, and Jie Huang. Comparative Analysis of Dynamic Responses of Different Types of High-Speed Railway Noise Barriers under the Influence of Fluctuating Wind Pressure. *Sustainability*, 14(19):12900:1–12900:16, October 2022. ISSN 2071-1050. doi: 10.3390/su141912900.

[106] Weichao Yang, Dehui Ouyang, E. Deng, Xuhui He, Yunfeng Zou, and Yongming Huang. Aerodynamic characteristics of two noise barriers (fully enclosed and semi-enclosed) caused by a passing train: A comparative study. *Journal of Wind Engineering and Industrial Aerodynamics*, 226:105028:1–105028:16, July 2022. ISSN 01676105. doi: 10.1016/j.jweia.2022.105028.

[107] Jing Zheng, Qingliang Li, Xiaozhen Li, and Yunke Luo. Train-Induced Fluctuating Pressure and Resultant Dynamic Response of Semienclosed Sound Barriers. *Shock and Vibration*, 2020:1–16, September 2020. ISSN 1070-9622, 1875-9203. doi: 10.1155/2020/6901564.

[108] Shaobo Zhang, Jiang Liu, Hongbo Zhang, and Shuliang Wang. Tunable Low Frequency Band Gap and Waveguide of Phononic Crystal Plates with Different Filling Ratio. *Crystals*, 11(7):828:1–828:13, July 2021. ISSN 2073-4352. doi: 10.3390/cryst11070828.

[109] Hsiao Mun Lee, Yuting Hua, Jinlong Xie, and Heow Pueh Lee. Parametric Optimization of Local Resonant Sonic Crystals Window on Noise Attenuation by Using Taguchi Method and ANOVA Analysis. *Crystals*, 12(2):160:1–160:21, January 2022. ISSN 2073-4352. doi: 10.3390/cryst12020160.

[110] Xiao-Long Li, Wai Kit Lam, and S. K. Tang. Experimental investigation on the enhancement of plenum window noise reduction using solid scatterers. *The Journal of the Acoustical Society of America*, 153(2): 1361–1374, February 2023. ISSN 0001-4966. doi: 10.1121/10.0017353.

[111] Theo Cavalieri, Alejandro Cebrecos, Jean-Philippe Groby, C Chaufour, and Vicente Romero-García. Three-dimensional multiresonant lossy sonic crystal for broadband acoustic attenuation: Application to train noise reduction. *Applied Acoustics*, 146:1–8, March 2019. ISSN 0003682X. doi: 10.1016/j.apacoust.2018.10.020.

[112] Clément Lagarrigue, Jean-Philippe Groby, Vincent Tournat, Olivier Dazel, and Olga Umnova. Absorption of sound by porous layers with embedded periodic arrays of resonant inclusions. *The Journal of the Acoustical Society of America*, 134(6):4670–4680, December 2013. ISSN 0001-4966, 1520-8524. doi: 10.1121/1.4824843.

[113] Alexandre Lardeau, Jean-Philippe Groby, and Vicente Romero-García. Broadband Transmission Loss Using the Overlap of Resonances in 3D Sonic Crystals. *Crystals*, 6(5):51:1–51:12, May 2016. ISSN 2073-4352. doi: 10.3390/cryst6050051.

[114] Zhengyou Liu, Xixiang Zhang, Yiwei Mao, Y. Y. Zhu, Zhiyu Yang, C. T. Chan, and Ping Sheng. Locally Resonant Sonic Materials. *Science*, 289(5485):1734–1736, September 2000. ISSN 0036-8075, 1095-9203. doi: 10.1126/science.289.5485.1734.

[115] Mattia Cenedese, Edoardo Belloni, and Francesco Braghin. Interaction of Bragg scattering bandgaps and local resonators in mono-coupled periodic structure. *Journal of Applied Physics*, 129(12): 124501:1–124501:17, 2021. doi: 10.1063/5.0038438.

[116] Javier Redondo, David Ramírez-Solana, and Rubén Picó. Increasing the Insertion Loss of Sonic Crystal Noise Barriers with Helmholtz Resonators. *Applied Sciences*, 13(6):3662:1–3662:13, March 2023. ISSN 2076-3417. doi: 10.3390/app13063662.

[117] B. Yuan, V.F. Humphrey, J. Wen, and X. Wen. On the coupling of resonance and Bragg scattering effects in three-dimensional locally resonant sonic materials. *Ultrasonics*, 53:1332–1343,, 2013. doi: 10.1016/j.ultras.2013.03.019.

[118] María Pilar Peiró-Torres, Sergio Castiñeira-Ibáñez, Javier Redondo, and Juan Vicente Sánchez-Pérez. Interferences in locally resonant sonic metamaterials formed from Helmholtz resonators. *Applied Physics Letters*, 114(17):171901, April 2019. ISSN 0003-6951, 1077-3118. doi: 10.1063/1.5092375.

[119] Javier Redondo, Luis Godinho, Kestutis Staliunas, and Juan Vicente Sanchez-Perez. An equivalent lattice-modified model of interfering Bragg bandgaps and Locally Resonant Stop Bands for phononic crystal made from Locally Resonant elements. *Applied Acoustics*, 211:109555:1–109555:6, August 2023. ISSN 0003682X. doi: 10.1016/j.apacoust.2023.109555.

[120] Martin Vasina, Katarina Monkova, Peter Pavol Monka, Drazan Kozak, and Jozef Tkac. Study of the Sound Absorption Properties of 3D-Printed Open-Porous ABS Material Structures. *Polymers*, 12(5): 1062, May 2020. ISSN 2073-4360. doi: 10.3390/polym12051062.

[121] Cecilia Casarini, James F. C. Windmill, and Joseph C. Jackson. 3D printed small-scale acoustic metamaterials based on Helmholtz resonators with tuned overtones. In *2017 IEEE SENSORS*, pages 1–3, Glasgow, UK, October 2017. IEEE. ISBN 978-1-5090-1012-7. doi: 10.1109/ICSENS.2017.8234381.

[122] Jean Boulvert, Théo Cavalieri, Vicente Romero-García, Gwénaël Gabard, and Jean-Philippe Groby. Optimization of 3D printed porous materials accounting for manufacturing defects. *INTER-NOISE and NOISE-CON Congress and Conference Proceedings*, 263(3):3143–3148, August 2021. ISSN 0736-2935. doi: 10.3397/IN-2021-2314.

[123] Alicia Gardiner, Paul Daly, Roger Domingo-Roca, James Windmill, Andrew Feeney, and Joseph Jackson-Camargo. Additive Manufacture of Small-Scale Metamaterial Structures for Acoustic and Ultrasonic Applications. *Micromachines*, 12(6):634, May 2021. ISSN 2072-666X. doi: 10.3390/mi12060634.

[124] International Organization for Standardization. ISO 10140-2:2021 "Measurement of airborne sound insulation" - Laboratory measurement of sound insulation of building elements: Part 2: Measurement of airborne sound insulation, 2021.

[125] Ao Yamada and Masahiro Toyoda. Prediction of bandgap characteristics by sonic crystals. *Acoustical Science and Technology*, 41(6):815–818, November 2020. ISSN 1346-3969, 1347-5177. doi: 10.1250/ast.41.815.

[126] Malcolm J. Crocker and A. John Price. Sound transmission using statistical energy analysis. *Journal of Sound and Vibration*, 9:469–486, 1969. URL `https://api.semanticscholar.org/CorpusID:119834137`.

[127] Carl Hopkins. *Sound Insulation*. Elsevier, Oxford, 2007.

[128] Mário Martins, Luís Godinho, and Luís Picado-Santos. Numerical evaluation of sound attenuation provided by periodic structures. *Archives of Acoustics*, vol. 38(No 4):503–516, 2013. doi: 10.2478/aoa-2013-0060.

[129] Jaime Galiana-Nieves, Romina Del Rey, Jesús Alba, David Ramírez-Solana, and Javier Redondo. Evaluación de la Reducción Sonora Proporcionada por Materiales con Alta Permeabilidad Acústica. In *Proceedings of Tecniacustica 2022*, Elche (Spain), 2022.

[130] Romina Del Rey, Jesús Alba, Juan C. Rodríguez, and Laura Bertó. Characterization of New Sustainable Acoustic Solutions in a Reduced Sized Transmission Chamber. *Buildings*, 9(3):60, March 2019. ISSN 2075-5309. doi: 10.3390/buildings9030060.

[131] Michael R. Stinson. The propagation of plane sound waves in narrow and wide circular tubes, and generalization to uniform tubes of arbitrary cross-sectional shape. *The Journal of the Acoustical Society of America*, 89(2):550–558, February 1991. ISSN 0001-4966, 1520-8524. doi: 10.1121/1.400379.

[132] Gioia Fusaro, Luca Barbaresi, Matteo Cingolani, Massimo Garai, Edoardo Ida, Andrea Prato, and Alessandro Schiavi. Investigation of the impact of additive manufacturing techniques on the acoustic performance of a coiled-up resonator. *The Journal of the Acoustical Society of America*, 153(5):2921:1–2921:12, May 2023. ISSN 0001-4966. doi: 10.1121/10.0019474.

[133] Fernando J. F. G. Branco, Luís Godinho, and António Tadeu. ACOUSTIC INSERTION LOSS PROVIDED BY RIGID ACOUSTIC BARRIERS OF DIFFERENT SHAPES. *Journal of Computational Acoustics*, 11(04):503–519, December 2003. ISSN 0218-396X, 1793-6489. doi: 10.1142/S0218396X03002073.

[134] Rosa Martínez-Sala, J. Sancho, Juan Vicente Sánchez-Pérez, Vicente Gómez, Jaime Llinares, and Francisco Meseguer. Sound attenuation by sculpture. *Nature*, 378(6554):241–241, November 1995. ISSN 0028-0836, 1476-4687. doi: 10.1038/378241a0.

[135] Manvir S. Kushwaha, Peter Halevi, Leonard Dobrzynski, and B. Djafari-Rouhani. Acoustic band structure of periodic elastic composites. *Physical Review Letters*, 71(13):2022–2025, September 1993. ISSN 0031-9007. doi: 10.1103/PhysRevLett.71.2022.

[136] Sergio Castiñeira-Ibáñez, Constanza Rubio, Javier Redondo, and Juan Vicente Sánchez-Pérez. Quantitative characterization of bandgap properties of sets of isolated acoustic scatterers arranged using fractal geometries. *Applied Physics Express*, 7(4):042201, April 2014. ISSN 1882-0778, 1882-0786. doi: 10.7567/APEX.7.042201.

[137] Anchen Ni and Zhifei Shi. Broadband wave attenuation and topological transport in novel periodic pile barriers. *Engineering Structures*, 262:114378, July 2022. ISSN 01410296. doi: 10.1016/j.engstruct.2022.114378.

[138] Xinhua Hu, C. T. Chan, and Jian Zi. Two-dimensional sonic crystals with Helmholtz resonators. *Physical Review E*, 71(5):055601, May 2005. ISSN 1539-3755, 1550-2376. doi: 10.1103/PhysRevE.71.055601.

[139] Jan Radosz. Acoustic performance of noise barrier based on sonic crystals with resonant elements. *Applied Acoustics*, 155:492–499, December 2019. ISSN 0003682X. doi: 10.1016/j.apacoust.2019.06.003.

[140] Xiaochun Qin, Anchen Ni, Zhenghao Chen, Mengjie Fang, and Yanhua Li. Numerical modeling and field test of sonic crystal acoustic barriers. *Environmental Science and Pollution Research*, 30 (6):16289–16304, October 2022. ISSN 1614-7499. doi: 10.1007/s11356-022-23109-2.

[141] Karisma Mohapatra and Dibya Prakash Jena. Insertion loss of sonic crystal made with multi resonant shells. *Applied Acoustics*, 171: 107676, January 2021. ISSN 0003682X. doi: 10.1016/j.apacoust.2020.107676.

[142] D.P. Elford, L. Chalmers, F.V. Kusmartsev, and G.M. Swallowe. Matryoshka Locally Resonant Sonic Crystal. *The Journal of the Acoustical Society of America*, 130(5), 2011. doi: 10.1121/1.3643818.

[143] V. Romero-García, J.V. Sánchez-Pérez, L.M. García-Raffi, J.M. Herrero, S. García-Nieto, and X. Blasco. Hole distribution in phononic crystals: Design and optimization. *The Journal of the Acoustical Society of America*, 125(6):3774–3783,, 2009. doi: 10.1121/1.3126948.

[144] Javier Redondo, Juan Vicente Sánchez-Pérez, Xavier Blasco, Juan Manuel Herrero, and Michael Vorländer. Optimized sound diffusers based on sonic crystals using a multiobjective evolutionary algorithm. *The Journal of the Acoustical Society of America*, 139(5):2807–2814, May 2016. ISSN 0001-4966, 1520-8524. doi: 10.1121/1.4948580.

[145] Jaime Galiana Nieves, Javier Redondo, Daniel Benítez Aragón, David Ramírez-Solana, and Juan Manuel Herrero. Evolutionary optimization processes for acoustic applications where size matters. *INTER-NOISE and NOISE-CON Congress and Conference Proceedings*, 265 (3):4125–4135, 2022. ISSN 0736-2935. doi: 10.3397/IN_2022_0589.

[146] Jaime Galiana-Nieves, David Ramírez-Solana, Rubén Picó, and Javier Redondo. Periodic Boundary Conditions implementation for the study of sonic crystals. In *Proceedings of the 10th Convention of the European Acoustics Association Forum Acusticum 2023*, pages 3835–3840, Turin, Italy, 2023. European Acoustics Association. ISBN 978-88-88942-67-4. doi: 10.61782/fa.2023.0810.

[147] David Ramírez-Solana, Sergio Castiñeira-Ibáñez, Jose Maria Bravo-Plana-Sala, Juan Vicente Sánchez-Pérez, Javier Redondo, and Rubén Picó. Analysis of the interaction of helmholtz resonators in periodic acoustic metamaterials depending on its orientation with the acoustic source. *INTER-NOISE and NOISE-CON Congress and Conference Proceedings*, 263(6):215–226, August 2021. ISSN 0736-2935. doi: 10.3397/IN-2021-1369.

[148] Bin Wu, Wei Jiang, Jiaqing Jiang, Zinan Zhao, Yuqi Tang, Weijian Zhou, and Weiqiu Chen. Wave Manipulation in Intelligent Metamaterials: Recent Progress and Prospects. *Advanced Functional Materials*, 34(29):2316745, July 2024. ISSN 1616-301X, 1616-3028. doi: 10.1002/adfm.202316745.

[149] Hyeonu Heo, Arkadii Krokhin, Arup Neogi, Zhiming Cui, Zhihao Yuan, Yihe Hua, Jaehyung Ju, and Ezekiel Walker. Multifunctional Acoustic Device Based on a Phononic Crystal with Independently Controlled Asymmetric Rotating Rods. *Physical Review Applied*, 19(5):054008, May 2023. ISSN 2331-7019. doi: 10.1103/PhysRevApplied.19.054008.

[150] Lige Chang, Xiaowen Li, Zengrong Guo, Yajun Cao, Yuyang Lu, Rinaldo Garziera, and Hanqing Jiang. On-demand tunable metamaterials design for noise attenuation with machine learning. *Materials & Design*, 238:112685, February 2024. ISSN 02641275. doi: 10.1016/j.matdes.2024.112685.

[151] Zhenyu Chen, Yung Boon Chong, Kian Meng Lim, and Heow Pueh Lee. Reconfigurable 3D printed acoustic metamaterial chamber for sound insulation. *International Journal of Mechanical Sciences*, 266:108978, March 2024. ISSN 00207403. doi: 10.1016/j.ijmecsci.2024.108978.

[152] Hongqing Dai, Pan Xue, Enhui Lu, Lei Wang, and Laishui Zhou. Experimental realization of a soft topological acoustic switch. *Physical*

Review B, 107(14):144105, April 2023. ISSN 2469-9950, 2469-9969. doi: 10.1103/PhysRevB.107.144105.

[153] Pan Xue, Hongqing Dai, and Laishui Zhou. Acoustic Switch via a Compressible Minimal Surface Structure. *Advanced Engineering Materials*, 25(4):2201144, February 2023. ISSN 1438-1656, 1527-2648. doi: 10.1002/adem.202201144.

[154] Jyotsna Dhillon, Ezekiel Walker, Arkadii Krokhin, and Arup Neogi. Energy trapping in a phononic crystal cavity enhanced by nonreciprocal acoustic wave transmission. *Applied Acoustics*, 203:109192, February 2023. ISSN 0003682X. doi: 10.1016/j.apacoust.2022.109192.

[155] Serkan Alagoz and Baris Baykant Alagoz. Sonic crystal acoustic switch device. *The Journal of the Acoustical Society of America*, 133(6):EL485–EL490, June 2013. ISSN 0001-4966, 1520-8524. doi: 10.1121/1.4807306.

[156] Xue-Feng Li, Xu Ni, Liang Feng, Ming-Hui Lu, Cheng He, and Yan-Feng Chen. Tunable Unidirectional Sound Propagation through a Sonic-Crystal-Based Acoustic Diode. *Physical Review Letters*, 106 (8):084301, February 2011. ISSN 0031-9007, 1079-7114. doi: 10.1103/PhysRevLett.106.084301.

[157] Ahmet Cicek, Olgun Adem Kaya, and Bulent Ulug. Refraction-type sonic crystal junction diode. *Applied Physics Letters*, 100(11):111905, March 2012. ISSN 0003-6951, 1077-3118. doi: 10.1063/1.3694020.

[158] Hong-xiang Sun, Shou-qi Yuan, and Shu-yi Zhang. Asymmetric acoustic transmission in multiple frequency bands. *Applied Physics Letters*, 107(21):213505, November 2015. ISSN 0003-6951, 1077-3118. doi: 10.1063/1.4936609.

[159] Sagr Alamri, Bing Li, Garrett Mchugh, Nicholas Garafolo, and K.T. Tan. Dissipative diatomic acoustic metamaterials for broadband asymmetric elastic-wave transmission. *Journal of Sound and Vibration*, 451:120–137, July 2019. ISSN 0022460X. doi: 10.1016/j.jsv.2019.03.018.

[160] J. V. Sánchez-Pérez, D. Caballero, R. Mártinez-Sala, C. Rubio, J. Sánchez-Dehesa, F. Meseguer, J. Llinares, and F. Gálvez. Sound Attenuation by a Two-Dimensional Array of Rigid Cylinders. *Physical Review Letters*, 80(24):5325–5328, June 1998. ISSN 0031-9007, 1079-7114. doi: 10.1103/PhysRevLett.80.5325.

[161] L. Sanchis, F. Cervera, J. Sánchez-Dehesa, J. V. Sánchez-Pérez, C. Rubio, and R. Martínez-Sala. Reflectance properties of two-dimensional sonic band-gap crystals. *The Journal of the Acoustical Society of America*, 109(6):2598–2605, June 2001. ISSN 0001-4966, 1520-8524. doi: 10.1121/1.1369784.

[162] Kosuke Nagaya, Yasudide Hano, and Akihisa Suda. Silencer consisting of two-stage Helmholtz resonator with auto-tuning control. *The Journal of the Acoustical Society of America*, 110(1):289–295, July 2001. ISSN 0001-4966, 1520-8524. doi: 10.1121/1.1370524.

[163] David Ramírez-Solana, Jaime Galiana-Nieves, Javier Redondo, Agostino Marcello Mangini, and Maria Pia Fanti. Improving Insertion Loss of Sonic Crystal Active Noise Barrier by Reinforcement Learning and Finite Difference Time Domain Simulations. *IEEE Access*, 12:77988–77998, 2024. ISSN 2169-3536. doi: 10.1109/ACCESS.2024.3406857.

[164] Yuanyuan Li, Kunqi Huang, Menyang Gong, Chenghao Sun, Shenlian Gao, Yun Lai, and Xiaozhou Liu. Realization of acoustic tunable logic gate composed of soft materials. *Results in Physics*, 57:107421, February 2024. ISSN 22113797. doi: 10.1016/j.rinp.2024.107421.

[165] Binsheng Li, Hui Chen, Baizhan Xia, and Lingyun Yao. Acoustic energy harvesting based on topological states of multi-resonant phononic crystals. *Applied Energy*, 341:121142, July 2023. ISSN 03062619. doi: 10.1016/j.apenergy.2023.121142.